Dissertation

submitted to the
Combined Faculties for the Natural Sciences and for Mathematics
of the Ruperto-Carola University of Heidelberg, Germany,
for the degree of
Doctor of Natural Sciences

Put forward by
Marcus Oliver Held, M.Sc.
born in Worms, Germany
Oral examination: 13th July 2021

4Pi-MINFLUX localizations of fluorescent molecules

Referees: Prof. Dr. Dr. h. c. mult. Stefan W. Hell
Prof. Dr. Ulrich S. Schwarz

Summary

4Pi-MINFLUX localizations of fluorescent molecules

MINFLUX has led to remarkable improvements in localization precision compared to centroid-fitting localization schemes. Yet, molecular localization precision with far fewer than 100 photons remained to be demonstrated. Previously, the localization precision and the number of detected photons were linked by an inverse square root relation. Decoupling these parameters allows for ultrafast tracking and measurements of photo-sensitive samples. An illumination scheme with two opposing objective lenses promises further improvements of the efficient use of detected photons in a MINFLUX localization. In this thesis, the MINFLUX concept was combined with a 4Pi-optics illumination scheme to explore highest axial localization precision with low photon counts. Simulations suggested that, for a given signal-background-ratio, a 4Pi-MINFLUX microscope would outperform single objective lens MINFLUX microscopes by 40 % in terms of detected photons required for molecular localization precision. Our implementation surpassed this expectation and achieved a localization precision of 1 nm with only several tens of detected photons in single molecule measurements. Detecting more than 100 photons led to an axial localization precision of one one-thousandth of the excitation wavelength, limited only by vibrations and thermal drift. The axial resolving power was demonstrated with DNA origami-based nanorulers featuring single fluorophore distances of 10 nm. These results highlight that molecular distances and dynamics on a spatial scale of 1 nm, and below, become accessible with an extremely low number of detected photons.

Zusammenfassung

4Pi-MINFLUX Lokalisationen von fluoreszenten Molekülen

MINFLUX erzielte bemerkenswerte Verbesserungen in der Lokalisierungspräzision im Vergleich zu Schwerpunkts anpassenden Lokalisierungsschemata. Allerdings wurde eine molekulare Lokalisierungspräzision mit weit weniger als 100 Photonen noch nicht erreicht. Bisher waren Lokalisierungspräzision und Anzahl der detektierten Photonen stets durch eine inverse Quadratwurzelbeziehung miteinander verbunden. Die Auflösung dieser Beziehung ermöglicht ultraschnelles Tracking und Messungen von lichtempfindlichen Proben. Die effiziente Nutzung detektierter Photonen in einer MINFLUX-Lokalisation kann mit einem Beleuchtungsschema, das zwei gegenüberliegende Objektivlinsen nutzt, weiter verbessert werden. In dieser Arbeit wurde das MINFLUX-Konzept mit einem 4Pi-Optik Beleuchtungsschema kombiniert, um höchste axiale Lokalisierungspräzision mit einer geringen Photonenzahl zu erzielen. Simulationen legten nahe, dass ein 4Pi-MINFLUX-Mikroskop bei einem gegebenen Signal-Hintergrund-Verhältnis 40 % weniger Photonen für eine molekulare Lokalisierungspräzision benötigt als MINFLUX-Mikroskope mit nur einer einzelnen Objektivlinse. Unsere Implementierung übertraf diese Erwartung und erreichte in Einzelmolekülmessungen eine Lokalisierungsgenauigkeit von 1 nm mit nur einigen zehn detektierten Photonen. Die Detektion von mehr als 100 Photonen erzielte eine axiale Lokalisierungspräzision von einem Tausendstel der Anregungswellenlänge. Dieser Wert war lediglich durch Vibrationen und thermischen Drift begrenzt. Das axiale Auflösungsvermögen wurde an Hand von DNA-Origami-basierten Nanolinealen demonstriert, deren einzelne Fluorophore einen Abstand von 10 nm besaßen. Diese Ergebnisse veranschaulichen, dass eine extrem geringe Anzahl an detektierter Photonen ausreicht, um molekulare Abstände und Dynamiken im Subnanometer-Bereich zu messen.

To my parents
and my beloved grandma

"Die Phantasie ging und die Welt kam."

author unknown (movie quote)

Contents

List of Abbreviations

1D one-dimensional
2D two-dimensional
3D three-dimensional
4Pi-SMS 4Pi single-molecule switching

AOTF acousto-optic tunable filter
APD avalanche photodiode

bfp back focal plane

CRB Cramér-Rao bound

DNA deoxyribonucleic acid

FPGA field-programmable gate array
FRET Förster resonance energy transfer
fwhm full width at half maximum

GMM Gaussian mixture model
GNP gold nanoparticle

iPALM interferometric PALM
isoSTED isotropic STED

NA numerical aperture

PALM photoactivation localization microscopy
PMT photon multiplier tube
PSD power spectral density
PSF point spread function

SBR signal-background-ratio
SIM structured illumination microscopy
STED stimulated emission depletion
STORM stochastic optical reconstruction microscopy

UV ultraviolet

1 Introduction

Since the invention of the first light microscope, many techniques have been developed to look in more detail into subcellular biological processes. Electron microscopy is currently the technique that allows the highest spatial resolution in biological materials [1]. Yet, despite the high resolution of electron microscopy, the fluorescence light microscope remains an important tool for the investigation of biological structures and dynamics. Some of the main disadvantages of electron microscopy are the laborious sample preparation to image deep into a cell and achieving contrast, and the further requirement for imaging in vacuum. Both complicate the study of dynamical biological processes [2].

A fluorescence microscope does not directly create an image of the biological structure in the sample but rather of the fluorophores incorporated to it [3]. Different labeling strategies allow molecule-specific selection of the structure of interest, and, when illuminated with excitation light, its contrast with respect to the background is drastically increased. In addition, photophysical properties of fluorophores, like emission wavelength and fluorescence lifetime, can be used to image different structures of the same sample at the same time [4, 5].

Diffraction-limited microscopy, of which the confocal microscope was the gold standard for many decades, allows laterally resolving structures up to approximately half the excitation wavelength λ as given by Abbe's law [6]. In order to maximize the resolution in fluorescence microscopy, high numerical aperture (NA) objective lenses in combination with oil immersion (n) have been successfully used. However, the diffraction pattern, i.e. point spread function (PSF), of the excitation light in the sample plane is more extended along the optical axis ($d_z = {}^{2n\lambda}/_{NA^2}$) compared to the lateral direction ($d_{x,y} = {}^{0.61\lambda}/_{NA}$) by a factor of 3.7 [7]. The same holds true for the fluorescence in the emission path. The anisotropy of the PSF, created with conventional microscopy, limits the information that can be obtained from the biological sample along the axial direction. With confocal detection, a slight improvement in isotropy is achieved leading to an axial resolution of $\sim 500\,\text{nm}$ and a lateral resolution of $\sim 250\,\text{nm}$ when using red excitation wavelengths.

A further improvement towards isotropic resolution has been achieved with confocal 4Pi microscopy [8]. Here, by the coherent use of a second objective lens, the solid aperture angle of the microscope can be increased close to its maximal physically

achievable value of 4π. In a type-C 4Pi microscope, the information content about the emitter position is improved even further, within the Abbe limit. This is achieved by the generation of a converging spherical wave in the illumination and the nearly complete reconstruction of the diverging spherical wave of the emitter. The application of 4Pi microscopy is hampered by the larger technical effort required for close to aberration free imaging. Axial resolution improvements with a single objective lens microscope can also be achieved by depth-sensitive diffraction patterns (e.g. astigmatic [9] or double-helix PSF [10]), or total internal reflection excitation (the latter and further examples can be found in [11]).

Diffraction-unlimited superresolution microscopy allows for achieving resolutions below the Abbe limit by implementing a focal switch and sequentially detecting adjacent fluorophores within a diffraction-limited volume. The concept was first realized with STED, a confocal scanning technique which deterministically induces stimulated emission of the excited fluorophore state, allowing spontaneous fluorescence emission only at a targeted spot where the diffraction pattern of the depletion laser features an intensity minimum [12, 13]. The resolution is determined by the power, i.e. number of photons (N_{STED}), of the depletion laser ($d \propto 1/\sqrt{N_{STED}}$). Several years later, the concept was implemented for widefield microscopy (photoactivation localization microscopy (PALM) [14] / stochastic optical reconstruction microscopy (STORM) [15]) by stochastically activating only a single fluorophore within a diffraction-limited spot, i.e. unlocking its ability to emit fluorescence photons. The resolution is determined by the number of detected fluorescence photons (N_{fl}) from the diffraction spot on the camera ($d \propto 1/\sqrt{N_fl}$).

Diffraction-unlimited superresolution microscopy paved the way for new biological discoveries like the cytoskeleton periodicity in neurons [16]. In combination with a double objective lens system, almost isotropically resolved three-dimensional (3D) images of fixed cells could be recorded (isoSTED [17], iPALM [18] and 4Pi single-molecule switching (4Pi-SMS) [19]). The restriction of the imaging depth of interferometric single molecule localization (iPALM and 4Pi-SMS) to approximately one half of the wavelength was overcome by inducing astigmatism on the detection beam enabling the acquisition of a whole cell [20]. Hence, double objective lens systems became a central element for 3D optical superresolution imaging.

Theoretically, these superresolution microscopy techniques can achieve molecular resolution down to 1 nm. However, practically, each fluorophore can only perform a finite number of fluorescence emission cycles before it irreversibly ends up in a non-fluorescent state, i.e. photobleaches [21]. Despite the development of more powerful excitation and depletion lasers, as well as bright and stable fluorophores, the inverse square root law limits the achievable resolution in STED and PALM/STORM to roughly 20 to 30 nm, i.e. one twentieths of a wavelength.

A recently introduced new superresolution technique called MINFLUX achieves a localization precision in the range of 1 nm with far fewer photons ($\sim$ 500 [22]) compared to camera-based localizations using centroid fitting ($\sim$10000 [23]). This enables significantly higher image resolution with a similar photon budget. MINFLUX synegistically uses the advantages of the previously introduced superresolution techniques and thereby circumvents the inverse square root law. As a localization technique like PALM/STORM, individual emitters are located sequentially in time by making use of their molecular switching properties between a fluorescent 'on'- and long-lived 'off'-state. Similarly to STED, MINFLUX uses a scannable beam with an intensity minimum. However, in MINFLUX the beam is used for fluorescence excitation instead of depletion. The control of its zero position allows targeted probing of the fluorescence signal of the emitter at specific coordinates in the sample. Since the shape of the diffraction pattern around the minimum is known, the position of the emitter can be calculated from the relative difference of the emitted photon counts.

Various practical demonstrations of the MINFLUX concept have emerged within the last years. The implementation of an iterative MINFLUX localization scheme has demonstrated that larger field of views (e.g. cellular structures in the range of 10 µm) can be studied without compromising the high localization precision [24]. Furthermore, based on depletion schemes used previously in 3D STED [25], 3D multicolor images of protein distributions in fixed and living cells were recorded in iterative 3D MINFLUX [24]. Other imaging modalities, such as pulsed excitation combined with fluorescence lifetime detection, start to be integrated into MINFLUX [26]. Current widefield implementations, in which a structured illumination pattern is translated to three positions per dimension, can locate multiple emitters at once (SIMFLUX [27] and ROSE [28]). However, such techniques lack the ability to iteratively center the zero intensity to individual emitters, which is crucial to make use of the scalable localization precision. Consequently, these techniques allow only a factor two improvement in localization precision compared to centroid-fitting with the same photon budget.

While uniting their strengths, imaging using the MINFLUX concept faces the challenges of both STED and PALM/STORM microscopy. Firstly, establishing a reliable molecular state switching is necessary, which was addressed by the use of stochastically blinking dyes and conditional activation. Secondly, generating a clean excitation intensity minimum for low photon count emission from the emitter. This goes along with minimizing background luminescence effects from the sample. So far, the presence of background photons in MINFLUX experiments, which are indistinguishable from fluorescence signal photons, led to the requirement of high photon numbers, i.e. >100 photons, to achieve molecular localization precision [22]. Conceptually,

however, the MINFLUX localization method does not require this many photons to achieve a 1 nm localization precision.
The challenge of high localization precision with a low number of detected photons can be faced best by using a double lens system, i.e. 4Pi-optics, for the generation of the excitation diffraction pattern. In the 4Pi-optics, counter propagating spherical wave front caps can generate the smallest interference pattern, i.e. minimum fringe separation, optimizing the localization precision determining parameter: the curvature of the excitation intensity profile at the intensity minimum.
The aim of the work presented in this thesis was to improve the axial localization precision and resolution in MINFLUX by implementing a 4Pi-optics illumination scheme. With this novel setup, we achieve molecular localization ($\sim \lambda/500$) precisions with as little as 20 photons. When measuring more photons (in the order of several hundreds) this system would theoretically allow localization precisions around one Ångström. However, we are limited by vibrations and thermal drift and therefore achieve a maximum localization precision in the range of 0.3 to 0.6 nm. By measuring with less than 700 photons we were able to resolve axial structures in deoxyribonucleic acid (DNA) origami nanorulers distanced by 10 nm with a localization precision of less than 2 nm. No other fluorescent microscopy method has previously achieved such high axial localization precision with this few detected photons.

1.1 Basic concept of MINFLUX

MINFLUX is based on the use of a scannable, structured illumination intensity pattern for fluorescence excitation [22]. The intensity minimum of this pattern serves as point of reference for the localization of the emitter. Without loss of generality, it can be assumed that the intensity around the minimum x_0 can be approximated with a parabolic function with curvature a and scaling intensity I_0. Thus, the intensity pattern along one dimension, e.g. x-axis, is defined by:

$$I(x, x_0) = \frac{1}{2} I_0 \, a(x - x_0)^2 \tag{1.1}$$

In order to locate a fluorescent emitter positioned at x_{em} in one dimension, the illumination pattern can be scanned along a range L from position x_L to x_R, as illustrated in figure 1.1(a). Here, it is assumed that the fluorescent emitter is located within this interval ($x_L < x_{em} < x_R$). The amount of detected photons depends on statistical processes related to both the emitter and the microscope. The relevant photo-physical properties of the emitter are its absorption coefficient ϵ_{abs} and fluorescence quantum yield ϕ_{fl} while the microscope parameters are combined into

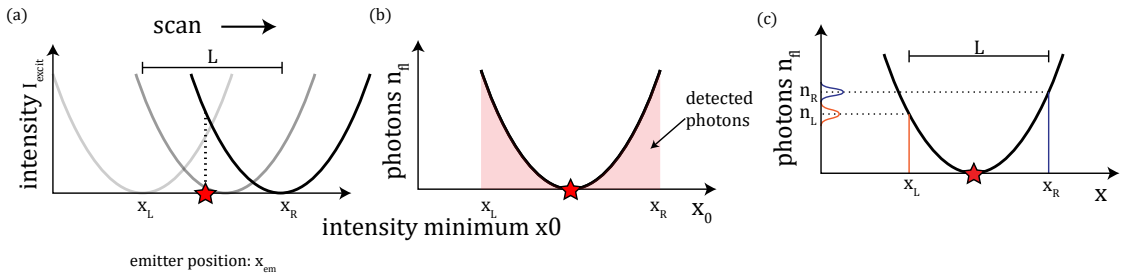

Figure 1.1: Localization principle of 1D MINFLUX. (a) Scan of an excitation profile with an intensity minimum along the range L between x_1 to x_2. A fluorescent emitter is positioned at x_{em}. The excitation profile in close proximity to the intensity minimum is approximated as a parabolic function, which is shown for three different scan positions. (b) The detected photons feature exactly the shape of the excitation profile and the emitter position can be extracted by finding the position of minimal photon counts i.e. $x_{em} = \min(\bar{n}_{fl})$. (c) When the shape of the excitation pattern is known, two single measurement points at known separation $L = |x_R - x_L|$ are sufficient to extract the position of the emitter.

the detection efficiency c_{det} [29]. Thus, the detected photons monotonically increase with increasing distance between the emitter x_{em} and the intensity minimum x_0. Assuming linear excitation, the mean detected fluorescence photons $\bar{n}_{fl}$ are defined by:

$$\bar{n}_{fl}(x_{em}, x_0) = c_{det}\phi_{fl}\epsilon_{abs} \cdot \frac{1}{2} I_0\, a\, (x_{em} - x_0)^2 \tag{1.2}$$

$$= \alpha \cdot \frac{1}{2} I_0\, a\, (x_{em} - x_0)^2 \tag{1.3}$$

The mean detected fluorescence photons follow exactly the shape of the excitation pattern, scaled by a factor α, which combines c_{det}, ϕ_{fl} and ϵ_{abs} (figure 1.1(b)). Consequently, the emitter position is precisely defined by the position in the scan at which minimal fluorescence photon counts are detected: $x_{em} = \min(\bar{n}_{fl})$.
Since the parabolic shape of the expected photons is described by two parameters, one can interpolate the emitter position based on only two targeted exposures. One exposure minimum is positioned to either side of the emitter (x_L and x_R) with a separation of $L = |x_R - x_L|$ (figure 1.1(c)). An estimation of the emitter position ($\bar{x}_{em}$) can obtained by solving the quadratic equation:

$$\bar{x}_{em} = L \left(\frac{1}{1 + \sqrt{\frac{\bar{n}_R}{\bar{n}_L}}} - \frac{1}{2} \right) \tag{1.4}$$

It is important to note that the resulting position depends on the ratio of the two photon counts measured, but not on their magnitude. Thus, the estimated position is independent from the photon emission processes of the emitter or illumination

parameters like intensity or wavelength [22].
Since the measured photon counts n_L and n_R are expected mean photon counts of the underlying Poissonian statistics of fluorescence emission and detection, the calculated positions fluctuate around the expected value of the position. In order to estimate the variance of the mean position, the Poissonian error of the expected photon counts has to be considered: $\sigma_{n_L} = \sqrt{\bar{n}_L}$ and $\sigma_{n_R} = \sqrt{\bar{n}_R}$.
Once the emitter is illuminated at the two defined positions and fluorescence photons are detected, the information content of the measurement is defined. Thus, there exists an absolute lowest value for the localization precision of the measurement. Balzarotti *et al.* have applied a statistical model to the MINFLUX process and derived position estimators, which extract the information of the position from the measured photons most efficiently [22]. For example, the maximum likelihood estimator determines the position which describes with highest probability the photon counts measured for a MINFLUX measurement and noise model. For unbiased estimators, which find on average the true emitter position, the lowest obtainable localization uncertainty is given by the Cramér-Rao bound (CRB). With $N = \bar{n}_L + \bar{n}_R$ being the sum of the measured photons, the CRB for a one-dimensional (1D) MINFLUX localization, as described in figure 1.1, is expressed as:

$$\sigma_{1D,CRB}(x_{em}) = \frac{L}{4\sqrt{N}} \left(1 + \left(\frac{x_{em}}{L/2}\right)^2\right) \tag{1.5}$$

The localization uncertainty reaches a minimum if the emitter is placed exactly between the two exposures, i.e. $x_{em} = 0$:

$$\sigma_{1D,CRB}(0) = \frac{L}{4\sqrt{N}} \tag{1.6}$$

The localization uncertainty is solely determined by the separation of the two exposures L and the inverse square root of the detected photons. The inverse square root of detected photons is a dependency shared also by centroid-fitting localization schemes, like camera-based localization. In camera-based localization, however, the uncertainty depends on the size of the diffraction spot on the camera, i.e. the shape of the detection PSF, which is ultimately limited by the wavelength and the numerical aperture of the imaging system. In MINFLUX, the uncertainty instead depends on the magnitude of the adaptable L-value, which in principle can be chosen arbitrarily small. Consequently, MINFLUX allows scalable localization precision and, when implemented in a iterative localization scheme (see section 1.1.1), the inverse square root law can be circumvented [24].

1.1.1 Iterative MINFLUX

Iterative MINFLUX allows reduction of the photon budget required for molecular localization precision compared to a single measurement [24]. This approach consists of a series of subsequent MINFLUX measurements in which the MINFLUX parameters are updated at each iteration. Iterative MINFLUX does not require measuring more photons to achieve a higher localization precision, which improves by the square root of N. Instead, it reduced the spatial scale of the L-value of the localization scheme and benefits from the linear relation between L and $\sigma_{1D,CRB}$.
In each MINFLUX iteration two MINFLUX parameters are updated, starting from user-defined values in the first step. Firstly, the positions of the two exposures are placed symmetrically around emitter position estimated in the previous iteration. Second, the L-value is decreased to a multiple (ϵ) of the uncertainty of the preceding iteration. For the i-th step this leads to: $L^{(i)} = \epsilon \cdot \sigma^{(i-1)}$. Note that for $\epsilon = 4$ the emitter is located with a probability of 96 % in the range defined by $L^{(i)}$.
In order to estimate a lower value of the uncertainty, it is assumed that the emitter is positioned exactly between the two exposures in every localization step, i.e. $x_{em} = 0$. Consequently, the uncertainty of the i-th MINFLUX step $\sigma^{(i)}$ is defined by equation 1.6, whereby L and N are treated as iteration step dependent parameters from now on. $\sigma^{(0)}$ denotes the starting localization precision of the imaging system. Rewriting the uncertainty as function of the successive localization parameters leads to:

$$\sigma^{(i)} \geq \frac{L^{(i)}}{4\sqrt{N^{(i)}}} = \frac{\epsilon\,\sigma^{(i-1)}}{4\sqrt{N^{(i)}}} = \frac{\epsilon^2\sigma^{(i-2)}}{4^2\sqrt{N^{(i)}\,N^{(i-1)}}} = \frac{\epsilon^i}{4^i}\frac{\sigma^{(0)}}{\sqrt{N^{(i)}N^{(i-1)}...N^{(1)}}} \tag{1.7}$$

Furthermore, one can assume that the number of photons detected in every step i is equal. By introducing the total number of detected photons in all steps $N = \sum_{k=1}^{i} N^{(k)}$, it follows that $N^{(k)} = {}^{N}/_{k}$. The uncertainty can then be rewritten as:

$$\sigma^{(i)} \geq \frac{\epsilon^i}{4^i}\frac{\sigma^{(0)}}{\sqrt{{N^{(i)}}^i}} = \frac{\epsilon^i}{4^i}\frac{\sigma^{(0)}}{\sqrt{\left(\frac{N}{i}\right)^i}} = \left(\frac{\epsilon}{4\sqrt{\frac{N}{i}}}\right)^i \sigma^{(0)} \tag{1.8}$$

In order to evaluate the number of iteration steps i at which the uncertainty of the localization becomes minimal for the assumptions mentioned above, one has to differentiate equation 1.8 with respect to i and zero the resulting expression:

$$\frac{d\,\sigma^{(i)}}{d\,i} \stackrel{!}{=} 0 \rightarrow i = \frac{16}{\epsilon^2 e}N \tag{1.9}$$

Inserting the minimal number of iterations into equation 1.8 leads to

$$\sigma^{(i)} \geq e^{-\frac{8}{\epsilon^2 e}N}\sigma^{(0)} \propto \sigma^{(0)}e^{N} \tag{1.10}$$

From equation 1.10 it follows that estimating the emitter position using iterative MINFLUX results in a localization uncertainty that depends exponentially on the total photon counts. This stands in strong contrast to methods for single molecule localization, such as PALM/STORM-type, which scale solely with the square root of the number of detected photons. In conclusion, to circumvent the square root law, it is crucial to perform iterative MINFLUX measurements. According to the current state of scientific knowledge, adaptive MINFLUX measurements have so far exclusively been performed with focused illumination patterns [24, 27, 28].
Yet, the exponential relation derived here is limited, to a certain extent, by experimental conditions. In particular, by the detection of background photons. Lowering the L-value results in an increase of the excitation intensity to maintain a constant photon flux throughout the measurement. Hence, laser intensity dependent processes (e.g. luminescence), which generate photons indistinguishable from fluorescence photons, become more probable. Consequently, in the experiment it is not guaranteed that the measured photon exclusively stems from the investigated emitter. In order to address these undesired background photons, the measurement scheme requires adaptation, as discussed in the following chapter.

2 Theoretical background

In this chapter the concept of the 1D localization in MINFLUX is presented under the consideration of background photons. In the presence of background counts, the performance of MINFLUX becomes dependent on various illumination pattern, e.g. the point spread function (PSF) (section 2.1). Therefore, PSF calculations were performed to evaluate the optimal illumination scheme for a 1D MINFLUX localization, which is achieved by 4Pi-optics (section 2.2). This section ends with a comparison of the localization performance between experimentally realized MINFLUX microscopes and the postulated double objective lens (4Pi-) MINFLUX microscope (section 2.2.2). The possible implementation of a 3D localization in a 4Pi-MINFLUX setup is described in section 2.3.

2.1 1D localization in MINFLUX using three exposures

2.1.1 Detected photons and background contributions

In addition to fluorescence signal photons stemming from an illuminated emitter (equation 1.3), background photons are detected under real experimental conditions. The background photons are caused by other emitting sources, besides the emitter investigated, or stem from the studied emitter due to a residual excitation intensity in the minimum. Thus, it can be assumed that the background photons are independent from the position if the intensity minimum; hence, they exhibit a constant photon offset. Further, it is assumed that only a single emitter is present in the investigated sample volume. Under typical experimental conditions, three major processes contribute to the background signal:

1. **Illumination intensity dependent emission of luminescence photons that do not stem from the emitter:** It is characterized by the product of excitation and detection probability per illuminated intensity unit, β:[1]

$$\bar{n}_{lum} = \beta I_0 \tag{2.1}$$

[1]It is assumed that the luminescence photon flux remains constant in the sample, is linearly dependent on the excitation intensity, and that its emission occurs primarily in the focal volume.

2. **Dark current noise of the detector:** $\bar{n}_{r.o.}$
3. **Illumination intensity dependent fluorescence photon emission of the emitter:** These photons stem from residual excitation intensity in the minimum caused by imperfect destructive interference. The magnitude of these background photons is defined by the product of the fraction b of the illuminated intensity I_0 and the statistical parameter of both emitter and microscope α , which are defined by equation 1.3:

$$\bar{n}_{fl,bg} = \alpha I_0 b \tag{2.2}$$

Based on the imperfect destructive interference, which leads to the third background contribution, the illumination pattern of the i-th exposure, which is defined by equation 1.1, rewrites to:

$$I_i(x, x_{0,i}) = I_0 \left(\frac{1}{2} a(x - x_{0,i})^2 + b \right) \tag{2.3}$$

Thus, the mean fluorescence photon counts of the emitter measured with the i-th exposure are defined by:

$$\bar{n}_{i,fl}(x_{em}, x_0) = \alpha\, I_0 \left(\frac{1}{2}\, a\, (x_{em} - x_{0,i})^2 + b \right) = \bar{n}_{i,sig} + \bar{n}_{i,fl,bg} \tag{2.4}$$

The total number of measured photons in the i-th exposure ($\bar{n}_i$) can be rewritten as the sum of the fluorescence signal photon ($\bar{n}_{i,sig}$) and the total sum of all background photons. Since the detector cannot distinguish the source of the background photons all three contributions are summarized in a single parameter for the background photons $\bar{n}_{i,bg}(I_0)$. This leads to mean total photon counts of:

$$\bar{n}_i(x_{em}, x_{0,i}, I_0) = \alpha\, I_0 \left(\frac{1}{2} a(x_{em} - x_{0,i})^2 + b \right) + \bar{n}_{lum} + \bar{n}_{r.o.} \tag{2.5}$$

$$= \frac{1}{2}\, \alpha\, I_0\, a(x_{em} - x_{0,i})^2 + \bar{n}_{bg}(I_0) \tag{2.6}$$

$$= \bar{n}_{i,fl.sig}(x_{em}, I_0) + \bar{n}_{bg}(I_0) \tag{2.7}$$

The background photons ($\bar{n}_{bg}(I_0)$) of equation 2.7 lead to a third parameter (constant y-axis offset) of the so-called photon count parabola, which is further defined by the parabolic curvature ($\frac{1}{2}\, \alpha\, I_0\, a$) and the emitter position offset (x_{em}). Consequently, the previously-derived emitter position obtained with two exposures (equation 1.4) no longer leads to an unbiased position estimation. Further, the localization uncertainty according to equation 1.5 is underestimated. To tackle this problem, a third exposure must be included in the localization process.

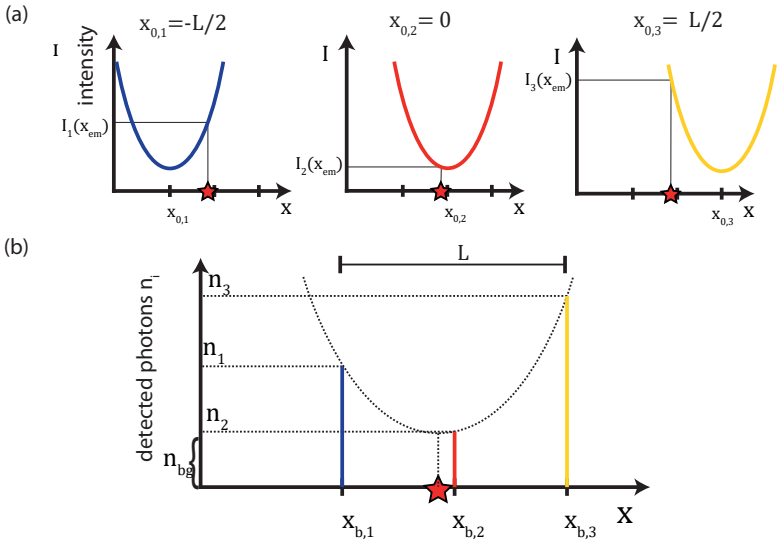

Figure 2.1: 1D MINFLUX localization using three exposures. (a) shows the excitation intensity profiles for the single exposures i. They have the same shape but differ in the position of the minimum according to equation 2.10. (b) shows the total detected photons of signal and background, which are plotted at the respective position of the minimum. It is shown illustratively how the position of the emitter can be determined by fitting a parabola to the measured photon counts and determining the minimum position of the parabola. Only background photon counts are measured in the minimum of the parabola.

For the sake of readability, from equation 2.11 onward, mean detected photons are referred to as n_i instead of $\bar{n}_i$.

2.1.2 Position estimation

To achieve an unbiased position determination the minimum of a third exposure can be placed in the center of the initially introduced two exposures, which are separated by L. Without loss of generality the position of the middle exposure can be set to zero, and the resulting minimum positions are defined by:

$$x_{0,1} = -L/2 \tag{2.8}$$

$$x_{0,2} = 0 \tag{2.9}$$

$$x_{0,3} = L/2 \tag{2.10}$$

In figure 2.1(a) the illumination parabolas of the three exposures are shown. The measured total photon counts of each exposure i is shown in figure 2.1(b). Each of the three detected photon counts, n_1, n_2 and n_3, consists of the sum of both signal and background photons, as defined in equation 2.7, with the minimum positions defined by equation 2.8 to 2.10.
In order to determine the emitter position with the three measured photon counts, firstly, the curvature and the offset of the y-axis are eliminated by taking the ratio

of the photon count differences between the right-to-center and the left-to-center exposure.

$$\frac{n_1 - n_2}{n_3 - n_2} = \frac{-2x_{em}\,{}^{L}\!/_{2} + ({}^{L}\!/_{2})^2}{2x_{em}\,{}^{L}\!/_{2} + ({}^{L}\!/_{2})^2} \tag{2.11}$$

Secondly, the expression is solved for the emitter position x_{em}:

$$x_{em} = \frac{L}{4}\frac{n_3 - n_1}{n_1 + n_3 - 2n_2} \tag{2.12}$$

Note that this position is only dependent on the number of measured photons and the separation L of the two outer exposures, which is from now on referred to as L-value.

2.1.3 Localization uncertainty

In order to approximate the uncertainty the emitter position estimation based on equation 2.12, the formula for Gaussian error propagation is applied. Every mean detected photon count n_i has a Poisson error of:

$$\sigma_{n_i} = \sqrt{n_i} \tag{2.13}$$

For the estimation of the photon statistical error, it is assumed that the L-value has no error. Thus, the localization uncertainty becomes:

$$\sigma_{1D}(x_{em}) = \sqrt{\left(\frac{\partial x}{\partial n_1}\cdot\sigma_{n_1}\right)^2 + \left(\frac{\partial x}{\partial n_2}\cdot\sigma_{n_2}\right)^2 + \left(\frac{\partial x}{\partial n_3}\cdot\sigma_{n_3}\right)^2} \tag{2.14}$$

$$= \frac{L}{2}\frac{\sqrt{(n_2 - n_3)^2\cdot n_1 + (n_3 - n_1)^2\cdot n_2 + (n_1 - n_2)^2\cdot n_3}}{(n_1 + n_3 - 2n_2)^2} \tag{2.15}$$

By assuming that the emitter position coincides with the middle exposure ($x_{em} = 0$), which is guaranteed in the case of iterative MINFLUX, the two outer exposures are equal ($n_1 = n_3$) and equation 2.15 can be simplified to:

$$\sigma_x(0) = \frac{L}{8}\frac{\sqrt{2n_1}}{n_1 - n_2} \tag{2.16}$$

Note that for the centered emitter, the background photons counts in all three exposures are directly probed by the middle exposure: $n_2 = n_{bg}$.
In order to reformulate the photon counts n_i in parameters which describe the whole measurement process, we introduce two new parameters:

- Total photon number N, with $N = \sum_{i=1}^{3} n_i$

- Signal-background-ratio ($SBR(x_{em}, L)$) of the two outer exposures:[2]

$$SBR(x_{em} = 0, L) = \frac{n_{1,fl.sig} + n_{3,fl.sig}}{n_{1,bg} + n_{3,bg}} = \frac{n_{1,fl.sig}}{n_{1,bg}} = \frac{n_1 - n_2}{n_2} \tag{2.17}$$

The values of the SBR can range from zero (no signal photon counts) to infinity (no background photon counts). Using the photon count definition (with neglected detector dark current) of equation 2.7, the SBR can be reformulated as the ratio of curvature and y-axis offset of the photon count parabola scaled by L^2:

$$SBR(0, L) = \frac{\alpha \frac{1}{2} I_0 \, a \, (L/2)^2}{\alpha I_0 b + \beta I_0} = \frac{\frac{1}{2} a}{\alpha \, b + \beta} \left(\frac{L}{2}\right)^2 \tag{2.18}$$

The measured photon counts n_i of the i-th exposure can be rewritten in terms of N and $SBR(0, L)$.

$$n_1 = n_3 = N \frac{SBR(0, L) + 1}{2SBR(0, L) + 3} \tag{2.19}$$

$$n_2 = \frac{N}{2\,SBR(0, L) + 3} \tag{2.20}$$

In order to parameterize the localization uncertainty σ_{1D} in terms of L, N and SBR, the stated photon count definitions are inserted into equation 2.16. This leads to the following expression for the localization uncertainty that arises from photon statistics and background photon contributions:

$$\sigma_{1D}(0, L, N, SBR(L)) = \frac{L}{4\sqrt{N}} \sqrt{1 + \frac{3}{2} \frac{1}{SBR(0, L)}} \sqrt{1 + \frac{1}{SBR(0, L)}} \tag{2.21}$$

As was pointed out by Gwosch *et al.*, the background contributions affect the iterative MINFLUX such that the L-value should not be decreased below an optimal value [24]. At this optimum, the uncertainty per number of detected photons becomes minimal.

Position estimation with minimal localization uncertainty

In the following, we want to verify, whether the position estimation in equation 2.12 can achieve the uncertainty σ_{1D} of equation 2.21 for different number of detected photons. We determined the position uncertainty by calculating the standard deviation of multiple MINFLUX localizations with statistically-simulated number of detected photons. The MINFLUX localization was parameterized by an L-value of 10 nm, a total number of detected photons N (varied between 5 and 200), and

[2] The total SBR, which considered all measured photons of the MINFLUX measurement, differs by a factor 2/3 from the SBR defined above.

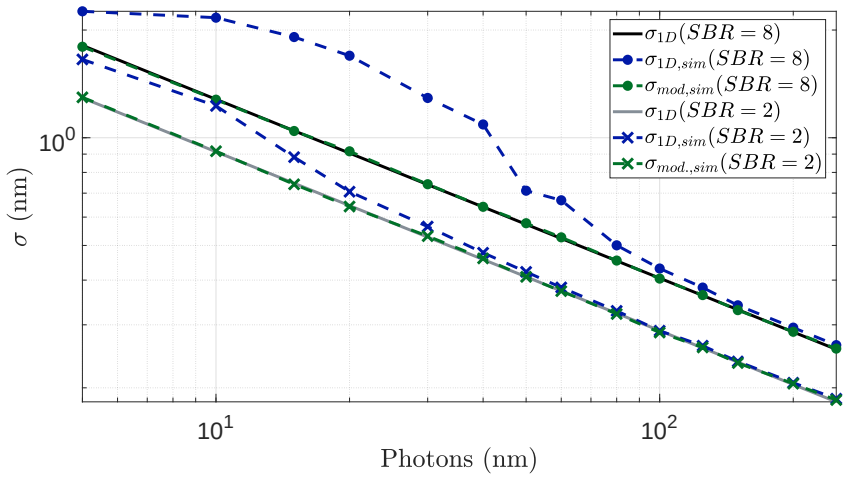

Figure 2.2: Comparison of position estimator Simulation of the position estimator uncertainty from two different estimators (normal estimator equation 2.12 (blue) and modified estimator equation 2.23 (green) for two different SBR values (2 (dots) and 8 (crosses)). The deviation of the normal estimator in the low photon regime is apparent and a deviation of 0.1 nm occurs for SBR=2 (8) at 60 (15) photons, respectively.

a SBR-value (varied between 2 and 8). A MINFLUX localization was simulated by determine three randomly generated photon counts according to three Poisson statistics with mean values defined by the equations of the mean expected photon counts (equation 2.19 and 2.20). Afterwards, the position was calculated according to equation 2.12 and the standard deviation was determined based on 10000 repeats of this procedure.

In figure 2.2 the results of the uncertainty ($\sigma_{1D,sim}$) are shown together with the uncertainty value of the photon statistics (σ_{1D}). When comparing the results, one can state that the simulated uncertainty does not achieve the uncertainty of the photon statistics but rather approximates it asymptotically for larger photon counts. Further, at lower values of the SBR higher photon counts are required to reach the uncertainty of the photon statistics. Similar findings have been observed by Balzaroitti *et al.* for the maximum likelihood estimator used in the first realization of a two-dimensional (2D) MINFLUX setup [22].

For repeated MINFLUX measurements of the same emitter with the same measurement settings, we can modify the position calculation of equation 2.12 by replacing the denominator with the averaged value gained from all repeats. Thus, the information of all repeats is used to calculate the curvature of the photon count parabola. The curvature ($1/2 \cdot a$) can be determined from the SBR defined in equation 2.18. Hereby, we considered again the centered configuration with $n_2 = b$. The mean

curvature can be calculated with the mean photon counts from all repeats $< n_i >$ for each of the three exposures i, as follows:

$$< \frac{1}{2}a >= \frac{2(< n_1 > + < n_3 > -2 < n_2 >)}{L^2} \tag{2.22}$$

Next, this equation is solved for the term in the brackets and inserted in the denominator expression of equation 2.12. Finally, the modified position estimator is defined by:

$$x_{em,mod} = \frac{n_3 - n_1}{2L < \frac{1}{2}\, a >} \tag{2.23}$$

The emitter position is now determined with the two outer exposures of each measurement (nominator). The influence of the middle exposure is represented, as averaged value, in the mean curvature. Due to the lowest photon count number in the middle exposure, statistical fluctuations of this exposure had contributed with a large relative error in the low photon count regime.
Performing the same simulation, but with the position estimator introduced above, reveals that the uncertainty values of the modified estimator ($\sigma_{mod,sim}$) are similar to the values of the uncertainty of the photon statistics over the whole range of investigated number of photons (green curves in figure 2.2).
The repeats of the simulation with same conditions can be seen as an analogy to repeating MINFLUX measurements with identical experimental parameters. In order to prevent an additional bias from the position calculation, we analyzed MINFLUX measurements of a single emitter (MINFLUX tracing) with the modified estimator. Hence, when no additional noise contributions arising from the microscope are present, the MINFLUX measurements should achieve the localization uncertainty $\sigma_{1D,sim}$.

Smallest achievable localization uncertainty considering background photons

As pointed out by Gwosch *et al.*, the existence of background photons limits the MINFLUX measurement to an optimal L-value below which the uncertainty per number of detected photons increases [24]. In iterative MINFLUX measurements the L-value should converge towards this optimal value. In the following, formulas for the optimal L-value, the corresponding value of the SBR, and the uncertainty per number of detected photons are derived analytically for the quadratic approximation of the excitation profile. Since the quadratic approximation is only valid for a certain range around the minimum, we present numerical results for the most general case of a standing wave excitation pattern.

A) Quadratic excitation profile

The dependency of the SBR with regard to L, which is independent from the exact parameters of the excitation profile, can be derived by relating the SBR to a reference SBR at a reference L-value (L_0). The ratio of the two SBR-values is equal to the ratio of their respective fluorescence signal photon counts. With $n_{fl.sig} = n_{1,fl.sig} = n_{3,fl.sig}$ this leads to:

$$\frac{SBR(0,L)}{SBR(0,L_0)} = \frac{{}^{n_{fl.sig}(L/2)}/_{n_{bg}}}{{}^{n_{fl.sig}(L_0/2)}/_{n_{bg}}} = \frac{n_{fl.sig}({}^{L}/_{2})}{n_{fl.sig}({}^{L_0}/_{2})} \tag{2.24}$$

Using the definition of the fluorescent signal photon counts $n_{fl.sig}$ for the parabolic excitation profile (equation 1.3) the SBR simplifies to

$$SBR(0,L) = SBR(0,L_0)\frac{\alpha\frac{1}{2}I_0\,a\left(\frac{L}{2}\right)^2}{\alpha\frac{1}{2}I_0\,a\left(\frac{L_0}{2}\right)^2} = SBR(0,L_0)\left(\frac{L}{L_0}\right)^2 \tag{2.25}$$

Likewise as the excitation profile, the SBR depends on the quadratic ratio of the two referenced L-values. Inserting this term into equation 2.21 leads to the formula of the localization uncertainty with parameters L, N, $SBR(0,L_0)$ and L_0.

$$\sigma_{1D}(0) = \frac{L}{4\sqrt{N}}\sqrt{1+\frac{3}{2}\frac{1}{SBR(0,L_0)\left(\frac{L}{L_0}\right)^2}}\sqrt{1+\frac{1}{SBR(0,L_0)\left(\frac{L}{L_0}\right)^2}} \tag{2.26}$$

The SBR-dependent correction factor ($\delta(SBR)$, product of both square root terms) increases with decreasing L-value ($\delta(SBR) \propto {}^{1}/_{L^2}$). This dependency counteracts the linear decrease of the background free uncertainty term of equation 1.6 for decreasing L-value and consequently leads to a minimal uncertainty. The L-value at which the uncertainty is minimal (L_{min}) can be calculated by finding the extreme point of equation 2.26. This leads to:

$$L_{min} = \sqrt[4]{\frac{3}{2}}\frac{L_0}{\sqrt{SBR(L_0)}} \tag{2.27}$$

Equally to the localization precision, the optimal L-value follows an inverse square root relation to the detected fluorescence photon counts $n_{fl}({}^{L_0}/_{2})$, since it holds that: $SBR(L_0) \propto n_{fl}({}^{L_0}/_{2})$. The calculation of the SBR at the optimal L-value can be performed by inserting equation 2.27 into 2.25, resulting in:

$$SBR(0,L_{min}) = 1.2 \tag{2.28}$$

Further, the value of the minimal achievable localization uncertainty for a given set of parameters ($x_{em} = 0$, L_0, $SBR(0, L_0)$ and N) is defined by:

$$\sigma_{1D,min}(0, L_0, SBR(0, L_0), N) = \frac{L_0}{4\sqrt{N}\sqrt{SBR(0, L_0)}} 2\left(1 + \sqrt{\frac{3}{2}}\right) \tag{2.29}$$

In conclusion, these findings help us to perform MINFLUX measurements with optimal parameters, by defining the L-value such that an optimal SBR-value is achieved. However, when larger L-values were used for referencing, the quadratic approximation breaks down. Therefore, we numerically analyze the relations for optimal settings in the standing wave approach. This will allow us to parameterize the optimal L-value in terms of the SBR evaluated at the maximum to minimum intensity.

B) Standing wave excitation profile

In an experimental illumination pattern of finite intensity the minimum is flanked to either side by a maximum. By assuming no optical aberrations, the pattern is defined to be symmetric with respect to the minimum. This leads to equal intensity values of the first side maxima. Without loss of generality, we can approximate the region between these two maxima by a standing wave. Its wavelength is defined by $\lambda_{st.w.} = 2 \cdot fwhm$. The full width at half maximum (fwhm) is evaluated around the minimum.[3] For example, two interfering counter propagating plane waves of wavelength λ_0 would create a standing wave with $\lambda^{st.w.} = 0.5\lambda_0$ (see figure 2.3(a)). The illumination intensity of the standing wave is defined by:

$$I^{st.w}(x) = I_0 \sin^2\left(\frac{2\pi}{2\lambda^{st.w.}} x\right) \tag{2.30}$$

The photons obtained from this illumination pattern including background photons are defined by:

$$n(x) = n^{st.w.}_{fl.sig}(x) + n_{bg} = \alpha I_0 \sin^2\left(\frac{2\pi}{2\lambda^{st.w.}} x\right) + n_{bg} \tag{2.31}$$

$$= \alpha I_0 \left(\frac{1}{2} - \frac{1}{2}\cos\left(\frac{2\pi}{\lambda^{st.w.}} x\right)\right) + n_{bg} \tag{2.32}$$

From the photon counts at the minimum and maximum position we can calculate the SBR that a MINFLUX localization would achieve with an L-value equal to the standing wave wavelength: $SBR(0, L_0 = \lambda^{st.w.})$. For comparison reason, this definition of the SBR-value might be more suitable, since it describes the quality of the illumination scheme independently from other illumination parameter, like the

[3] In case of a lateral donut PSF $\lambda^{st.w.}$ is equal the donut crest.

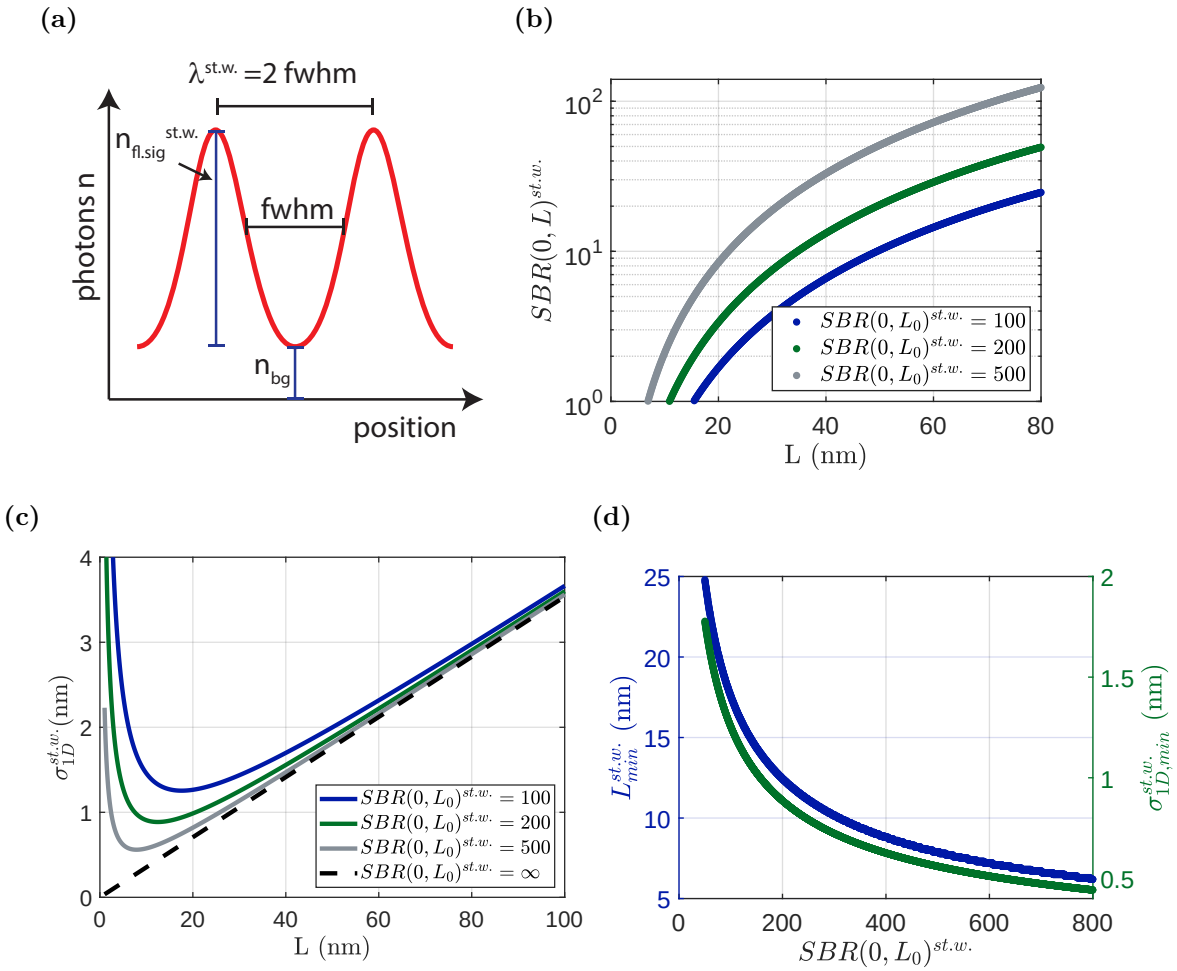

Figure 2.3: Evaluation of the minimal achievable localization uncertainty and L-value with background influence (a) Illumination intensity pattern of the two maxima flanking the minimum is approximated by a standing wave of wavelength $\lambda_{st.wave}$. Definition of the reference L-value (L_0) as the double full width half maximum of the intensity minimum. or the wavelength of the standing wave . (b) SBR in dependency of the L-values for different reference $SBR(0, L_0)$ (see legend). (c) Localization uncertainty as a function of the L-value for different reference SBR-values (see legend). With increasing SBR the minimal uncertainty is obtained at smaller L-values. (d) Value of the minimal uncertainty (green) and the corresponding L-value (blue) calculated for different reference SBR-values at L_0 (as shown in (c)). In both cases, an inverse square root relation between the respective parameter and the reference SBR can be stated (similar to equation 2.27 and 2.29). Calculations were performed with $N = 50$ and $L_0 = 250\,\text{nm}$ (motivated by later experimental conditions).

wavelength or the effectively used aperture. Inserting the definition of the fluorescence signal photons ($n_{fl.sig}^{st.w.}$) into the equation of the SBR progression (equation 2.24) leads to the most general form of the SBR.

$$SBR(0,L)^{st.w.} = SBR(0,L_0)\frac{\alpha I_0\left(\frac{1}{2}-\frac{1}{2}\cos\left(\frac{2\pi}{\lambda^{st.w.}}\frac{L}{2}\right)\right)}{\alpha I_0\left(\frac{1}{2}-\frac{1}{2}\cos\left(\frac{2\pi}{\lambda^{st.w.}}\frac{L_0}{2}\right)\right)} \tag{2.33}$$

This equation is valid for reference L-values (L_0) up to the wavelength of the standing wave. For $L_0 = \lambda^{st.w.} = 2fwhm$ this expression can be simplified to:

$$SBR(0,L)^{st.w.} = SBR(0,2fwhm)\frac{\alpha I_0\left(\frac{1}{2}-\frac{1}{2}\cos\left(\frac{2\pi}{2fwhm}\frac{L}{2}\right)\right)}{\alpha I_0\left(\frac{1}{2}-\frac{1}{2}\cos\left(\frac{2\pi}{2fwhm}\frac{2fwhm}{2}\right)\right)} \tag{2.34}$$

$$= SBR(0,2fwhm)\left(\frac{1}{2}-\frac{1}{2}\cos\left(\frac{2\pi}{2fwhm}\frac{L}{2}\right)\right) \tag{2.35}$$

This relation is plotted in figure 2.3(b) for different reference SBR-values ($SBR(0,L_0)$). The respective L-value-dependent localization uncertainty was evaluated by inserting the SBR as defined above into equation 2.21. The result is plotted in figure 2.3(c). These findings show, that the localization uncertainty exhibits a minimum when background counts are present. Further, a stronger increase in uncertainty can be stated towards lower L-values as compared to larger values. Thus, it is important not to set the L-value smaller than the optimal value. On the other hand, L-values larger than the optimal value ($\sim 25\,\%$) result only in minor increases in uncertainty. The value of the minimal uncertainty as well as the corresponding L-value were calculated for different referencing SBR-values (figure 2.3 (d)). Both values are coupled to the SBR with and inverse square root proportionality.

Conclusion

With this in hand, the quest of finding ideal experimental settings for high localization precision in MINFLUX with a low number of photons can be subdivided into two research tasks. Firstly, to maximize the achievable pattern $SBR(0,L_0)$. Secondly, to create the highest curvature in the intensity minimum by using the smallest wavelength of a standing wave, i.e. $fwhm$-value. The former originates primarily from e.g. beam aberrations, which lead to imperfect destructive interference, or sample impurities. Thus, it is left to the experimenter to find optimal conditions during the execution of specific measurement. The latter, however, can be tackled by means of the possible illumination schemes that give rise to different illumination PSF. This approach will be discussed in the following section.

2.2 4Pi-optics illumination scheme for 1D MINFLUX

2.2.1 PSF in single and double objective lens illumination schemes

In order to find the best illumination conditions for MINFLUX localization with the highest photon efficacy, we compared different illumination schemes with respect to their curvature in the intensity minimum. The curvature describes the rate at which the illumination intensity changes per length scale along the direction of localization. As previously introduced, the standing wave approach is a sufficiently good approximation for describing the range from the minimum until the first maximum on either side for any illumination PSF. When performing the quadratic approximation around the minimum of the standing wave intensity pattern (equation 2.30), the intensity can be simplified to:

$$I^{st.w.}(x) \approx I_0 \frac{1}{4} \frac{\pi^2}{(fwhm_{st.w.})^2} x^2 \tag{2.36}$$

Comparing this expression with equation 1.1, one can conclude the following two relations for the curvature a in the intensity minimum:

- $a \propto \frac{1}{fwhm^2_{st.w.}}$
- $a \propto I_0$

Hence, for maximal photon efficacy it is favorable that the spacing of minimum and maximum is very tight (minimizing $fwhm$) and that the objective lens focused the light primarily in the first side maximum (maximizing I_0 per illumination unit).
In the following, we present the results of illumination PSF calculations for single and double objective lens configuration and compare them with respect to the parameters mentioned above [30].

Single objective lens illumination

In order to realize a one-dimensional (1D) localization pattern in the lateral plane with a single objective lens, the back focal plane (bfp) of the objective lens is illuminated with two coherent beams at opposing positions, with respect to the center of the bfp, e.g. displaced along the x-axis. Destructive interference in the focal point can be achieved by setting the polarization of the beams perpendicular to the beam displacement direction, here y-polarization, and adding a relative phase delay of π to one of the beams. Further, the minimum is flanked by one or multiple side maxima to either side along the x-axis. The exact shape of the PSF, like the number of side maxima, depends, among other things, on the size of the two beams. An estimation of the $fwhm$ can be performed by considering two parameters for the illumination. Firstly, the relative aperture angle of both beams (defined by the distance of beam center to the optical axis — Abbe's sine condition). Secondly, the

effective illuminated area of the bfp, which is the effectively used aperture for the illumination.

The first parameter describes the angle of incidence (ϕ) of the wave vectors (k_1 and k_2) which arise from the center of each beam. The projection of this wave vector onto the lateral direction ($k_{i,lat}$) defines the fraction, with which both waves of wavelength λ interfere in the lateral plane: $k_{i,lat} = |k_i| \sin(\phi) = \frac{2\pi n_{med}}{\lambda} \sin(\phi)$. n_{med} denotes the refractive index of the medium. The corresponding wavelength is defined by: $\lambda_{lat} = \frac{\lambda_0}{n_{med} \sin(\phi)}$ (see figure 2.4).

The second parameter can be considered by a positive aperture correction term ($f^{lat}_{aper.,corr}$), which depends on the shape of the illumination beam and ranges between 1 (focused beams in the bfp) and ~ 1.5 (complete aperture illuminated).[4] Thus, we can write for the lateral $fwhm$:

$$fwhm_{lat} = \frac{1}{4}\lambda_{lat} \cdot f^{lat}_{aper.,corr} = \frac{\lambda_0}{4n_{med} \sin(\phi)} \cdot f^{lat}_{aper.,corr} \geq \frac{\lambda_0}{4NA} \tag{2.37}$$

Here, the numerical aperture (NA) was introduced with $NA = n_{med} \sin(\phi)$. The minimal $fwhm$ can be reached in case of widefield illumination whereby the beams are focused close to the edge of the entrance pupil. However, this configuration is still limited by the NA of the objective lens. The aperture angle for a 100x 1.44 oil objective lens is: $\sin(71.6°) = 0.95$. On the other side, this value is only 5 % smaller than the maximum achievable value of one.

In figure 2.4 the illumination PSF along the lateral (x-y) and axial (x-z) direction are shown for different beam sizes. The $fwhm$-values range from 115 nm (widefield illumination) to 173 nm (full aperture illumination). The widefield illumination scheme is applied in structured illumination microscopy (SIM) [31], whereas the full aperture illumination scheme can be used to create a 1D depletion pattern in STED microscopy by using a half moon phaseplate in the beam path of the STED laser [32].

Double objective lens illumination

One conceivable way to maximize the curvature is to interfere two beams such that their respective wave vectors are completely counter aligned, and the resulting interference pattern is coaligned to the direction of localization. This illumination scheme can be realized when a second equal objective lens is placed opposite to the first one and similar beams are illuminated along the optical axis of each objective lens. The propagating plane wave fronts (widefield illumination) or the converging spherical wave front caps (full aperture illumination) are counter aligned with respect

[4] The aperture correction term mainly represents the coherent sum of differently oriented waves segments in the focus.

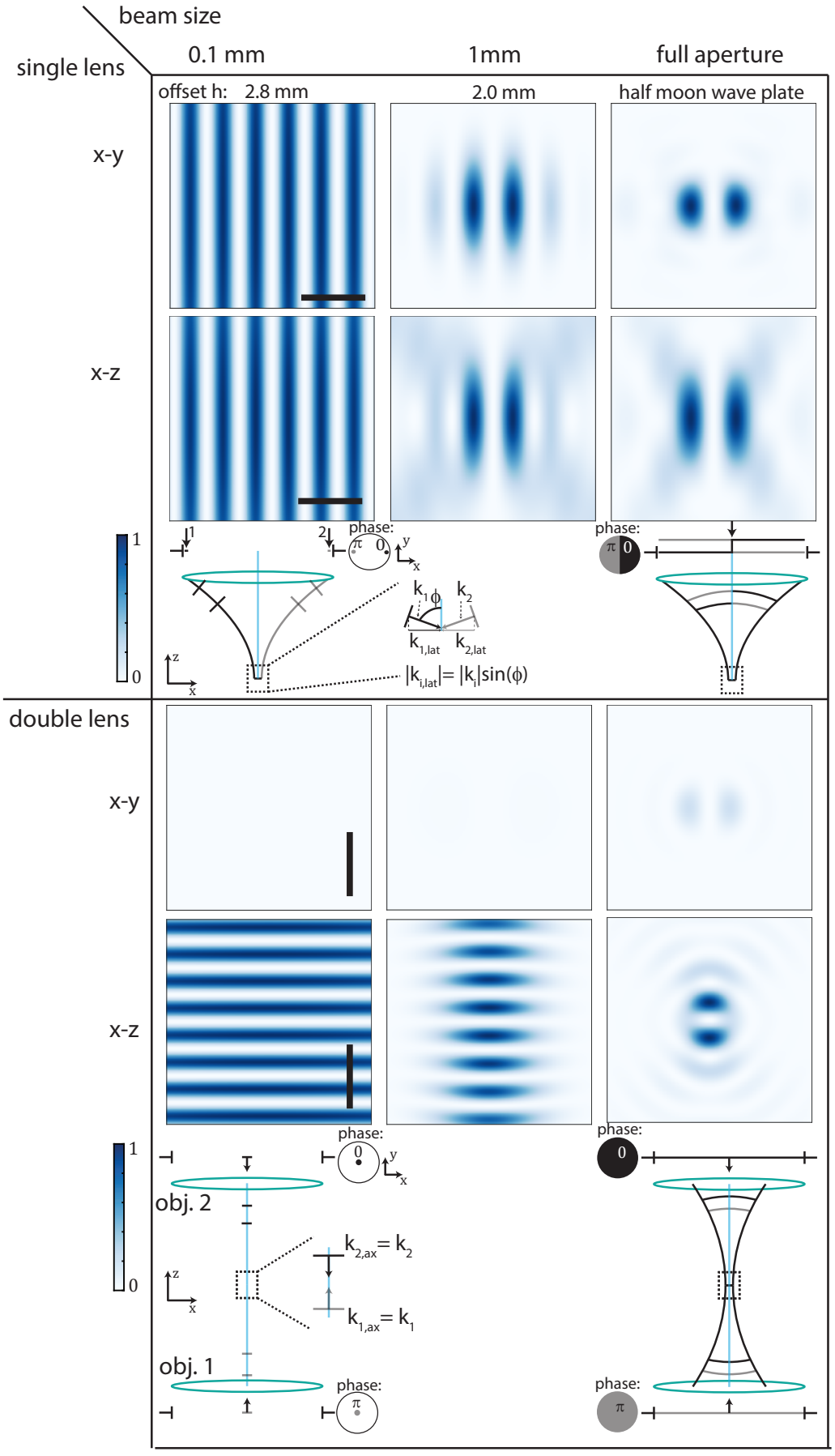
beam size
single lens
0.1 mm
1mm
full aperture
offset h: 2.8 mm
2.0 mm
half moon wave plate
x-y
x-z
1
0
phase:
k_1 ϕ
k_2
$k_{1,lat}$
$k_{2,lat}$
$|k_{i,lat}| = |k_i| \sin(\phi)$
double lens
obj. 2
obj. 1
$k_{2,ax} = k_2$
$k_{1,ax} = k_1$

Figure 2.4: Creation of an illumination PSF featuring an intensity minimum in single and double objective lens systems The x-y and x-z PSF were calculated for different illumination beam sizes ($fwhm$-value of a Gaussian beam located in the bfp of the objective lens). An intensity minimum is created by a phase difference of π between both two interfering beams or two segments of the beam wave front. Increasing the beam size reduces $fwhm$-value of the minimum but the peak intensity of the first side maxima increase. (a) A minimum along the lateral direction is created by displacing two beams from the optical axis or by a single beam in combination with a phase plate. The $fwhm_{lat}$-value is dependent on the projection of the wave vector of the beam wave front k onto the lateral direction and limited by the wavelength and the aperture angle (equation 2.37). $fwhm_{lat}$-value along the x-axis from left to right is: 115 nm, 152 nm and 173 nm. (b) In the double objective lens system (4Pi-optics) the illuminated beams are coaligned to the optical axis. The $fwhm_{ax}$-value is only limited by the wavelength (equation 2.38). $fwhm_{ax}$-values from left to right: 105 nm, 110 nm and 137 nm. Calculations were performed for a NA 1.44 oil objective lens (λ =640 nm). PSF were normalized to the respective maximum. Scale bar 500 nm.

to one from the opposing objective lens. A relative phase delay of boths beams of π, creates an intensity minimum in the focal plane with side maxima along the optical axis (see figure 2.4).

In case of the widefield illumination, the smallest $fwhm$-value can be achieved since the projection of the wave vector to the localization direction is one ($k_1 = k_{1,ax} = {}^{2\pi}/_{\lambda_{ax}}$). Consequently, the $fwhm$ is only limited by the effective wavelength of the beam in the focus medium ($\lambda_{ax} = \lambda_0/n_{med}$). Increasing the effective aperture used by a larger beam size enhances the focusing strength, and at the same time enlarges the $fwhm$-value along the axial direction. Similar to the single lens system, the resulting $fwhm$-value along the axial direction ($fwhm_{ax}$) must be corrected with an aperture-dependent correction term ($1 \leq f^{ax}_{aper.,\,corr} \leq 1.3$), and can be written as:

$$fwhm_{ax} = \frac{1}{4}\lambda_{ax} \cdot f^{ax}_{aper.,\,corr} = \frac{\lambda_0}{4n} \cdot f^{ax}_{aper.,\,corr} \geq \frac{\lambda_0}{4n} \tag{2.38}$$

We want to refer to the double lens system as a 4Pi-optics configuration since the term 4Pi microscopy is associated to a confocal scanning microscopy with two photon excitation using opposing lenses [33]. The $fwhm$-values range from 105 nm (widefield illumination) to 137 nm (full aperture illumination). The widefield illumination scheme was implemented for axial localization in the scope of standing wave microscopy [34], I^{5}M [35, 36] or modulation interferometry [37]. The full aperture illumination scheme was used in a 3D STED scanning microscope achieving isotropic resolution (isoSTED [38]). The results of the PSF calculation are given in the figure.

By comparing the results for the lateral with the axial $fwhm$-value, we conclude that with 4Pi-optics a 10 to 30 % smaller $fwhm$ can be achieved. A detailed simulation of the $fwhm_{ax}$-value in dependency of the beam size is shown in figure A.2. After

having shown that 4Pi-optics features the smallest $fwhm$, and thus the intensity profile with the highest curvature in the intensity minimum, we want to compare these values with values arising from current implemented MINFLUX illumination schemes.

2.2.2 1D performance of 4Pi-MINFLUX over existing MINFLUX schemes

In the following, PSF calculations were used to quantify the advantage of a focused 4Pi-optics illumination PSF used for 1D localization over the illumination PSF which were used for 2D and 3D localizations in exciting MINFLUX microscopes [22, 24, 30]. To date, 2D and 3D MINFLUX experiments were exclusively performed using a single objective lens for the illumination. For lateral localization, a donut shaped PSF was generated using a vortex phaseplate. For axial localization, a PSF termed tophat was generated using a half moon phaseplate. It has been shown that these PSF, when generated with the STED beam, are optimal for lateral and axial STED microscopy [25]. Consequently, they might exhibit a good performance as excitation pattern in MINFLUX. In 1D localizations using 4Pi-optics, a tunable parameter is the beam size ($fwhm_{beam}$). This parameter influences both the width of the interference pattern ($fwhm_{ax}$) and axial expansion of the interference pattern (confocal envelope). PSF simulation revealed that a good enough compromise between both quantities can be found for (figure A.2): $fwhm_{beam}$ =2.5 mm. This value was used in the following PSF calculation. A sketch of the three different illumination schemes and the resulting lateral and axial PSF are given in figure 2.5(a).

Results of PSF calculations Each PSF was evaluated with respect to the values for $fwhm$ and I_0 (see figure 2.5 or table 2.1). In 4Pi-optics, the counter propagating spherical wave front caps lead to a one-third smaller $fwhm$-value compared to the corresponding value of the donut pattern (see figure 2.5(a) and (b)). Additionally, the peak intensity is improved by the interference along the axial direction. Hence, the 4Pi PSF requires only one fourth (third) of the light dose which was required for the donut (tophat) PSF, to achieve equal values of I_0. Even when the source of background photons in an experiment is difficult to pinpoint, it can be assumed that a lower light dose produces fewer luminescent background photons. In conclusion, the 4Pi-optics PSF clearly outperforms the donut and tophat PSF with respect to both parameters.

When background photons are present, the photons required for one nanometer localization precision can be used as a comparative figure to determine the performance of the MINFLUX microscope. For this comparison, we first assumed equal

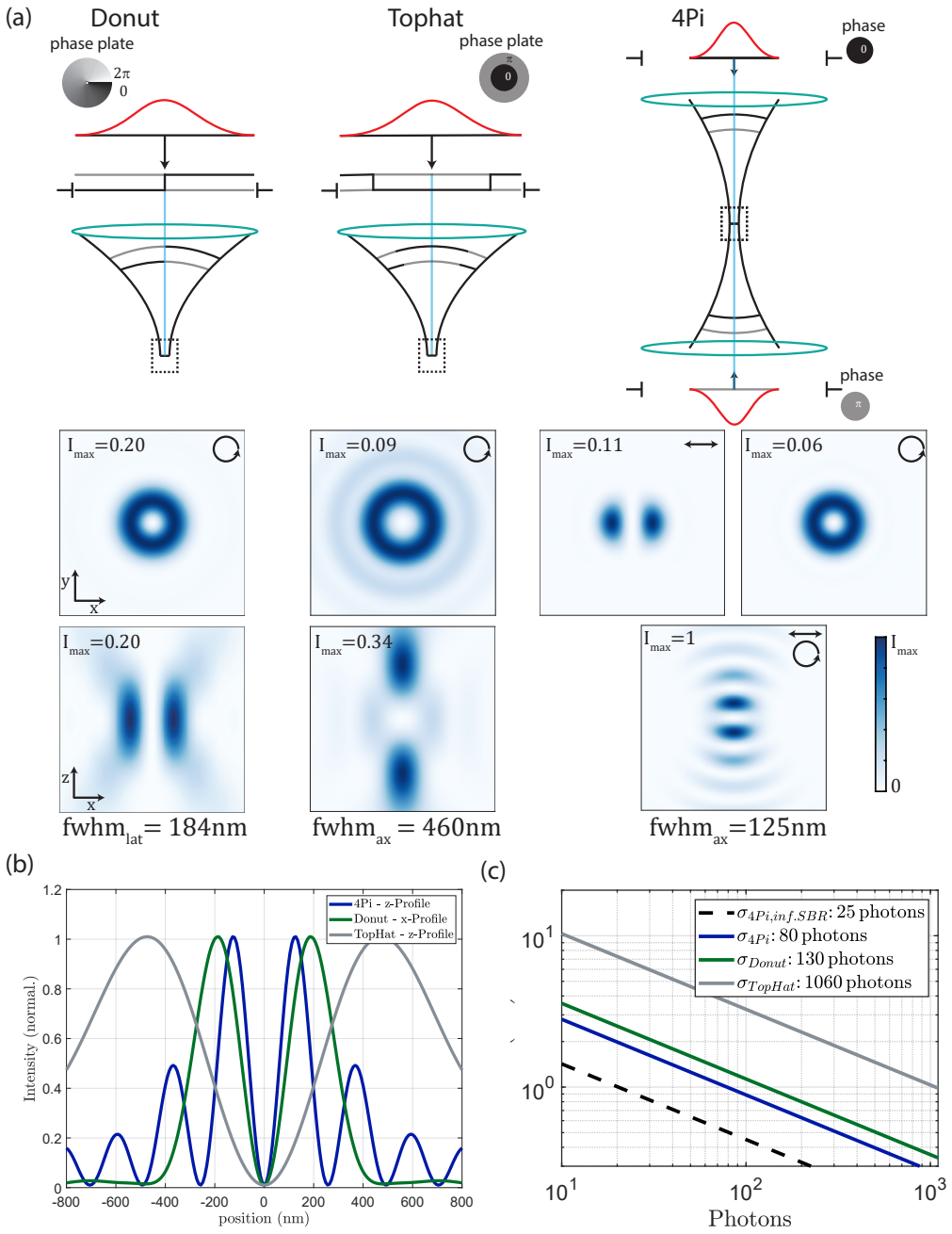

Figure 2.5: MINFLUX performance with different illumination PSF.(a) Sketch of three different illumination schemes (Donut, Tophat, 4Pi) with the lateral (x-y) and axial (x-z) PSF. The respective $fwhm$-value was evaluated for the minimum and along the x (donut) or z-direction (tophat and 4Pi). The intensity and the polarization of the illumination light are given in the respective PSF pattern. (b) Intensity profile of the PSF through the focus along the direction of localization (x-axis for donut and z-axis for tophat and 4Pi). (c) Localization uncertainty of the three different illumination schemes with $SBR = 100$ and at their respective optimal L-value (same calculation as in figure 2.3(d)). In the legend the photons for 1nm localization uncertainty are listed (equation 2.39 with σ_{1D} =1 nm). 4Pi-optics features minimal $fwhm$ and highest intensity peak for a given illumination unit. Assuming equal $SBR(L = 2 \cdot fwhm)$, 4Pi-optics requires 40 % less photons to achieve the same localization uncertainty compared to the donut. The simulated parameter are summarized in table 2.1. Calculations were performed for a NA 1.44 oil objective lens (λ =640 nm). Scale bar in (a) 500 nm.

reference SBR-values in all illumination PSF. Motivated by common experimental conditions, the intensity in the minimum is assumed to reach a value of 1 % of the respective intensity maximum.[5] This results in a SBR-value of 100 for MINFLUX measurements with $L = 2 \cdot fwhm$ (equation 2.17). Secondly, we calculated the optimal L-value of each illumination scheme according to the procedure used in figure 2.3. Finally, the localization uncertainty of the photon statistic including background photon contributions σ_{1D}, defined by equation 2.21 was calculated using the optimal L-value (L_{min}) and the respective SBR, derived from the standing wave approach ($SBR^{st.w.}(0, L_{min})$). The resulting localization uncertainty values are shown in figure 2.5(c).

Number of detected photons The photons required for 1 nm localization uncertainty can be extracted from the graph or can be calculated by the following equation (see equation 2.21):

$$N_{tot} = \left(\frac{L}{4\sigma_{1D}}\right)^2 \left(1 + {}^3\!/_2 \frac{1}{SBR(L)}\right)\left(1 + \frac{1}{SBR(L)}\right) \tag{2.39}$$

In conclusion, the benefit from the lower $fwhm$-value in 4Pi-optics reduces the photon number by 40 % with regard to the currently best experimentally implemented illumination PSF (donut). All numerical values are summarized in table 2.1.
A centroid-fitting localization microscope which uses a coherent double objective lens system could, under ideal conditions, achieve localization uncertainties limited by the quantum Cramér-Rao bound and defined by [39]:

$$\sigma_z \approx \frac{50\,\text{nm}}{\sqrt{N}} \tag{2.40}$$

Here, 2500 photons would be required to achieve single nanometer localization precision. In experiments, however, a finite SBR worsens the data acquisitions leading to an increase to more than 10000 photons required [40]. Even under ideal conditions, a centroid-fitting localization requires thirty times more photons than 4Pi-MINFLUX to achieve a localization precision of one nanometer.

SBR in 4Pi-optics It is in principle not guaranteed that despite a more technical-demanding 4Pi-optics setup, the background photons can be reduced to the same

[5] There as several reasons why a relative scaling of the background photons can be useful. For example when background photons stem from a residual illumination intensity in the minimum due to wave front aberrations. Both signal and background increase when the illumination intensity I_0 increases.

Simulations	Donut PSF	Tophat PSF	4Pi PSF
$fwhm$ (nm)	184	460	125
Maximum intensity (arb.u.)	0.2	0.34	1
L_{min} (nm) for $SBR(L_0) = 100$	26	65	18
Total photons for $\sigma = 1\,\text{nm}$ ($SBR(L_0) = 100$)	130	1050	80
Experimental results			
smallest L (nm)	50 [22]	100 [24]	section 4.4
lateral localization uncertainty:			
$\sigma_{2D,lat}$ (nm) / photons	1 / 650 [22]		
$\sigma_{3D,lat}$ (nm) / photons	2.6 /2000 [24]		
axial localization uncertainty:			
$\sigma_{3D,ax}$ (nm) / photons		1.8 / 2000 [24]	
$\sigma_{1D,ax}$ (nm) / photons			section 4.3
smallest resolved structure (nm)	6 [22]	50 [24]	section 5

Table 2.1: Simulated and experimental results of the MINFLUX performance for different illumination PSF. The simulated parameter are extracted from figure 2.5 Note that the 2000 photons of the 3D localization uncertainty ($\sigma_{3D,lat}$ and $\sigma_{3D,ax}$) is the total number of photons required for both lateral and axial localization.

relative value of the intensity maximum compared to the other two presented illumination schemes. In 4Pi-optics, a SBR, which is roughly 2 or 5 times smaller than the respective value of the donut or tophat PSF, can still be tolerated to achieve the same localization uncertainty for an equal number of detected photons.
On the other side, simulations of aberrated 4Pi PSF revealed that the value of the intensity minimum is relative insensitive with respect to asymmetries in the illumination (see figure A.3). A relative power difference between both beams of 30 % would lead to a SBR of 100. Similar findings apply to the polarization or the centering of the beams in the bfp. Wave front aberrations, like spherical or astigmatic aberration, become dominant when they reach a value of half the wavelength. These results promise that high SBR values can indeed be achieved with 4Pi-optics.

Experimental results The experimental localization uncertainty and resolution achieved for the donut and tophat PSF are listed in table 2.1. In order to encounter the molecular heterogeneity, experiments of 2D and 3D MINFLUX were performed with a larger L-value, which leads to a larger SBR ($\sim 2-5$). The number of detected photons required in 2D MINFLUX for 1 nm localization precision range around 300 per localization dimension. The 3D localization precision was stated for the iterative MINFLUX scheme, whereby in total for all iteration steps and for all dimensions 2000 photons were required. Hence, these experiments, and especially 3D MINFLUX,

still rely on a high number of photons to achieve a high localization precision.
With this thesis we want to experimentally prove that 4Pi-MINFLUX requires far fewer photons to reach molecular localization precision compared to all currently existing MINFLUX microscopes. This allows us to examine the MINFLUX localization process in the low photon regime (<100). We chose 4Pi-optics because it features the best starting condition, whereas it is left to the experimentalist to minimize the sample and microscope induced aberrations. In the next section, we want to present a possible expansion to 3D localization using 4Pi-optics.

2.3 3D localization in 4Pi-MINFLUX

Although the aim of the present thesis is to investigate the properties of the best possible optical configuration for MINFLUX localizations restricted to one dimension, it is shown in the following how the principle can be easily expanded to almost isotropic three dimensional localizations. First, we have a schematic look into the generation of a focused PSF in 4Pi-optics before the concept of tilted PSF is introduced and expanded to 3D. The requirements for the 3D localization laid the motivation for the experimental setup.

2.3.1 Tilted illumination PSF in 4Pi-optics

Counterpropagating waves in 4Pi-optics

The symmetry of the opposing objectives in 4Pi-optics, generates a diffraction pattern, which is point symmetric to the geometric focal point and mirror-symmetric to the focal plane. It is assumed that the illuminated beams propagate along the optical axis and have arbitrary but equal properties e.g. size, power or polarization. As a consequence, these symmetry properties ensure that there is always a segment of the beam which is completely counter propagating to a respective segment of the other beam.
This fact can be best illustrated in the picture according to Huygens Principle. An incoming plane wave (beam) in the back focal plane can be decomposed into starting points of diverging spherical wave fronts. The objective transforms these secondary waves into plane waves which are differently tilted towards the optical axis but converge all to the same point, termed geometric focus. The angle of the wave vector towards the optical axis is determined by the paraxial distance h after Abbe's sine-condition. A sketch of this illustrative focus formation is shown in figure 2.6(a). Hence, when both objectives are illuminated equally, one can find for every secondary plane wave from object 1 a secondary plane wave coming from objective 2 which travels along the same path but in an opposite direction i.e. completely counter

propagating. Finally, a standing wave is formed along the common line of propagation. The starting points of a counter propagating waves pair in the bfp of each objective are point inverted with respect to the focal point when similar objective lenses are used (magnification 1):

$$\vec{r}_{Obj.2} = -\vec{r}_{Obj.1} \tag{2.41}$$

In conclusion, the coherent superposition of differently oriented pairs of counter-propagating secondary waves in the focal point is the reason why the $fwhm$-value of the intensity minimum is increased (see figure 2.4).

Generation of tilted illumination PSF

In contrast to a homogeneous illumination of the bfp of the objective lenses, one can illuminate the bfp with only a smaller angular segment, for example with a Gaussian beam which is additionally displaced along the x-axis by the distance $-h$ or h in objective 1 or 2, respectively. For this configuration only a smaller part of the spherical wave front cap is used for the coherent superposition of wave pairs in the focus (e.g. only wave pair 4 and 5). Consequently, the resulting illumination pattern PSF gets titled towards the optical axis.
The tilt of the illumination PSF (α) can be approximated by the angle of incidence of the beam centroid leading to: $\alpha \approx \arcsin\left(\frac{h}{fn}\right)$. This relation is equal for widefield PSF since only a single secondary plane wave pair interferes. Deviations occur when large beams are used which are cut off at the entrance pupil of the objective lens (5.76 mm diameter of a NA 1.44 oil objective lens). Consequently, beam segments which are closer to the optical axis are more pronounced in the effective PSF pattern. In figure 2.6(b) calculations of the illumination PSF (x-y and x-z) are given for destructive interference 4Pi-optics illuminations with varying beams offsets. The tilt angle α of the PSF is stated in the figure.
In summary, the resulting angle of the PSF is a combination of two factors. First, the shape of the effective illumination aperture used which is defined by the size of the input beam and limited by the entrance pupil of the objective lens. Secondly, the intensity profile of the input light field which defines the weighting of every individual secondary wave component. Further, the $fwhm$ is still minimized due to the complete counter propagation of the spherical wave front caps and only enlarged by the aperture correction due to focusing.

2.3.2 3D localization in MINFLUX with three differently tilted illumination PSF

With 4Pi-optics, a possible improvement for 3D MINFLUX localizations as compared to Gwosch *et al.* [24] could be accomplished by combining the lateral localization as

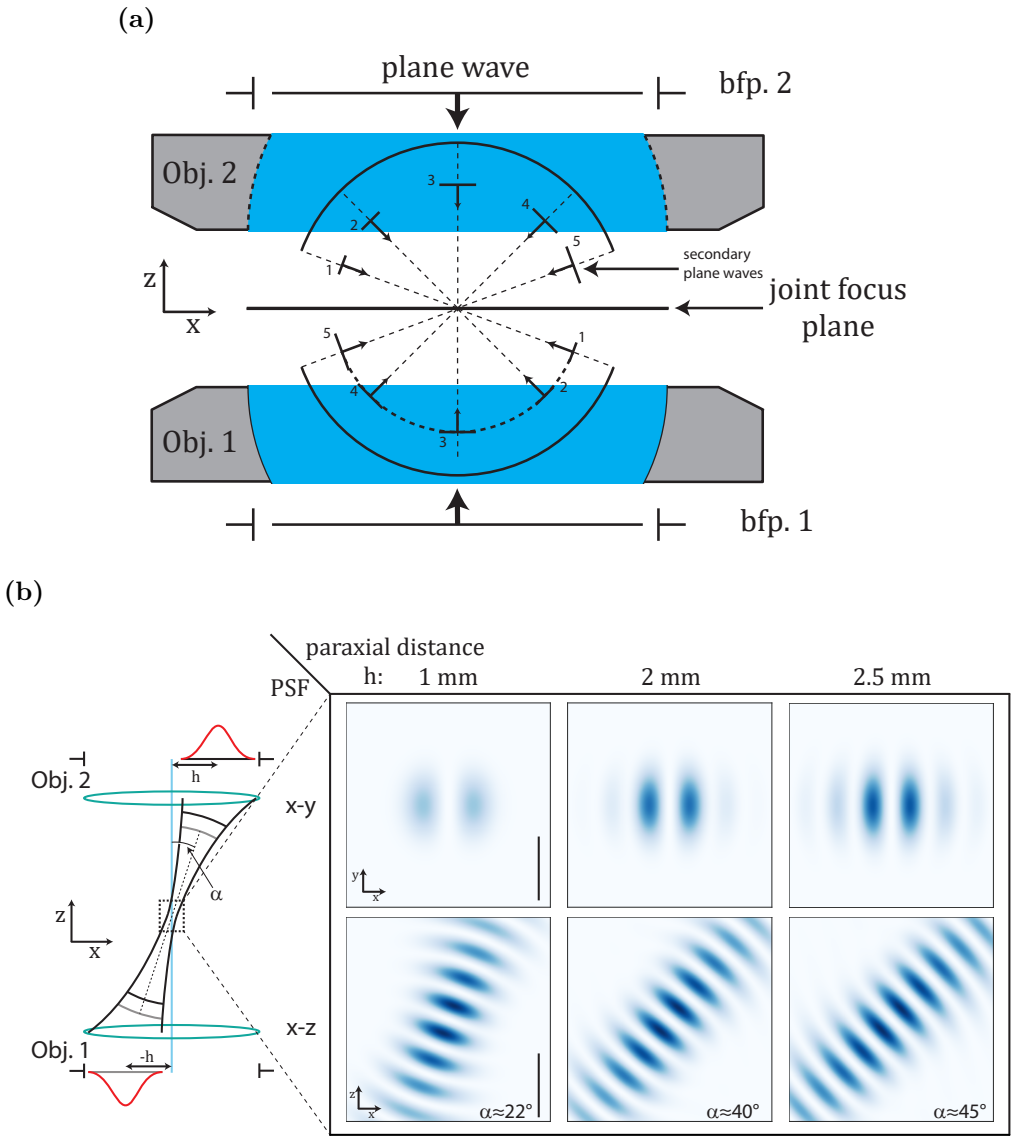

Figure 2.6: Tilted PSF in 4Pi-optics (a) Illustration of the focus formation in an double lens system, i.e. 4Pi-optics. The objective lens transforms the incoming plane wave into a spherical wave front cap which converge from different direction to the same point. According to Huygens Principle, the incoming wave can be decomposed into secondary waves which appear as plane waves in the focus area. For each secondary plane wave in objective 1 there is a secondary wave in objective 2, which propagates in the counter direction and both form a counter propagating beam pair (standing wave, dotted line). The total illumination pattern is described by the coherent sum (i.e. superposition) these standing waves weighted by their intensity. The different orientations leads to an effective increase in the $fwhm$ and intensity filling of the lateral plane (compare figure 2.4).
(b) Calculation of tilted PSF. A Gaussian input beam is illuminated with a paraxial distance along the x-direction of $-h$ and h in objective 1 and 2, respectively. Due to the offset the PSF appears tilted towards the optical axis by an h dependent angle α. The focal point remains unchanged (approximated angels are given). Referring to (a), the PSF is created by only selecting the secondary wave pairs from specific angular segment (e.g. 4 or 5). Calculations were performed for a NA 1.44 oil objective lens (λ =640 nm) and with $fwhm_{beam}$ = 1.5 mm. Scale bar: 500 nm.

preformed from Balzarotti *et al.* [22] with an axial localization using two interfering beams illuminated along the optical axis in 4Pi-optics. This can be seen as an analogy to isoSTED [38]. However, another conceivable approach would be to decompose the three dimensional localization into three sequential 1D localizations. For this case, 4Pi-optics allows to locate the emitter with three differently tilted PSF, which ideally form a normal coordinate system, i.e. are perpendicular to each other. The targeted translation of the minimum position in the single MINFLUX exposures could be accomplished by controlling the relative phase difference of the interfering beams. Thereby, all three localizations would rely on the same position estimation algorithm, which reduces complexity of the experiment.
In order to create three differently tilted PSF of counter propagating beams, the bfp of each objective is illuminated with three beams at different positions (figure 2.7(a)). Therefore, the entrance pupil is subdivided into three congruent circular segments with a circular arc of 120 °. The three beams are positioned in the center of the individual segments $\vec{r}_{bfp,i}$ with $i = \{1, 2, 3\}$ and are characterized by their distance to the optical axis h and their beam size $fwhm_{beam}$. In the coordinate system of the bfp the respective beam centers are:

$$\vec{r}_{x',obj.1} = (-h\cos(30\,^\circ),\ -h\sin(30\,^\circ))^\intercal \tag{2.42}$$

$$\vec{r}_{y',obj.1} = (h\cos(30\,^\circ),\ -h\sin(30\,^\circ))^\intercal \tag{2.43}$$

$$\vec{r}_{z',obj.1} = (0,\ h)^\intercal \tag{2.44}$$

The transformation of the beam position in objective 1 to objective 2 is performed by inverting all the coordinates (see equation 2.41). The electric field vector ($\vec{E}$) of the converging wave front cap, which is described in the coordinate system of the focus (x,y,z), is transformed by:

$$\vec{E}_2(\vec{r}) = M\vec{E}_1(M\vec{r}) \tag{2.45}$$

With the transformation matrix M

$$M = \begin{pmatrix} -1 & 0 & 0 \\ 0 & -1 & 0 \\ 0 & 0 & -1 \end{pmatrix} \tag{2.46}$$

With each localization using a tilted PSF, the emitter position is confined along the normal plane of the beam propagation axis, i.e. tilted PSF axis. Performing first a localization along x', confines the emitter positions to a plane normal to the x'-axis. With the second localizations along the y'-direction, the emitter is confined to the cut line of the two respective planes of possible positions. A third localization along

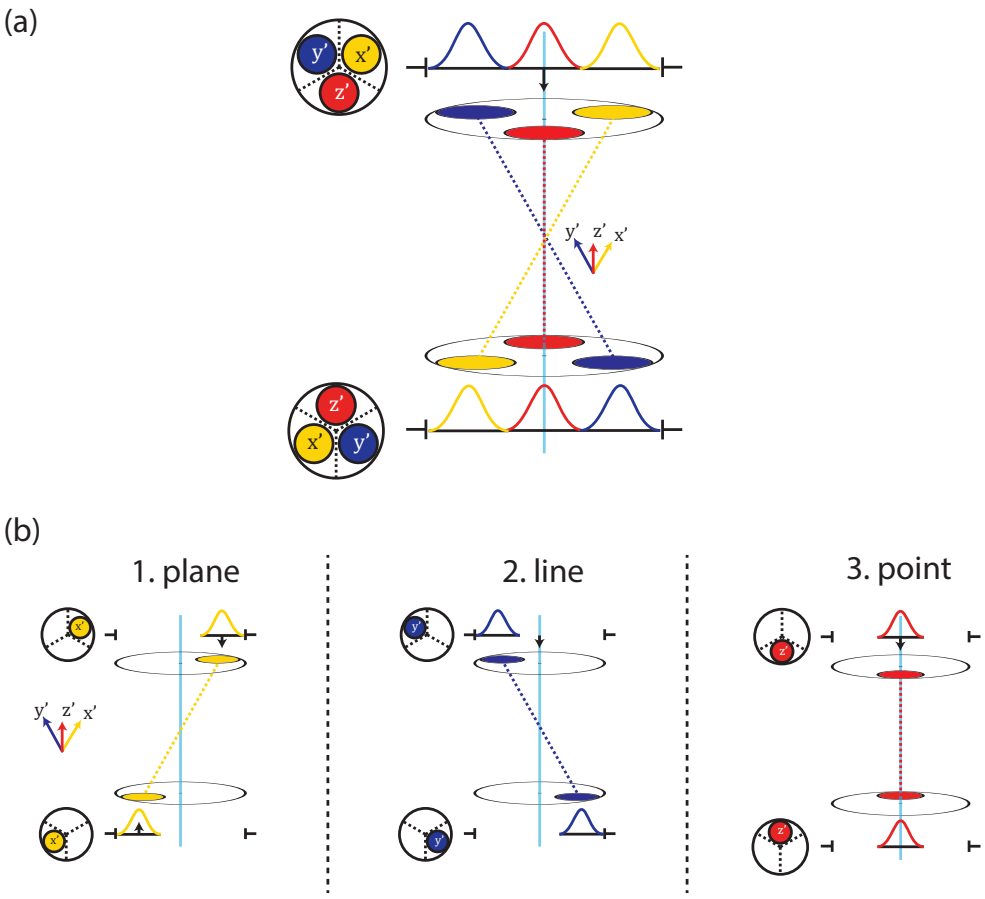

Figure 2.7: 3D localization of an emitter using 4Pi-optics (a) Three one-dimensional localizations are performed with differently tilted PSF. The localization is performed along a coordinate system (x', y', z') which is rotated to the coordinate system of the microscope. (b) The 3D localization is decomposed into sequential one-dimensional localizations along the respective propagation line of the PSF. The position of the emitter is confined to a first plane, second a line and finally a single point.

z' would define the allowed emitter positions down to a single point. The point is the intersection of the third localization plane and the previously derived line of possible localizations (figure 2.7(b)).

Ideally, the tilted PSF can form a normal coordinate system, i.e. the centerline of the tilted PSF are perpendicular to each other. Considering widefield illumination, i.e. focused beams in the bfp, this can be achieved with a paraxial distance of 2.45 mm for all three beams (derived in appendix A.3). In order to get a focused PSF, which we favor in the MINFLUX application, the beam size must be increased. However, this would lead to a cut off of the beam profile at the edge of the entrance pupil due to the limited pupil radius of 2.88 mm for a 100x 1.44 oil objective lens. Consequently, beam segments closer to the optical axis, which cause a smaller angle of incidence, are stronger weighted in the superimposed PSF pattern. Thus, the effective tilt of the PSF is reduced with increasing beam size. In conclusion, a compromise between tilt of the PSF and focusing strength must be found by tuning the parameters of the

amount of illuminated pupil area and the intensity structure (beam profile) in the illuminated area.
In simulations, the beam position in the pupil and the $fwhm$ of the beam was varied to find ideal conditions, which enable an as high as possible tilt of the PSF to the optical axis and focusing strength. It was found out that a beam positioned at the edge of the entrance pupil (h =2.8 mm) and a beam size ($fwhm_{beam}$) of 2 to 2.5 mm satisfies the conditions well enough. The resulting angle of incidence is approximately 40 ° and the focusing properties leads to a confocal $fwhm$ of 118 nm. These settings can be used as starting conditions in the experimental realization of 3D 4Pi-MINFLUX.

2.3.3 Requirements for the 4Pi-MINFLUX setup

In a conventional 4Pi microscope, the illumination beam is divided by a beam splitter in two beam parts that are guided to the respective objective lens and are united in the common focus of the objective lenses (4Pi cavity). In order to minimize the complexity of the setup only a single mirror was used between beam splitter and objective lens, which leads to a triangular shape of the beam path [41, 42]. Hence, the beams are passed to equal positions in the back focal plane (bfp) of the respective objective lenses, i.e. their position is symmetric to the focal plane. Since 4Pi microscopes were used with beams traveling along the optical axis, this property has not caused any limitations. It was even advantageous since it allows for using the microscope as a scanning setup with the scan mirror outside of the 4Pi cavity (scannable 4Pi-optics).
The triangular illumination, however, does not allow the generation of tilted PSF with a single displaced beam that enters the 4Pi cavity. Here, a beam displaced to the optical axis could not generate a counter propagating beam pair. To circumvent this limitation an additional reflection has to be inserted in one of the beam paths for each lateral dimension. In figure 2.8 the reflection with respect to the x-dimension is shown. For beam inversion in all three dimensions, as stated with the transformation matrix M (equation 2.46), an additional reflection has to be inserted in the y dimension (vertical to plane of the sketch). This additional requirement was considered in the experimental setup of the 4Pi-MINFLUX microscope (see section 3.1).
The detection beam path of a MINFLUX microscope does not require a specific symmetry or configuration. However, a coherent detection of the fluorescence light, as realized in type-C 4Pi microscope could double the detection efficiency [33].

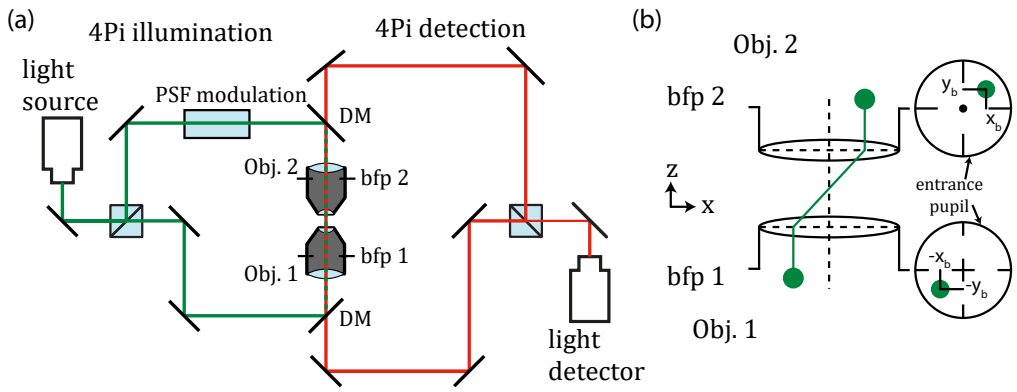

Figure 2.8: Sketch of a beam-inverting rectangular 4Pi setup as it was used in 4Pi-MINFLUX.(a) The 4Pi illumination cavity starts at the beam splitter that guides the incoming beam of a coherent light source into two paths, and ends at the common focus of the two objective lenses. The uneven number of reflections (number of mirrors) after the beam splitter leads to an inverted illumination scheme. The fluorescence light is guided under equal symmetry conditions of the beam path towards the light detector. For the sake of clarity, the beam inversion for the dimension pointing outside of the plane of the sketch was not shown. (b) In a beam-inverting setup (as shown in (a)) a beam that is displaced to the optical axis, is guided to inverted positions in the respective back focal plane (bfp). This leads to counter propagating beams in the focal plane. Note that for inversion along both dimensions the dimension pointing outside of the plane of the sketch must be also inverted. This can be fulfilled by a similar configurations of mirror as in (a).

3 Experimental materials and methods

This chapter covers the experimental microscope design, the developed MINFLUX localization routine and the sample preparation. The design of the 4Pi-MINFLUX microscope was based on the concept of a type-A 4Pi microscope with linear coherent excitation and incoherent detection, with the aim to achieve single nanometer localization precision with the fewest number of photons possible. The core unit is the interferometric illumination cavity, which uses electro-optical crystals for microsecond fast and subnanometer precise control of the two optical path lengths that span the cavity. This chapter starts with the optical and mechanical setup (section 3.1 and 3.2, respectively). The localization routine, data processing and its software implementation were developed by other members in the group and were adapted to the 4Pi-MINFLUX experiment (section 3.3 and 3.4). The protocols for the 4Pi microscope sample preparation are mentioned in section 3.5.

Comment on the design of the 4Pi cavity Based on the following reasons, the designed 4Pi cavity deviated from the triangular shape, which is the most compact one and was typically implemented in 4Pi microscopes [42–44]: (1) The phase modulation as well as multiple optical elements, e.g. wave plates, were installed inside the cavity. (2) The required beam inversion, which was motivated in section 2.3.3. (3) An increased rigidity of the objective positioning system with nanometer precision. All these boundary conditions required more space inside the cavity, and consequently a more bulky rectangular arrangement of the components was designed. In addition, the larger design simplified the diagnostic of the beam quality and allowed a more versatile use of the microscope. However, it made the illumination 4Pi cavity, with a cavity path length larger than one meter, more susceptible to thermal drift.

3.1 Optical setup

The main optical layout can be divided in multiple areas (figure 3.1): laser-unit, beam shaping unit, 4Pi cavity with illumination and detection unit.
A general description of each single microscope unit follows including a more detailed presentation of the 4Pi cavity. The microscope has been constructed with the intention to use four standard illumination wavelengths (405, 488, 560 and 640 nm), however not all of these wavelengths have been used within this thesis.

Laser unit The laser unit was built on a separated optical table. The fluorescence excitation laser light stemmed from different single frequency lasers with wavelength of 640 nm (Laser 1) and 560 nm (Laser 2), respectively. A dichroic mirror (DM1) combined both excitation laser beams onto the same optical path and the subsequent acousto-optic tunable filter (AOTF) adjusted the intensity of the respective transmitted laser light. The illumination light was coupled into a polarization-maintaining single-mode fiber (PM-SMF 1) using an apochromatic fiber coupler (FC1). A half-wave plate ($\lambda/2$) rectified the polarization of the beam to the preferred transmission direction of the fiber. For diagnostics of returning illumination light, a T90/R10 beam splitter (BS1) was installed before the fiber coupler. The reflected back traveling light was detected with a photo diode (PD).

Beam shaping unit After its collimation with FC2, the illumination beam was passed through a half-wave plate ($\lambda/2$) to set the polarization along the vertical direction, which is normal to the optical table. Then, the beam is guided to a laser line filter (LLF) for spectral filtering of residual luminescence photons generated in the optical fiber and a polarizer (Pol) for polarization clean-up. The subsequent motorized half-wave plate tilted the polarization to roughly 45 °, which defined the power levels of the two cavity beams. For adjustment and diagnostic purposes, the beam traveled through a pair of two glass plates, which reflected a small amount of light at its interface (forward and back traveling light). The installation of two contrary angled glass plates minimized the introduced lateral chromatic shift. We split back traveled light intensity according to its round trip direction (i.e. reflection or transmission at the illumination cavity beam splitter) with a polarizing beam splitter (PBS) and measured the light intensity at each output port of the beam splitter with a photo diode (PD2 and PD3). Before entering the 4Pi cavity, a telescope allowed adjusting the size of the excitation beam to a full width at half maximum value of 2.5 mm in the back focal plane (bfp) of the objective. For alignment purposes, we placed a pinhole with a diameter of 30 µm in the common focus of both lenses.

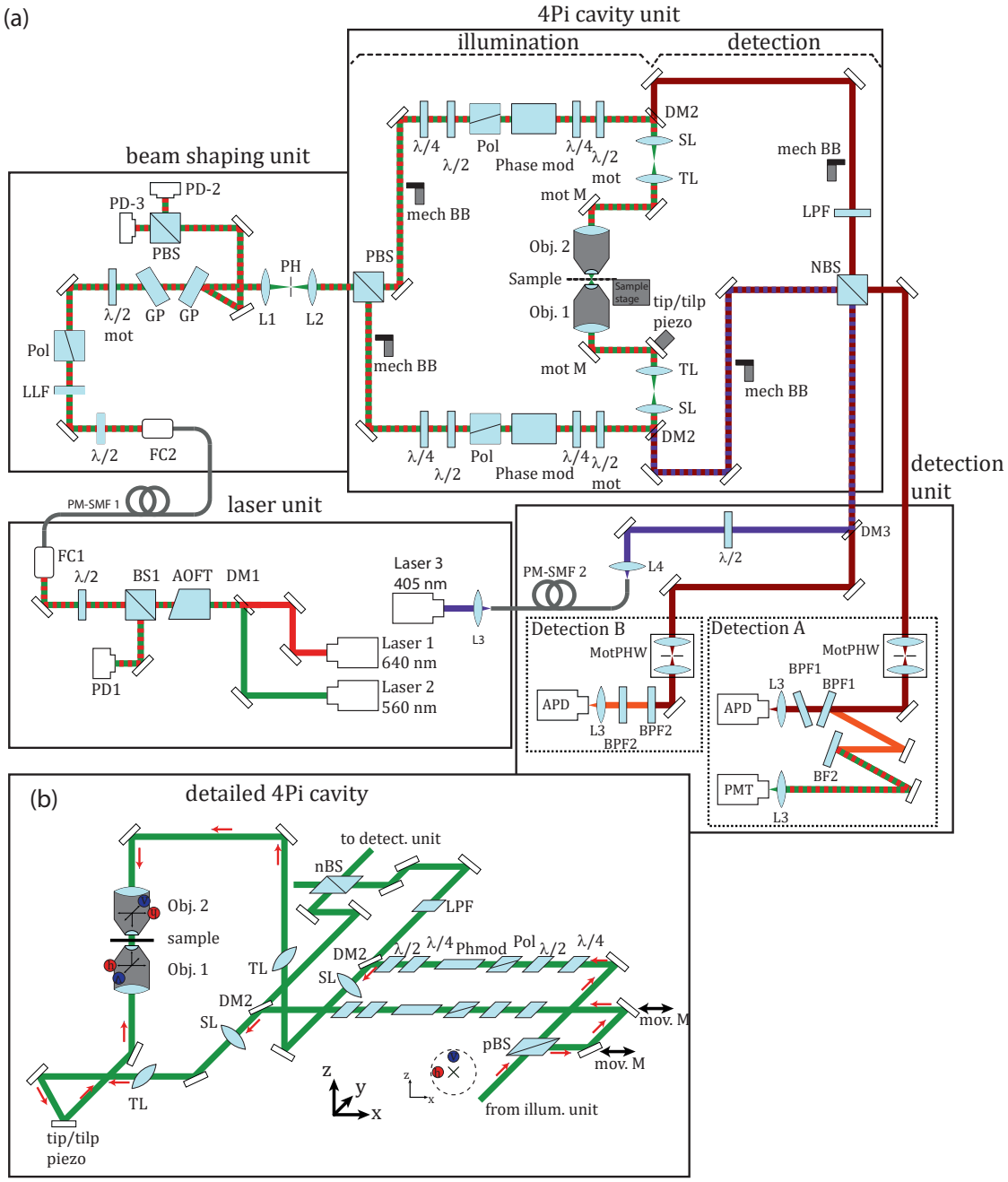

Figure 3.1: Optical beam path of the 4Pi-MINFLUX microscope for 1D axial localization. (a) Laser and beam shaping unit were used to establish the desired illumination beam properties before the beam entered the 4Pi cavity unit. At the beamsplitter (PBS) the beam is split into two different paths which are guided to one objective lens each. The interferometric recombination of the beams at the joint focus of both objective lenses creates a 4Pi illumination PSF (see figure 2.5). Fluorescence light emitting from this point is confocal detected in the detection unit. (b) Arrangement of all optical components in the 4Pi cavity. In order to highlight the beam inversion with respect to the focus point, the illumination pattern of a horizontal (red h) and vertical (blue v) displaced beam entering the beam splitter, is mapped into the bfp of the two objective lenses. The position of the horizontally displaced beam is highlighted with an red arrow. All components of this figure are listed in table 3.1.

4Pi cavity unit - illumination Depending on the polarization of the beam, the PBS split the illumination light into two different paths, which form the illumination cavity. Both beam paths, i.e. cavity arms, are recombined at the common focus of both objective lenses.[1] In order to compensate and minimize relative optical path length changes of the 4Pi cavity arms, we used similar optical components and placed them at roughly similar positions along the beam path. Note that we could not maintain complete symmetry of the beam path since the beam inversion was established by additional mirror reflections in one cavity arm (see figure 3.1 (b)).
We used a combination of half- and quarter-wave plate ($\lambda/2$ and $\lambda/4$) to rectify the polarization in each cavity arm which should be parallel to the direction of the applied electric field at the subsequent electro-optical phase modulator (Phase mod). Another combination of motorized $\lambda/2$ and $\lambda/4$ wave plates allowed arbitrary control of the beam polarization in the bfp of the objectives.
Afterwards, a dichroic beam splitter (DM2) reflected the illumination beam and guided it through the scan lens (SL) and the tube lens (TL) towards the objective (Obj. 1 and Obj. 2, respectively). We placed the tube lens on a five-axis stage to adjust its position in the beam path. The sample was mounted on a six-axis sample scanner (sample stage) which allows translational as well as rotational movement of the sample.
For lateral confocal scanning of the beam in the lower cavity arm, we mounted the mirror after the tube lens on a tip/tilt piezo scanner (tip/tilt piezo) and controlled it with a homemade electronic driver. For the adjustment of the relative optical path length of both cavity arms, we moved a closely placed pair of mirrors in a retro-reflection configuration along the beam direction which resulted in a minimal beam deviation upon translation (mov. M in figure 3.1(b)).

4Pi cavity unit - detection Each objective lens collected fluorescence light from the sample and illumination light, which was reflected at the coverslip interface or illuminated from the opposing objective lens. By splitting the fluorescence light from the illumination light inside the 4Pi unit at DM2, we created a detection cavity (incoherent) until the merge of both beams at the neutral beam splitter (NBS, T50/R50).[2] Due to the chosen mirror arrangement of the detection cavity, the respective field of view of each objective was point inverted at the optical axis when compared to each other after the beam splitter.
We installed electronically controlled mechanical beam blocks (mech BB) in each

[1] A horizontal (vertical) polarized input beam was transmitted (reflected) at the beam splitter and consequently, traveled clockwise (counter clockwise) inside the cavity (see figure 3.1).

[2] Even when the use of a beamsplitter was not necessary we tried to combined both beams, i.e. split the detection beam path into two paths, to allow for future application with different detection schemes, e.g. camera detection or coincidence measurements.

illumination and detection cavity arm to enable a diverse use of different illumination and detection schemes e.g. for alignment purpose or confocal measurements using only the lower beam path.

Detection unit We guided each output port of the NBS into a confocal detection subunit (Detection A and B) In each subunit, we installed a motorized pinhole wheel (mot PHW) and a pair of equal band pass filters (BPF1 (698/70 nm) or BPF2 (600/50 nm)) to ensure complete illumination light blocking. For fluorescence detection, we used an avalanche photodiode (APD) in combination with a focusing lens L3. Interchanging of the band pass filters with BPF1 in Detection B increased the detection efficiency (used in experiments of section 5 only).[3] The pinhole diameter of the mot PHW was 100 µm and 90 µm for 640 and 560 nm excitation which corresponded to a diameter of 384 and 346 nm in the sample plane.[4] The laser light was suppressed by 99 % at the intra-cavity dichroic mirror DM2, which, however, was not enough for complete blocking of the illumination light. Hence, the measurement of illumination light in the detection unit was used for alignment purposes. Therefore, we installed a photon multiplier tube (PMT) in detection A. The illumination light was mirrored from two band pass filters (BPF1 and BPF2) and focused by a lens (L3) onto the PMT.
Due to lack of space in the beam-shaping unit, we coupled the ultraviolet (UV) activation laser (Laser 3, 405 nm) which was used in MINFLUX imaging experiments, from the detection side into the beam path of the lower objective. We guided the activation light from the laser unit table with a single-mode polarization-maintaining fiber towards the microscope. A dichroic mirror (DM3, 405 nm) aligned the activation laser light onto the illumination and detection beam path but with different traveling direction. In order to photo-activate only with the lower objective lens, we placed a long pass filter (LPF, 473 nm) in the upper detection beam path.

[3] When both detectors were sensitive to red fluorescence light we have measured up to 10 % similar fluorescence intensities between them.

[4] Due to the physical arrangement on the optical table it was not possible to place the motorized pinholes for Detection A and B at equal distances to the NBS. Hence, based on the small beam sizes used the path length difference caused different magnifications of the beam at the mot PHW.

Lasers

Laser 1	Cobolt Bolero™, 640 nm, 500 mW	Cobolt AB, Solna, Sweden
Laser 2	Cobolt Jive™, 561 nm, 500 mW	Cobolt AB, Solna, Sweden
Laser 3	PhoxX+®,405 nm, 120 mW	Omicron-Laserage Laserprodukte GmbH, Rodgau-Dudenhofen, Germany

Beam modulation

AOTF	PCAOM VI	Crystal Technology Inc, Palo Alto, CA, USA
Phasemod	RTP-crystal, 2.3x2.3x60 mm^3	Raicol CRYSTALS Ltd, Rosh Ha'Ayin, Israel

Scanner mechanical mounts

Tip/tilt piezo	S316	Physik Instrumente GmbH & Co. KG, Karlsruhe, Germany
sample stage	Smarpod 110.45.2-d-sc-149	SmarAct GmbH, Oldenburg, Germany
mot M	STT-25.4	SmarAct GmbH, Oldenburg, Germany
mech BB	mechanical beam block	electronics workshop MPIBPC, Göttingen, Germany
mot. $\lambda/4$ or $\lambda/2$	motorized rotation mount	Thorlabs Inc., Newton, NY, USA

Polarisation and plan optic

$\lambda/2$	achromatic half wave plate (500-900nm or 460-680nm)	B. Halle Nachfl. GmbH, Berlin, Germany
$\lambda/4$	achromatic quarter wave plate (500-900nm or 460-680nm)	B. Halle Nachfl. GmbH, Berlin, Germany
Pol.	Glan-Laser calcite polarizer	Thorlabs Inc., Newton, NY, USA
PBS	polarizing beam splitter cube	Thorlabs Inc., Newton, NY, USA
NBS	T50/R50 beam splitter cube	Thorlabs Inc., Newton, NY, USA
BS1	T90/R10 beam splitter cube	Thorlabs Inc., Newton, NY, USA

Focussing optic and pinholes		
Obj1 and Obj. 2	HC PL APO 100x/1.44 Oil Corr CS	Leica Microsystems GmbH, Wetzlar, Germany
TL	tube lens f200	Leica Microsystems GmbH, Wetzlar, Germany
L1-L4	achromatic lenses with broadband anti reflection coating in the visible range	Qioptiq Photonics GmbH & Co KG, Göttingen, Germany
PH	pinhole (diameter: 30 µm)	Qioptiq Photonics GmbH & Co KG, Göttingen, Germany
Mot PHW	motorized pinhole wheel (MPH16)	Thorlabs Inc., Newton, NY, USA
Dichroic mirrors and filters		
DM1	Di03-R561-t3-25x36	Semrock Inc., Rochester, NY, USA
DM2	zt405/488/561/640rpc	Semrock Inc., Rochester, NY, USA
DM3	Di03-R405-t3-25x36	Semrock Inc., Rochester, NY, USA
LLF	640/8 (LD01-640/8-12.5) or 561/4 (FF01-561/4-25)	Semrock Inc., Rochester, NY, USA
BPF1	FF01-698/70-25	Semrock Inc., Rochester, NY, USA
BPF2	ET600/50m	Chroma Technology Corp, Bellows Falls, VT, USA
LPF	BLP01-473R-25	Semrock Inc., Rochester, NY, USA
Fibers and collimator		
PM-SMF 1	P3-630PM-FC-10	Thorlabs Inc., Newton, NY, USA
PM-SMF 2	P3-405BPM-FC-10	Thorlabs Inc., Newton, NY, USA
FC1	60FC-4-RGBV11-47	Schäfter + Kirchhoff, Hamburg, Germany
Detectors		
APD	SPCM-AQRH-13-FC	Excelitas Technologies, Waltham, MA, USA
PMT	H9305-03	Hamamatsu Photonics K.K., Hamamatsu City, Japan
PD	PDA10CS2	Thorlabs Inc., Newton, NY, USA
Objective positioning		
x, y & z motor	Piezo LEGS® Linear Twin-C 450N	PiezoMotor Uppsala AB, Uppsala, Sweden

Sensing head	T1031-15A	Renishaw GmbH, Pliezhausen, Germany
encoder	TI20KDA01A	Renishaw GmbH, Pliezhausen, Germany
linear scale	A-9715-0002	Renishaw GmbH, Pliezhausen, Germany
motor controller	BMC 101	NANOS-Instruments GmbH, Hamburg, Germany
acoustic foam plates	Pur Skin	SONATECH GmbH + Co. KG, Ungerhausen, Germany
alluminum scaffold	30 mm profile system	MayTec Aluminium Systemtechnik GmbH, Olching, Germany

Table 3.1: Abbreviation, model number and manufacturer of the hardware components installed in the 4Pi microscope e.g. as labeled in figure 3.1.

3.2 Mechanical construction of the 4Pi unit

We constructed the objective mounting frame with the purpose of lateral and axial translation of the objectives with respect to each other but without a rotational degree of freedom.[5] In order to facilitate the sample mounting, we chose an upright i.e. vertical objective lens arrangement (see figure 3.2 (a) or A.6). The first mirror behind the objective lenses was mounted in a motorized tip-tilt mirror mount (mot M).

The translational positioning of the objectives was decoupled into a lateral movement of the lower objective laterally (x and y) and an axial movement of the the upper objective (z). For a very rigid and precise positioning system, we pinpointed three main requirements:

Translation range: lateral: $\sim 1\,\mathrm{mm}$ for the compensation of manufacture inaccuracies of the mounting frame. Axial: $\sim 2\,\mathrm{mm}$ for lifting the objective high enough to facilitate the installation of the sample.

Rigidity: As high as possible to prevent susceptibility to external noise vibrations and as low as needed for the positioning device to achieve the aimed translation range.

Positioning accuracy and jitter: As low as possible and preferable in the range of the aimed MINFLUX localization precision (1 nm). The electrical noise of the position encoder (jitter) as well as the accuracy of the positioning system have to be

[5]The control of the rotational degrees of freedom would be necessary if it is required to correct residual tilts between the focal planes of the two objectives (see for example [43]). This was not required in our case, since we exclusively measured in the joint diffraction limited pattern of both objectives. However, it was required that the pattern overlap and that they are collinear to each other and the optical axis.

considered.
All positioning systems relied on the principle of a flexure bearing, i.e. bending of a flat spring. The deformation of the device upon a driving force enabled a parallel conduction along the desired direction with nearly no mechanical stick slip effects (excluding the driving force for the positioning device). Furthermore, the rigidity of the positioning system could be adjusted by the thickness of the part that bended upon force effect.
We performed lateral positioning with two similar flexure bearings but rotated by 90 ° in a stacked arrangement. The technical realization of the axial positioning differed to the lateral one, because the objective had to be moved parallel to the optical axis (see figure 3.2 (b)). Technical details of the force dependent deformation and mechanical stress of the positioning elements are shown in figure A.4 and A.5.
As driving force of the positioning system we chose a push/pull piezo motor,[6] which were operated in a closed loop circuit. The installed piezo motors (x, y & z motor) had a translation range of 20 mm, a load dependent push/pull force of 450 N and a smallest step length of 0.2 nm. The movement was monitored with an optical encoder system, which achieved a 1 nm precise incremental position measurement (constituted of linear scale, sensing head and encoder). We performed closed loop operation of the motor using an additional motor controller, which sent position commands to the motor and received the encoder signal as well as user defined new position commands from the host PC.
A CAD-illustration of the installed objective mounting frame is given in figure 3.2 (c). Beside the piezo motors and their connectors to the respective objective mount it included pillars of aluminum and brass. These pillars compensate the different thermal expansion coefficients of the objectives (brass-like) and the aluminum mounting frame [45]. In order to lower the influence of thermal fluctuations, the objective mounting frame was covered with aluminum plates on each side. The arrangement with additional optical components, like mirrors and beam splitter, is shown in figure 3.2(d).
To minimize noise contributions, e.g. microphony, fluctuation of the air and temperature drifts, all segments were caged twice in an aluminum scaffold and surrounded with aluminum plates and acoustic foam plates.

[6] These piezo motors reached the desired stroke in a sequence of many sub nanometer large sized steps. These steps were performed by the bending of multiple single piezo elements attached to two opposing sides of the rod that is pushed or pulled. Thus, their stated load dependent push/pull force could be guaranteed over the whole stroke range.

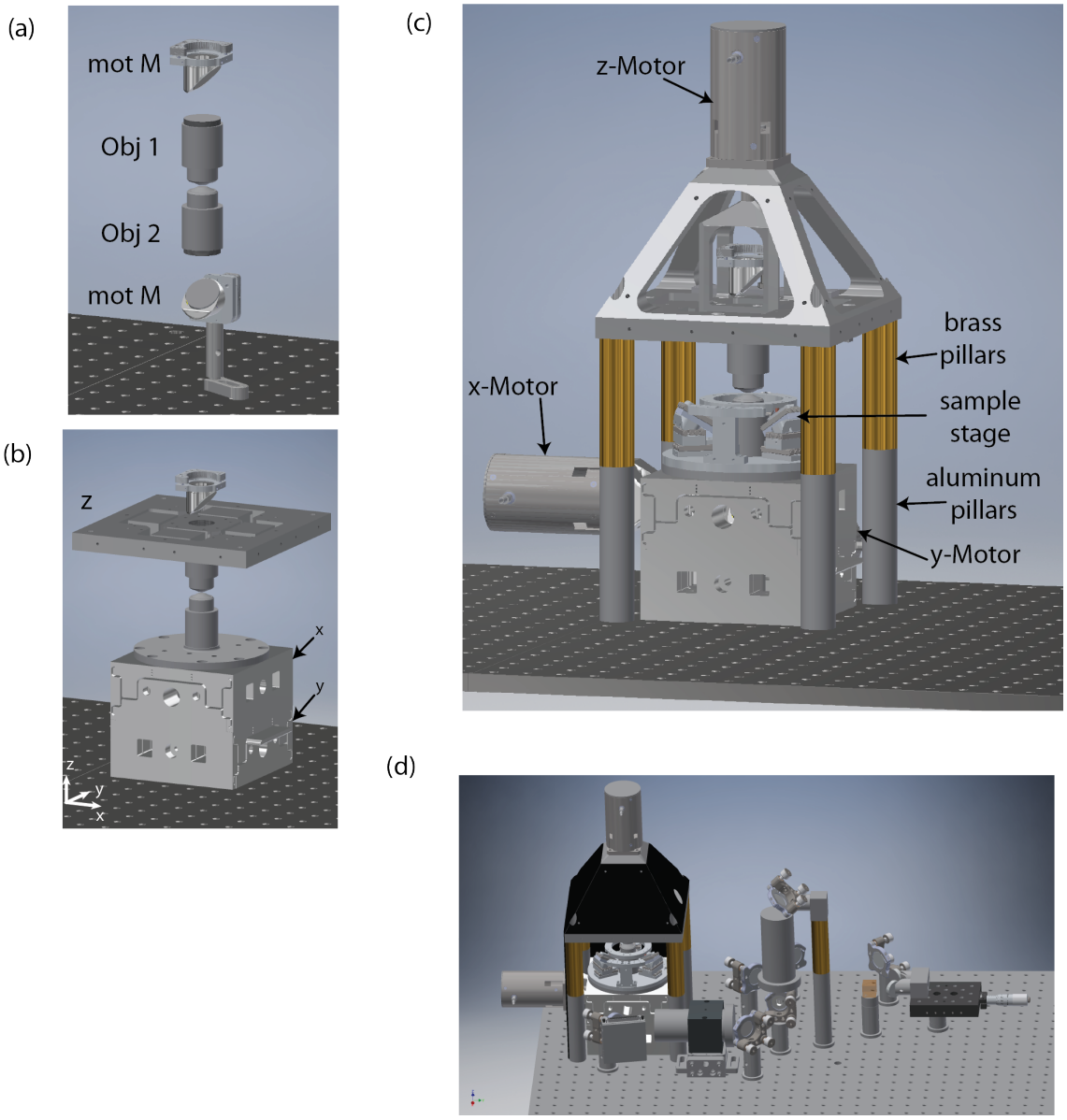

Figure 3.2: Mechanical construction of the objective mounting frame. (a) Vertical aligned opposing objective lenses and the respective first cavity mirror after the lens. (b) Objective lens positioning system translates the lower lens along the lateral (x and y) direction and the upper lens along the axial direction (z). (c) Total objective frame with the respective piezo motors and adapters to the positioning system. The upper objective frame was mounted on aluminum and brass pillars to equalize the thermal expansion. d) Complete 4Pi illumination cavity. For the sake of simplicity optical components e.g. wave plates were neglected.

3.3 Experiment control software

The individual devices of the microscope were controlled from a home-built LabView program (LabView 2019, National Instruments, Austin, TX, USA) running on a Windows 10 personal computer. Device communication, data acquisition, and online (live) calculations (evaluation) were performed by a field-programmable gate array (FPGA) based real-time system with a respond time of 1 µs (PCIe-7852, National Instruments, Austin, TX, USA).
The main task of the implemented FPGA structure was to create correct controlling and gating of illumination, scanning and detection devices. Additionally, the FPGA calculated the emitter position in each MINFLUX step and used this information, if required, for the parameter update in subsequent MINFLUX measurements. The relevant devices and the respond times for the communication with the FPGA board are shown in figure 3.3. We used the digital and analogue input-output communication based on a breakout box and two homebuilt FPGA connector cards to perform the following main communication tasks:

- **Laser controlling:** Laser power modulation and on-off-switching (analogue) modulation for diode lasers (Laser 3) and AOTF modulation for solid state lasers (Laser 1 and 2).
- **Scanning:** Controlling of the tip/tilt piezo position (electro-mechanical) and of the voltage at the phase modulator (electro-optical).
- **Detection:** Photon detection via PMT and ADP as well as auxiliary photo diodes.
- **Positioning:** Control of the position of sample, objective motors and mechanical shutters.

Communication to other peripheral devices (e.g. motorized pinhole and rotation mount) was done via USB. Information about the temporal performance were added at the relevant component in figure 3.3. It should be highlighted that the fast electro-optical scanning features response times lower than 1 µs, which is only limited by the electronics, i.e. high voltage amplifiers.

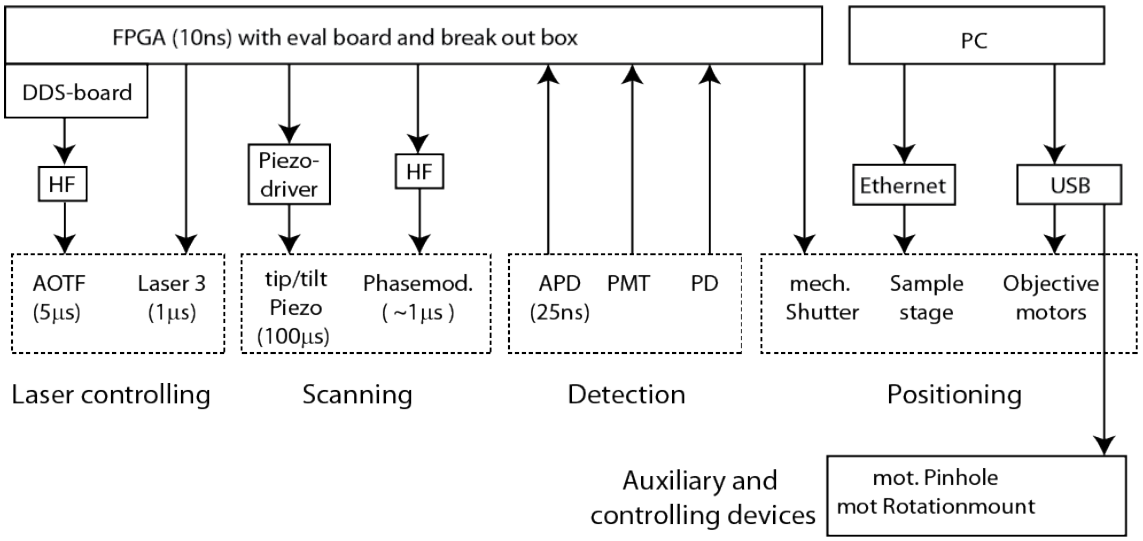

Figure 3.3: Schematic of the experiment control unit. A FPGA-based LabView program, which was operated on the host PC, was designed to synchronize the respective units: laser controlling, scanning, detection and positioning. The response times of individual devices are given to highlight the fast operating time of the microscope. The abbreviations of the devices are explained in table 3.1.

3.4 Scan routine

Since the MINFLUX localization was the last measurement step in a sequence of scans, we will present in the following the complete scan routine and give estimated number of detected photons, required in the pre-scans. The course of action for emitter localization required first a confocal centering of the emitter in the lateral plane and second an axial positioning to the point of reference for the MINFLUX localization onto the emitter. Thereby the axial field of view is defined symmetric around the reference point. From this point onward, MINFLUX measrements were performed either in localization or imaging mode. The values for the laser power and detected photons represent approximate values as they were measured in the experiments of section 4.3.

1. **Lateral confocal rough pre-localization:** Confocal x-y-scan (5x5 µm^2,1-2 µW)) with the tip-tilt piezo followed by identification and centering of a single emitter by sample stage positioning ($\sim$ 400 photons).
2. **Lateral confocal fine pre-localization** Confocal x-y-scan (500x500 nm, 1-2 µW) with the tip-tilt piezo followed by precise centroid fitting and subsequent centering to the emitter position by the sample stage ($\sim$ 1500 photons).
3. **Axial rough pre-localization:** Axial scan of the intensity minimum of the 4Pi PSF (100 nm, 1-2 µW with a subsequent correction of the minimum position (point of reference of the MINFLUX localization) to roughly match the emitter position by adjusting the voltage at the phase modulator ($\sim$ 500 photons).
   In case of MINFLUX imaging this scan was performed multiple times or

even with a higher power until a sufficient low fluorescence rate was detected indicating that all fluorophores were transferred into a long-lived dark state.

4. **Axial MINFLUX localization:** MINFLUX localization protocol as presented in section 3.4.2

In summary, the number of detected photons, which was spend for all scans before the MINFLUX localization, summed up to several 1000 photons. In order to prevent fluorescence excitation from the residual intensity pattern along the lateral plane, it was necessary that the prelocalization steps were performed with a sufficiently high number of photons and thus, achieve the required localization precision. (see x-y PSF of figure 2.5).

3.4.1 Iterative MINFLUX

A single MINFLUX measurement featured a fluorescent photon measurement with three illumination PSF, whose intensity minimum was translated along the axial localization direction to the positions $\{+L/2,\ 0,\ -L/2\}$ (figure 3.4(a)). Thus, each measurement contained the information of the photon counts at the respective position $\{n_1, n_2, n_3\}$.

The total measurement time (T_{tot}) was subdivided into three equally long exposure dwell times (T_{dwell}) which have individual preceeding setup times (T_{setup}), and a short position calculation time window ($T_{poscalc}$, see figure 3.4(b)). We performed the exposure dependent shift of the illumination PSF by updating the voltage at the top electrode of both phase modulators (U_{scan} in figure 3.4(c)). The initial reference position of the intensity minimum, which is defined by the voltage at the bottom electrode of both phase modulators (U_{pos}), as well as the laser intensity (U_{aotf}) were kept constant throughout the total measurement time.

The fluorescence detection window (T_{dwell}, colored surfaces in figure 3.4(b)) of each acquisition time window was gated after an individually chosen setup time (T_{setup}). The duration of the setup time ensured that firstly, the AOTF had activated the laser intensity, which needed to be considered only in the first exposure, and that secondly, the phase modulator has positioned the intensity minimum to the desired position.

In the last step, the detected photons counts were used to make a real time position calculation according to equation 2.10. If required, a position correction was performed by updating U_{pos}.

In the scope of this thesis, we implemented the iterative MINFLUX localization with three iterative steps. During these 'zoom in' steps, we corrected the reference position to the most probable emitter position, reduced the L-value and increased the laser intensity to gain similar photon fluxes in all iteration steps (adapted from

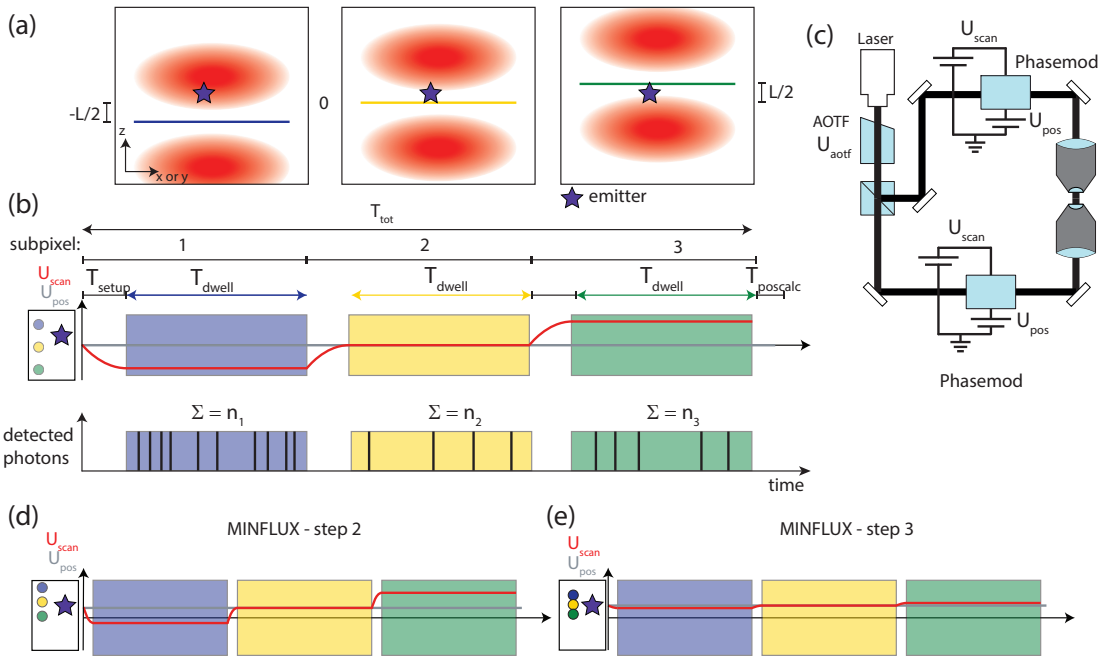

Figure 3.4: Sketch of the MINFLUX illumination and controlling scheme. (a) Illumination PSF was shifted along the z-direction (localization axis) towards three different positions: $\{-L/2,\ 0,\ L/2\}$. (b) Temporal process of a MINFLUX localization (upper graph: illumination and lower graph: detection). The total measurement time T_{tot} is subdivided in three exposures with individual setup and dwell times, and a position calculation time window. (c) Sketch of the devices used for the controlling of the 4Pi-MINFLUX scan algorithm. (d) and (e) Temporal process of the illumination controlling for iterative 'zoom in' steps with adjusting the point of reference (grey line) , L-value (red line) and laser intensity (denoted by transparency of the colored circles). Not highlighted are changes in dwell times since, they were experiment specific.

Gwosch *et al.* [24]). In figure 3.4 (d) and (e) the control of the measurement parameter in the 'zoom in' steps is illustrated. The dwell and setup times have been adapted with regard to the experiment question of interest in each iteration step. In case of MINFLUX imaging, we implemented a conditional activation of the photo-activation laser in the last iteration step. Therefore, we defined a certain photon count number as a threshold value to discriminate between measurements with and without activated molecules. If we measured in the second iteration step less counts as the threshold value we illuminated the activation laser instead of the laser for fluorescence excitation. Other measurement parameters were unchanged and the subsequent MINFLUX measurement were performed with the initially defined parameters.

3.4.2 MINFLUX localization modalities

In the scope of this thesis the 4Pi-MINFLUX microscope was used in three different modalities (adapted from Balzarotti *et al.* [22]):

MINFLUX tracing: Localization of a static emitter

The tracing algorithm was implemented with three iteration steps, from which the last iteration step was repeated with identical parameters multiple times (>100). Since the first two iteration steps should only guarantee that the point of reference for the last iteration step is centered to the emitter position, they were neglected in the analysis. The information about the emitter position was evaluated only from the repeats of the last iteration step. With tracing measurements we evaluated the drift of the minimum position and determined the localization uncertainty per number of detected photons (section 4.3).

MINFLUX tracking: Localization of a moving emitter

The tracking algorithm was implemented similar to MINFLUX tracing but additionally with a position correction at the end of each repeat of the last iteration step. This allows us to follow the movement of the emitter along the axial direction. We used MINFLUX tracking experiments to measure the artificial emitter movement created by the continuous displacement of the sample stage (see section 4.2).

MINFLUX imaging: Localization of multiple emitters

The imaging algorithm was implemented as a series of MINFLUX localizations of three iteration steps, e.g. more than 1000 repeats. Each localization was parameterized according to MINFLUX tracing and had identical starting parameters. The repeats of the last iteration step were defined by user-defined multiplexing factor, which typically ranged between 50 and 100. Using multiplexing, a measurement bias due to short term blinking of the emitter, which is shorter than the dwell time, could be more stronger suppressed. Here, the short off-state interval of the emitter does not fall within only one single exposure but is distributed among multiple different exposures (left, middle and right). For the position calculation of the last iteration step, the photon counts of all multiplexing steps are taken together in the respective exposure photon counts n_i. Since we achieved molecular on-/off-switching with statistically blinking fluorescence molecules, we implemented a conditional photo-activation using a UV laser in the last iteration step. This should support the statistical return of the molecule into an on-state (excitable for fluorescence emission) [21]. The laser was activated, if the total photon count of the second iteration came below a used defined threshold value. The position of the emitter is calculated from the cumulative sum of all position value per iteration step. MINFLUX imaging aimed for the localization of different close by fluorescent emitters (Alexa Fluor 647)

to demonstrate the resolution power of the 4Pi-MINFLUX microscope (see section 5).

3.5 Sample preparation

The 4Pi sample mounting differs from single objective lens microscopes in the aspect that two coverslips must be sealed together in a sandwich-like construction with the sample immobilized on the lower coverslip (figure 3.5(a)).
The 4Pi sample mounting creates an intrinsic asymmetry of the illumination scheme since the upper beam travels through the whole buffer medium before reaching the sample. Correcting actions to restore the optical symmetry could be taken by adjusting the refractive index of the buffer to the one of oil (n=1.518) and thereby minimizing the influence of e.g. spherical aberration [46]. In addition, the distance between both coverslips should be kept as low as possible and was commonly around 5 to 10 µm.

3.5.1 Coverslips and surface functionalization

For practical reasons, we chose two coverslips with different diameter (diameter: 15 and 18 mm, thickness: 170 µm, No 1.5H, Paul Marienfeld GmbH & Co. KG, Lauda-Königshofen, Germany) and mounted the sample on the larger one. To facilitate the alignment processes, the coverslip with the immobilized sample had an additional quarter-circular area aluminum coating serving as a mirror (adapted from [44]).

Cleaning of coverslips We sonicated the coverslips for 15 min each first in acetone (spectroscopy grade) and afterwards in milliQ water. We added only to the coverslips without the mirror 1 % (v/v) Hellmanex, since the soap removes the mirror coating. The coverslips were dried under nitrogen flow. Afterwards, we plasma cleaned (oxygen) the coverslips with 200 W power.

APTES surface functionalization For the silanization of the surface, the coverslips were placed directly after plasma cleaning into a 1 % (v/v) solution of APTES ((3-Aminopropyl)trieethoxysilane, Sigma-Aldrich, Steinheim, GER) in spectroscopy grade acetone. After 10 min of incubation, we placed the slide holder into a spectroscopy pure acetone, from which we took every coverslip individually and rinsed it on either side with milliQ water and dried under gentle nitrogen flow. To keep the silanized coverslips in a dry environment, we stored them in a sealed container box with beads of silica gel orange (Carl Roth Gmbh + Co. KG, Karlsruhe, GER).

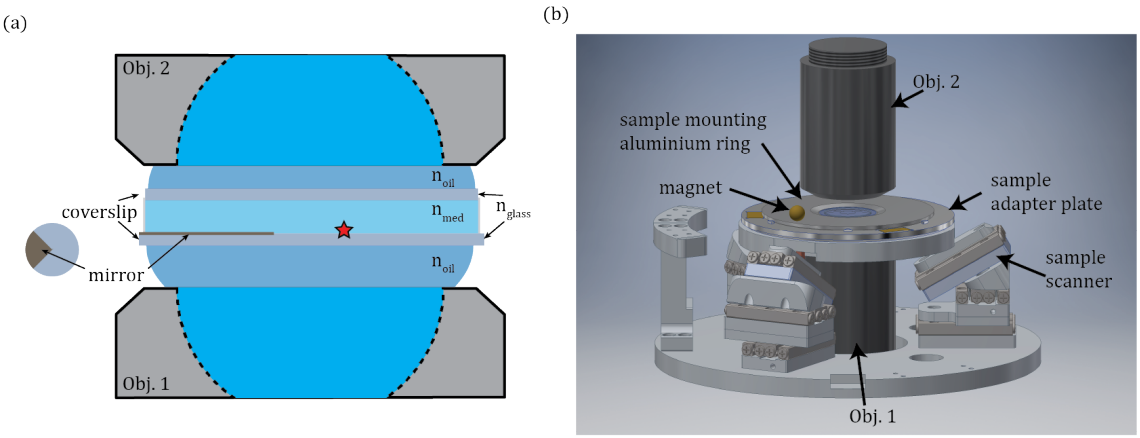

Figure 3.5: 4Pi sample mounting and installation in the sample stage. (a) Sketch of the 4Pi sample mounting. In order to guarantee illumination from both sides, we immobilized the sample (red star) on one coverslip and placed a second one on top with the mounting medium/ buffer in between. An alluiminum coating on the sample coverslip was just for alignment purposes. To guarantee best optical settings the refractive index of the medium n_{med} should be matched to the refractive index of the oil $n_{\text{oil}} = 1.518$.
(b) CAD-illustration of the sample installation on the sample stage. The aluminum ring, in which the both coverslips were fixed, was mounted onto the sample scanner using a homemade adapter plate. It was was kept in place by a magnet.

PLL-PEG-bt surface functionalization The coverslip surface was coated with PLL-PEG coated (PLL: Poly-L-Lysin and PEG: Polyethylene glycol) and functionlized with Biotin (bt). Therefore, we incubated 10 µl of PLL-PEG functionalized with Biotin (Bt) for 5 min on a cleaned coverslip. After washing with PBS, the PLL-PEG-bt functionalizd coverslip was stored with a drop of PBS in a wet chamber and were used at the same day. The protocol for was developed by Lukas Scheiderer and performed by Jessica Matthias both from our group.

3.5.2 Buffers

Refractive index matching was achieved with a commonly reported mounting medium for 4Pi samples: TDE (2,2'-thiodiethanol) [47]. TDE is a hygroscopic glycol derivative and its viscosity is more similar to the one of oil than of water. Mixing TDE with water (PBS) allowed a fine adjustment of the refractive index to any value of interest between 1.52 (TDE) and 1.33 (H2O). Due to this favorable property, we chose TDE as a component in all buffers used. In addition, we saw no increase in buffer induced background photon counts as compared to an aqueous buffer (PBS).

Buffer for MINFLUX tracking and tracing (TDE-buffer) We prepared a refractive index-matched TDE-buffer by adjusting the refractive index to 1.518 with the addition of PBS. The pH value was adjusted to 7.5-8 by adding HCl/NaOH [44].

Blinking Buffer for MINFLUX imaging In order to achieve suitable blinking properties of the studied dye (Alexa Fluor 647) and low beam aberrations, we prepared a mixture of a common STORM imaging buffer and the previously introduced TDE buffer [48]. We compared different mixing conditions and tried to achieve the highest possible amount of TDE while not degrading the rapid blinking properties.
We suspected that the more viscous TDE could have an impact on the mobility of the buffer ingredients; hence the stochastic blinking of the dye might not be guaranteed anymore. Thus, we stopped increasing the TDE concentration at a ratio of 65 % STORM-buffer and 35 % TDE. Here, the blinking properties could be demonstrated and the aberrations were sufficient low to achieve the required optical resolution. The STORM-buffer protocol was adapted from Balzarotti *et al.* [22] and the final imaging buffer was composed of: 50 mM Tris at pH 8, 10 mM NaCl, 10 mM $MgCl_2$, 10 % (w/v) glucose, 0.4 mg/ml pyranose oxidase (Sigma Aldrich P4234), 66 µg/ml catalase (Sigma Aldrich C100) and 100 mM cysteamine (Santa Cruz Biotechnology Inc., Dellas, Texas, USA).

Comment to background counts of different buffers In the study of different buffer media, low background photon counts in the medium relative to the coverslip are compared to refractive index matching an additional advantage for the suitability of the buffer. TDE-buffer and water based buffer resulted in a more than two-times lower background signal in the medium compared to the coverslip. We found that commercial available mounting media like the glycerol-based ProLong (ProLong glass Antifade Mountant, Thermo Fischer Scientific, Waltham, MA, USA) and Vectashield (Vectashield® Antifade mounting, Vector Laboratories Inc., Burlingame, CA, USA) showed equal or even higher background photon counts compared to the coverslip, respectively. Likewise, we found a 2.5-fold increased background signal for Mowiol, a common polyvinyl alcohol based buffer compounded after [49]. In conclusion, TDE-buffer or self-compounded water-based buffers are most suitable for our application.

3.5.3 Gold nanoparticles

Compared to single immobilized fluorophores, gold nanoparticle (GNP) exhibit a constant and non-bleachable photon emission rate, which made them ideal for the alignment of the 4Pi microscope. Since it was necessary to check the alignment for each sample, we immobilized GNP on the same coverslip as the sample of interest, but at a different location. We were able to distinguish GNPs from the sample of interest by the larger back-scattering signal of the GNP. Note that due to the refractive index matching the surface reflex at the coverslip interface is strongly suppressed.

We used GNP with a diameter of 40 nm and functionalized groups of NHS or Biotin for the immobilization on an ATPES or PLL-PEG-Bt surface, respectively (40 nm NHS-Activated Gold Nanoparticles and 40 nm Biotin Gold Nanoparticles, Cytodiagnostics Inc, Burlington, Canada). The GNP stock solution was diluted 1000-fold in the supplied buffer. The GNP solution was sonicated and centrifuged (3 min at 3000 rpm). For measurements with 560 nm (640 nm) illumination wavelength, we incubated 15 µl of the supernatant (pellet) in order to get predominantly monomers (oligomers). After 10 to 20 min of incubation time, we cleaned the coverslip with milliQ water, dried it under gentle nitrogen flow, and proceeded with the immobilization of the sample of interest.

3.5.4 Fluorophores

For proof of concept MINFLUX tracing and tracking experiments, we used Atto 647N (Atto 647N-NHS ester, Sigma-Aldrich, Steinheim, GER) for the red excitation wavelength or Cy3b (Cy3b-NHS Ester, Thermo Fisher Scientific, Waltham, USA) for the green excitation wavelength. Both dyes were bound to the surface with an NHS Ester. The dyes were stored in DMSO at -20 °C and we prepared a milliQ water diluted solution with 10 to 50 pM concentration at the day of preparation.
We incubated 10 µl of the dye solution on an APTES silanized coverslip for 5 min. Afterwards, we rinsed the coverslip with milliQ water and dried it under gentle nitrogen flow. For mounting the sample, we added 1.5 µl of TDE-buffer on the coverslip and placed the second one on top. By adjusting the volume of the mounting medium, we were able to tune the coverslip distance in the range of 5 to 10 µm.
Both coverslips were sealed and fixed in a homemade sample mounting aluminum ring using picodent twinsil® speed 22 (picodent® Dental-Produktions- und Vertriebs-GmbH, Wipperfürth, Germany). The sample could be stored for several days at 4 °C.

3.5.5 DNA origami nanopillars

The custom made DNA-Origami nanoruler (GATTAquant GmbH, Hiltpoltstein, GER) had the shape of a pillar with a quadratic base (nanopillar). The edge length of the quadratic pillar was 20 nm and the height was 40 nm. The base plate featured several Biotins, which enable the immobilization on a PLL-PEG-bt functionalized coverslip via streptavidin or neutravidin. Three labeling points of precise distance (10 and 20 nm) were labeled with one fluorophor (Alexa Fluor 647) each. In order to achieve stochastic blinking we used a blinking buffer.
Prior to incubation with the nanopillars, 20 µl of 1 $^{mg}/_{ml}$ neutravidin in PBS were

incubated for 5 min on a PLL-PEG-bt functionalized coverslip. We diluted the nanopillar delivered in solution in 1 x TAE 20 mM $MgCl_2$ (TAE: Tris-acetate-EDTA; EDTA: Ethylenediaminetetraacetic). The nanorules were exposed at a dilution of 1:10 to 1:20, as delivered for 5 min. After incubation, the solution was washed with TAE-Buffer containing 20 mM $MgCl_2$ and the remaining liquid was let drip. The sample was washed with the blinking buffer prior to mounting of the sample.
Due to the different hydrophilicity of the surface and different viscosity of the buffer, the volume of the buffer was not a good scale for the determination of the separation of both coverslips. Consequently, we placed an excess volume of imaging buffer (100 µl) on the sample and laid the second one on top of it. This sample-sandwich was mounted into a micrometer screw and squeeze together until a distance of roughly 360 µm was reached. While still mounted in the micrometer screw, we absorbed the excess liquid with a tissue and sealed both coverslips together with epoxy glue (UHU® Plus Sofortfest 2-K-Epoxidkleber, UHU GmbH & Co. KG, Bühl/Baden, Germany). The sealing into an aluminum sample holder ring was done with common nail polish. This protocol reliably reproduced the desired separation of the coverslips.

4 Axial 4Pi-MINFLUX localization of single fluorescent molecules

In the first two sections of this chapter we present the results of the verification of the 4Pi-MINFLUX microscope, which include the measured 4Pi PSF (section 4.1) and MINFLUX tracking measurements of an emitter moved along a user-defined trajectory (section 4.2). Further, the physical limitations of the 4Pi-MINFLUX localization precision with respect to the spatial and temporal dimension are discussed in section 4.3. The end of the chapter covers the results of MINFLUX measurements that were performed under optimal illumination conditions, to create a tight interference pattern and low residual intensity in the minimum (section 4.4).

4.1 Experimental 4Pi PSF

The illumination pattern used for axial 4Pi-MINFLUX localizations was measured with a single red-emitting fluorophore (Atto 647N) by sample stage scanning (figure 4.1). The axial PSF (x-z, figure 4.1(a)) shows the pattern of a focused standing wave along the axial direction. When the emitter is placed in the common focal plane of both objectives and the two beams interfere destructively, the intensity minimum coincides with the emitter position and the pattern features equally high side maxima. This pattern is used for the middle exposure in the MINFLUX localization scheme ($z_2 = 0$). When in the outer MINFLUX exposures the intensity minimum is translated by $\pm L/2$, the emitter experiences a higher intensity in the focallane plane (figure 4.1(b)). The lateral PSF (x-y, figure 4.1(c)) was measured in the central minimum of the symmetric PSF. The image shows a donut-shaped pattern that arises from the residual z-component of the electric field, when circular polarization is used. Deviations might occur due to beam aberrations or the orientation of the molecule. During lateral pre-localization, the emitter was centered to the middle point of the donut pattern.
In summary, we have found a good agreement of the lateral and axial experimental PSF pattern with the numerical calculations of figure 2.5(a). Further, the intensity at the minimum is 400 times suppressed in comparison to the intensity at the maximum (see section 4.3.1).

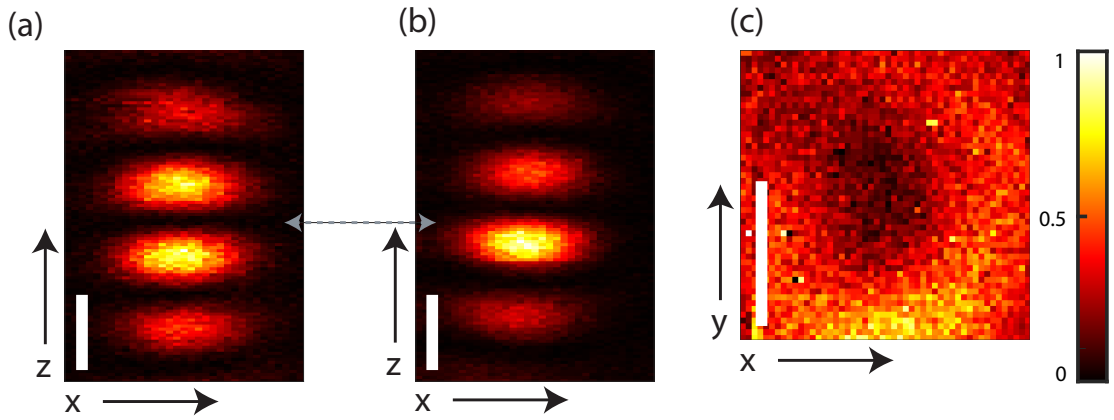

Figure 4.1: 4Pi PSF measured with a single molecule (Atto 647N) with circular illumination polarization. (a) Axial PSF pattern in destructive illumination mode, i.e. symmetric with respect to the focal plane (grey arrow). This PSF was used in the the middle (second) exposure of axial MINFLUX localization. (b) Axial PSF pattern which has a shifted minimum position with respect to the focal plane (grey arrow). The asymmetry of the first side maxima may arise from by photo-physics of the molecule or residual inhomogeneities of the illumination light. This pattern was used in the third MINFLUX exposure, in which the minimum was translated by $L/2$. The PSF pattern of the first exposure is similar to (b) but with the minimum at $-L/2$, not shown here. (c) The lateral PSF pattern measured in the focal plane of the symmetric PSF (a). The residual light intensity in the lateral plane leads, due to the circular polarization, to a donut pattern of detected photons. All PSF patterns are in good agreement with the numerical simulation shown in figure 2.5(a). Excitation wavelength: 640 nm. Pinhole: 1 AU. Scale bar: 250 nm.

4.2 Verification and calibration of 4Pi-MINFLUX localizations

The precision with which a molecule is localized by the 4Pi-MINFLUX setup can be verified by tracking the molecule position while moving the sample stage, and comparing the MINFLUX localization results with the sample stage positions. Here, we moved the sample stage in a sinusoidal trajectory with a peak to peak amplitude of 40 nm and simultaneously tracked the sample stage movement with a commercial displacement measurement device (fiber based interferometer, see figure A.7). MINFLUX tracking was performed at a single green excitable fluorophore (Cy3b in TDE-buffer, excitation wavelength: 560 nm) where, on average only 26 photons contributed to each position estimation (measurement parameters are listed in table A.1). Fitting the trajectory of the MINFLUX position values as well as of the reference position values with a sinus function defined by

$$f_{fit}(z) = 1/2 \cdot A \sin\left(\frac{2\pi}{T} z + 2\pi C\right) + D \tag{4.1}$$

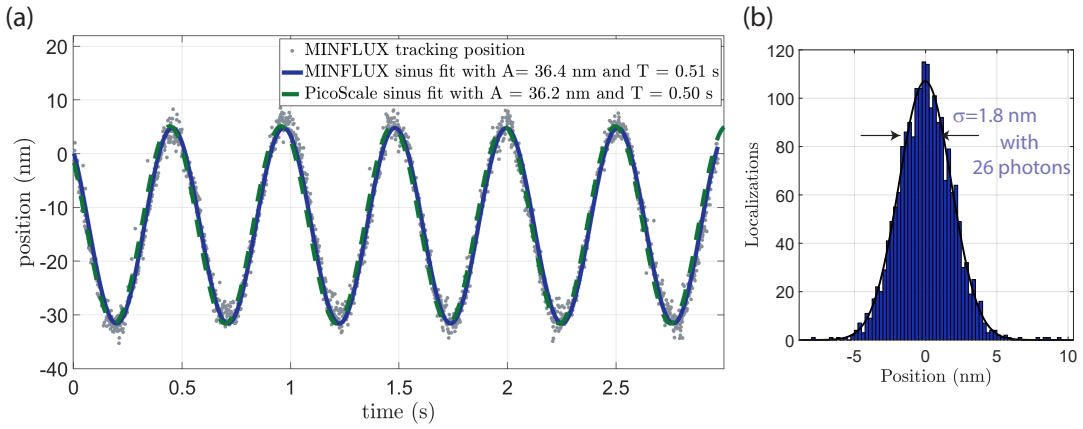

Figure 4.2: MINFLUX tracking of a single molecule (Cy3b) during continuous sinusoidal sample stage movement with a peak-peak amplitude A of 40 nm. (a) Position trace of MINFLUX tracking accurately follows the movement of the sample and a sinusoidal fit to the data shows good agreement with the theoretical amplitude (see legend). The movement of the sample stage was simultaneously tracked with a commercial displacement measurement device at a distance of 2 cm from the focus. Only the fit results to this data are shown for this measurement (green dashed lines) which achieve an amplitude similar to the MINFLUX tracking. For better visibility, the two independent but not synchronized measurements were overlaid manually along the time axis. (b) Histogram of the residuals of the 2500 MINFLUX tracking position values displayed in (a). The standard deviation of the residuals is $\sigma_{exp} = 1.8$ nm. The expected localization uncertainty would be 1.1 nm (according to equation 2.21). This underlines that the MINFLUX scheme can achieve single nanometer localization precision with only tens of photons. Bin size of (b): 0.25 nm.

resulted in an amplitude value A of (36.4 ± 0.2) nm and (36.2 ± 0.3) nm, respectively (the error defines the 95% confidence interval of the fit, see figure 4.2(a)).[1] Hence, we can conclude that 4Pi-MINFLUX was calibrated correctly, and that electro-optic control of the PSF pattern works reliably to reposition the minimum of the PSF pattern along the axial direction.[2]

By calculating the standard deviation of the residual of the sinusoidal fit to the MINFLUX position values, the localization uncertainty was estimated to about $\sigma_{exp.} = 1.8$ nm (figure 4.2(b)). The expected standard deviation based on the photon statistics is 1.1 nm, which shows that residual instrument-caused uncertainties are less than one nanometer.

In conclusion, these results highlight that the MINFLUX tracking measurements can follow a continuous movement of the sample stage with less than 30 photons, and at the same time achieves molecular localization precision. Since the scan speed was

[1] The systematic underestimation by approximately 10 % of the amplitude, which was also observed at both smaller and larger oscillation amplitudes, can be attributed to the inertia of the coverslip, the viscosity of the oil, or the bending of the very thin but large coverslip.

[2] This conclusion is only valid when the refractive index of the medium is matched with the one of oil [50].

limited by the time response of the sample stage to ensure reliable movements, we aimed in this experiment for a long tracking measurement (∼3 s at 0.67 kHz sampling rate), rather than an emitter tracking with high temporal resolution. However, there are no restrictions from the point of view of the experiment to performed MINFLUX tracing or tracking with higher sampling rates, as will be shown for 10 kHz sampling rate in section 4.3.1 and for 130 kHz sampling rate in section 4.4.4. In contrast, lateral 2D MINFLUX tracking has achieved 2 nm localization precision with 400 µs temporal sampling—i.e., 200 µs per dimension [51].
In figure A.8 an example of a stepwise stage movement in MINFLUX tracking mode is given. Here, on average 450 photons were used to achieve a localization precision of the step levels to less than 1 nm. The resting position after each step was clearly resolvable. These result show for the first time that a sub-nanometer localization precision can be achieved with less than 1000 photons.

4.3 Spatio-temporal localization precision in 4Pi-MINFLUX

In this section, the localization uncertainty will be discussed based on single molecule MINFLUX tracing measurements of a red excitable Atto 647N fluorophore. Beside the photon statistical limitation and the background contributions there are other factors influencing the localization uncertainty. For example, mechanical or electronic vibrations of intra-cavity devices, or thermal drift. The magnitude of both sources of uncertainty is dependent on the chosen measurement parameter. Vibrations, for example, can average out when the dwell time is set to be larger than the oscillation time of the vibration. On the other side, the impact of the thermal drift is mainly determined by the total measurement time. In summary, the experimental localization uncertainty σ_{exp} can be approximated with contributions arising from

- photon statistics, including a background photon influence σ_{1D} (equation 2.21),
- vibrations (mechanical and electronic) σ_{vibr} and
- thermal drift $\sigma_{therm.\,drift}$:

$$\sigma_{exp} \approx \sqrt{\sigma_x^2 + \sigma_{vibr}^2 + \sigma_{therm.\,drift}^2} \tag{4.2}$$

Measurement settings The MINFLUX localization uncertainty was studied for three different sampling rates (1, 5.5 and 10 kHz). For each sampling rate, the laser power in the last MINFLUX iteration step was adapted to measure roughly 10 photons in total. This lead to a mean fluorescence count rate of 8, 44 or 120 kHz measured at 5 to 10 molecules for the respective sampling rate. The L-value was set to 15 nm. In an additional measurement with 1 kHz sampling rate, the L-value was decreased

to 10 nm, which allowed for measuring with an optimal SBR (see section 4.3.3). In order to probe different photon count regimes with independent measurements for the 1 and 5.5 kHz sampling rate, the measurements were performed with three different dwell time factors (1x, 5x, 50x). Further measurement settings are stated in table A.2.

4.3.1 Sampling rate dependent localization uncertainty

Data Analysis

In the following, an exemplary analysis procedure is presented that was applied to all measurements. The photon count trace of the single MINFLUX exposures, as well as the total photon sum are shown in figure 4.3(a) (1 kHz sampling rate with 5x dwell time factor). We segmented the trace of the total photons into intervals of constant emitter brightness by using the Matlab function *findchangepts*. By doing so, the point of photo-bleaching, or of conformation change of the emitter, can be identified. For further analysis, the interval before bleaching was used. If multiple intervals of different photon rates were present, the interval with the highest photon rate, was used. In order to extrapolate from the starting photon counts per measurement ($\sim$10 photons) towards a higher photon counts regime ($\sim$1000 photons), single MINFLUX measurement were taken together by summing up the respective exposure photon counts (binning factor between 1 and 100). In order to maintain a sufficiently large number of localizations for the statistical analysis, we limited the binning factor to a value which ensured that at least 50 independent localizations were achieved.
In figure 4.3(b) the position trace that results from the photon counts from figure 4.3(a), is shown. We calculated the positions with the normal estimator (equation 2.10) and the modified estimator (2.23). Since only the modified estimator yields minimal uncertainty over the whole range of photons, this position estimator was considered in the following analysis of the localization uncertainty.

Results

In figure 4.3(c) and (d) the experimental localization uncertainty of multiple static molecules is plotted versus the total photon counts for the 1 kHz and 10 kHz sampling rate. In both cases, the averaged data points follow the theoretically expected inverse square root relation to the photons quite well, but differ from it along the whole photon count range. In the measurements with 1 kHz sampling rate 40 photons were on average necessary to achieve a localization uncertainty of 1 nm. For this number of detected photons the relative deviation from the expected localization

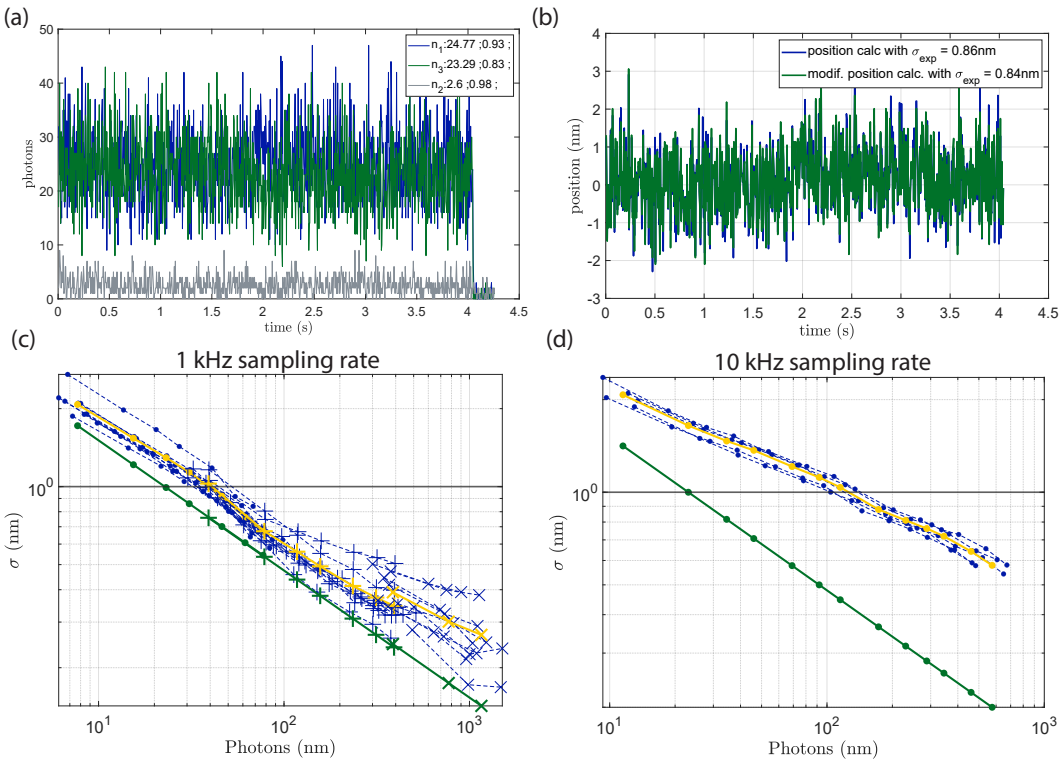

Figure 4.3: MINFLUX tracing (L=15 nm) of a static single molecule (Atto 647N) with varying sampling rates i.e. fluorescence count rates. (a) Photon counts from a representative measurement of 1 kHz sampling rate and 5x dwell time factor. At around second 4 photo-bleaching of the dye occurs. The mean photon numbers of each exposure for the intervals before and after photo-bleaching are stated in the legend. (b) Calculated position trace from (a) with two different position estimations (normal estimator 2.10 and modified estimator 2.23). The value of the standard deviation of each estimator is stated in the legend. The modified estimator achieves a localization uncertainty of 0.8 nm for a mean total photon count of 50. (c) and (d) localization uncertainty plotted against binned number of detected photons for 1 kHz (8 kHz) and 10 kHz (120 kHz) sampling rate (detection rate), respectively. The yellow curve represent the average results obtained from 7 to 10 measured molecules (blue curves). For the 1 kHz sampling rate, three measurements were performed with 1x, 5x and 50x dwell time factors (dot, plus and cross marker, respectively). Deviations of the average uncertainty and the expected uncertainty based on photon statistic σ_{1D} (equation 2.21) stem from additional noise contributions (see figure 4.4).

uncertainty value (σ_{1D}) is 30 %. In contrast to the expectation, the uncertainty approaches a lower limit of around 0.3 to 0.4 nm, when further measurements are binned together. Thus, measuring longer to achieve a higher number of detected photons does not improve the localization precision. Similar relations can be stated for the 10 kHz sampling rate, but in general a larger deviation from the theoretical value was observed for all photon counts. In the subsequent section we will study the source of the additional measurement error using Fourier analysis.

4.3.2 Spectral analysis of noise contributions

In order to determine the source of the deviation of the measured localization uncertainty from its theoretical limit, the mean power spectral density (PSD) was calculated from the position traces for 1 kHz and 10 kHz (figure 4.4(a) and (b), respectively). By comparing the measured spectrum to the expected constant spectrum arising from Poisson statistics (white noise), we can pinpoint two different contributions which differ in their spectral characteristic and can be attributed to σ_{vibr} and $\sigma_{therm.\,drift}$:

- narrow and high peaks at multiple frequencies
  - spectral characteristics of vibrations (mechanical and electronic)
- broad peak with a ∼1/f amplitude in the low frequency regime (<5 Hz)
  - spectral characteristics of thermal drift

The comparison of both spectra reveals that in the spectrum of the 10 kHz sampling rate more and sometimes higher peaks were present. Since these peaks have been averaged out in the lower sampling rate, they are resposible for the larger cumulative uncertainty. In both spectra, the two largest contributions were responsible for approximately 95 % of the total deviation of the measured from the expected uncertainty. In order to identify the source of the peaks, we performed MINFLUX localization measurements with the different elements of the system independently switched off in between measurements, while measuring a reflecting surface. From these measurements the spectral contributions could be traced back to the following three influences:

- Vibration of the tip/tilt piezo: 92 Hz and 512 Hz as well as their higher harmonics.
- Mechanical oscillation of the elevated cavity mirror in the upper beam path: 100 Hz.
- Alternating current hum: 50 Hz.

No resolvable influences were found for the sample stage, objective motors or fans used for cooling. Based on ongoing setup improvements, we could eliminate the influence of the piezo by temporarily slowing down the feedback loop of the piezo driver during the measurements (see appendix A.9). Further, mechanical reconstruction of the elevated cavity-mirror holder aided to reduce its susceptibility to external vibration. In summary, only the noise arising from 50 Hz, 100 Hz and low thermal drift frequencies remained in the spectrum.
The residual contributions arising from the baseline of the PSD at both sampling

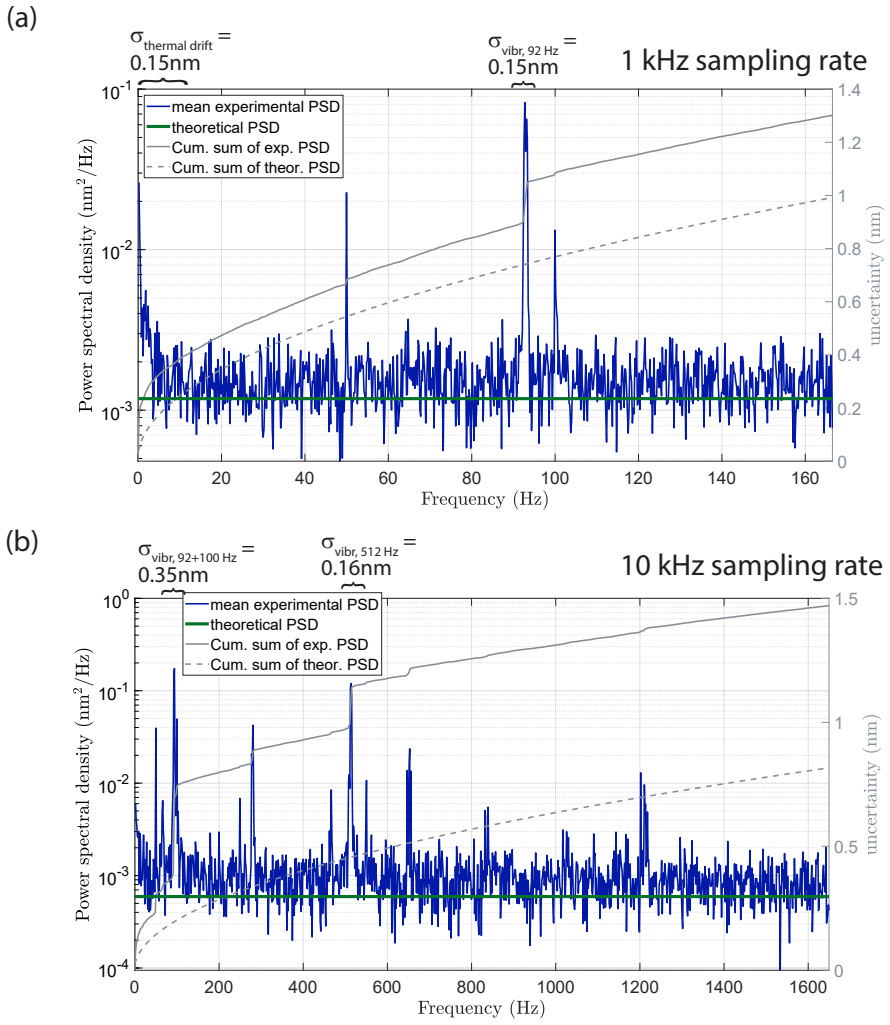

Figure 4.4: Average power spectral density (PSD) of the MINFLUX tracing measurements at single Atto 647N (figure 4.3). (a) 1 kHz sampling rate and 3x binning and (b) 10 kHz sampling rate with 3x binning. The uncertainty (square root of the integrated PSD values) is plotted on the right y-axis of each plot. In addition, expected values of the PSD (green) and the uncertainty (grey), which are caused by photon statistics, are given. The two main peaks in each spectrum are responsible for ∼95 % of the deviation of the experimental and expected uncertainty. The additional uncertainty caused by these two peaks was determined by taking the difference between the background subtracted cumulative uncertainty before and after the peak (values stated the respective plot). Note that due to the different sampling rate, the individual sources of noise contribution may differ between drift or vibration.

rates might be still white noise arising from microscope devices. However due to its small amplitude of <0.1 nm it was not possible to determine the source.

4.3.3 Improvements of the localization uncertainty with a smaller L-value

After having analyzed the systematic limitations, we further wanted to determine whether the number of photons needed for position estimation can be further improved

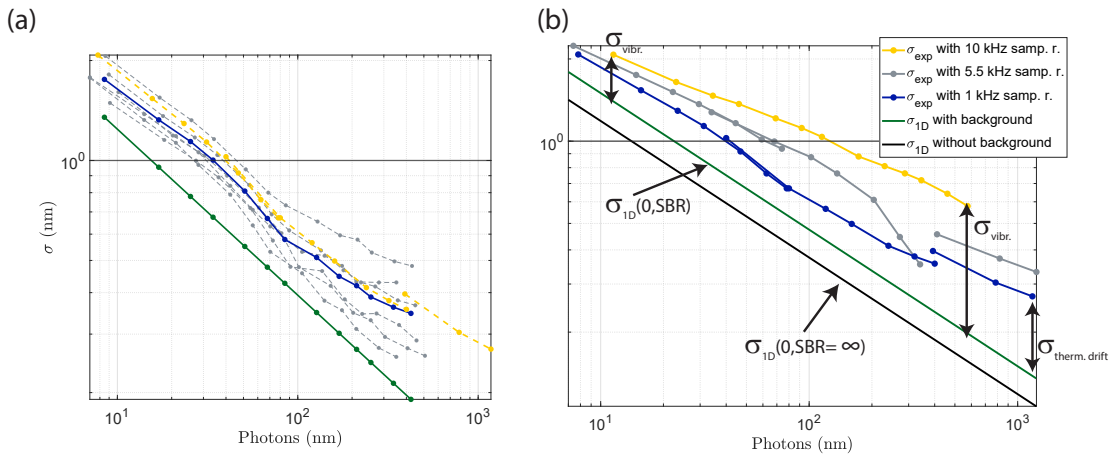

Figure 4.5: MINFLUX tracing ($L = 10\,\text{nm}$) of a static single molecule (Atto 647N) and summary of the results from figure 4.3 (a) Localization uncertainty with L-value of 10 nm at 1 kHz sampling rate measured at six single molecules (grey). The achieved mean uncertainty (blue) is compared with the mean uncertainty of measurements with $L = 15\,\text{nm}$ (yellow, from figure 4.3(c)). In the low photon count regime, a different uncertainty can be identified for the different L-values. Towards higher photon counts this difference is negligible. The mean SBR was 2.2 ± 0.9, thus closer to the optimal value of 1.2. (b) Comparison of the mean localization uncertainty for different sampling rates (1, 5.5 and 10 kHz). Starting from the photon statistic limit $\sigma_{1D}(0, SBR = \infty)$ the localization uncertainty increases due to background photon counts ($\sigma_{1D}(0, SBR)$). Mechanical and electrical vibrations ($\sigma_{vibr.}$) as well as thermal drift ($\sigma_{therm.drift}$) further increase the uncertainty of the measurement. Their influences depend on sampling rate and total measurement time. Approximated values of the magnitude of each contribution are summarized in table 4.1.

by performing MINFLUX measurements with a SBR-value closer to the theoretical optimum ($SBR(0, L_{min}) = 1.2$). Therefore, we repeated the measurement with a reduced L-value of 10 nm and a sampling rate of 1 kHz. The single molecule results are shown in figure 4.5(a) in comparison with the averaged results from the measurement with larger L-value (figure 4.3(c)). With ~ 35 photons per 1 nm localization uncertainty, a higher photon efficacy could be stated for the smaller L-value. However, towards the high photon count regime, both measurements converge to the same value of approximately 0.3 nm. Due to the heterogeneity of the emitter, we discarded more data of the measurement with the smaller L-value by demanding a SBR larger than 1.

4.3.4 Summary and discussion

Localization uncertainty contributions When combined, vibration and drift contributions are responsible for more than 95 % of the deviation from the expected value of the localization uncertainty, independently from the sampling rate. However, their impact is dependent on both the sampling rate and the total measurement

Source of uncertainty contribution	Estimated magnitude	Characteristics
Photon statistics ($\sigma_{1D} = \sigma_{1D,CRB}$)	1 nm	15 photons detected (L =15 nm)
Background photons	0.3 nm	30 % of σ_{1D} (for $SBR(L_0) = 400$)
Mechanical and electrical vibrations ($\sigma_{vibr.}$)	(a) 0.3 nm (b) 0.6 nm	for 1 kHz sampling rate for 10 kHz sampling rate
Thermal drift ($\sigma_{therm.\,drift}$)	0.2 or 1 nm	thermally equalized or non equalized (total measurement time ∼6 s)

Table 4.1: Summary of the contributions influencing the MINFLUX measurement uncertainty. The contributions arising from the photon statistics and background photons are mainly determined by the microscope. Influences of vibrations and thermal drift depend on dwell time and measurement time.entra Both contributions hampered the MINFLUX measurement to achieve localization uncertainties below 0.3 nm. The SBR correction factor is shown for different SBR-values in figure A.1(b)

time. For example, vibrational influences are averaged out if the total dwell time of a measurement is longer than the oscillation time.[3] An overview of the magnitude of the individual contributions of the MINFLUX localization uncertainty is given in table 4.1. In addition, the single noise contributions are labeled in the comparison plot of the localization uncertainty against the total measured photons per measurements with 1, 5.5 and 10 kHz sampling rate (figure 4.5(b)).
Using signal analysis tools, the contributions based on vibrations can be suppressed with a spectral band stop filter. Drift contributions can be compensated with high pass filtering of the position data (see filtered MINFLUX tracing data in figure A.10).

Buffer When using the TDE-buffer, we achieved sufficiently stable count rates and gained a sufficiently large total number of detected photons for both types of dyes studied (carbo-rhodamine: Atto 647N and cyanine: Cy3b, see section 4.4). Further, no significant influence of the dye's photo-physical properties, e.g. blinking, was observed. Thus, it does not seem to be necessary to use an additional photo-stabilizing system, e.g. a reducing and oxidizing system [52], which was used by Balzarotti *et al.* in aqueous buffers [22]. However, in future work photo-stabilizing additives may lead to further improvements towards a more stable photon rate at high illumination power, when their concentration is adapted to the viscous TDE-buffer.

[3] Compare photon count range 70 to 80 with sampling frequency 83 and 71 Hz in figure 4.3(c). Here, the effect of the 92 Hz oscillation is averaged out.

Background photons The mean ratio of detected photons in the middle exposure (n_2), before and after photo bleaching of the emitter, was 4±1.3 for 1 kHz and 5.5±1.2 for 10 kHz sampling rate. Thus, we conclude that most background photons were caused by an incomplete destructive interference. Surprisingly, background photons did not predominantly stem from luminescence processes in the sample. Thus, if residual optical imperfections could be overcome, the SBR could be increased by a factor of 4. These findings highlight that, by using 4Pi-optics, the illuminated light dose could be decreased allowing for 1000-fold decrease in the number of detected photons in the minimum compared to the maximum. In the following section, the optical illumination scheme was adapted to enable measurements with improved SBR.

Measurement settings Based on the variance of the SBR measured for single molecules, a choice has to be made between few MINFLUX localizations requiring a low number of photons and a higher number of valid MINFLUX measurements. If the aim is to obtain many valid measurements, the L-value should be chosen such that a SBR of 3 to 5 is reached. If, instead, few high-quality measurements are sufficient, an optimal L-value can be used—i.e., $SBR \approx 1.5$ to 2.

4.4 Maximizing the precision content of a photon: 20 photons required for 1 nm localization precision

The MINFLUX localization precision depends on a scalable spatial parameter (L-value) based on which the precision increases with the square root of the numbers of detected photons. Hence, the information content of a photon about the emitter position becomes especially valuable if low number of background photons are detected and the smallest optimal L-value can be used. Therefore, tailoring the optical illumination settings of 4Pi-optics to get the highest curvature of the intensity minimum is essential.

4.4.1 Experimental changes towards optimal illumination conditions

In order to measure under ideal conditions to achieve a high SBR, and thus a minimal L-value, we introduced changes in the optical setup by implementing green illumination light ($\lambda_0 = 560$ nm) and linear polarization of the illumination light. Compared to red excitation wavelength, the value of the full width at half maximum in the minimum of the illuminations PSF could be decreased by 14 % leading to: $fwhm_{ax}^{560nm} = 218$ nm. Further influences, such as a more stable operating laser

or less luminescence background from the sample, can lead to lower number of detected background photons. In summary, we found lower background counts that led to a high SBR measured at more bleaching-susceptible molecules such as Cy3b [53]. Other green emitting fluorophores, like Atto 565, exhibited a strong blinking behavior or emitted a low number of photons (<5000) before photo-bleaching.

4.4.2 Statistical analysis of single fluorescent molecules

Measurement settings In order to estimate the improvement in localization precision, we performed MINFLUX tracing measurements with $L = 15\,\text{nm}$ and 1 kHz sampling rate. The analysis of the resulting 46 MINFLUX tracing data sets was similar to the protocol stated in section 4.3.1. Further measurement parameters are stated in table A.3 and the measurement routine of MINFLUX tracing and tracking was explained in section 3.4.

Results The single molecule results shown in figure A.10(a), were evaluated by the number of detected photons that were required for 1 nm localization precision, and the measured $SBR\,(L = 15\,\text{nm})$ (see figure 4.6(a)). The results follow the theoretical prediction of the photon statistics- and background photons-limited value over the whole SBR-range and the offset of the experimental data to the theoretical value can be attributed to vibrational noise and drift (similar to section 4.3.2). The effect of the thermal drift was demonstrated by analyzing the same single molecule data first without any filter applied and later, after applying a high pass filter at 5 Hz (see figure A.10(b)). Further, the single molecules exhibited a larger variance of the SBR-values when compared to the results for circular polarization of the illumination light: 7.4 ± 6.9 (mean and standard deviation).[4] From the largest achieved SBR-value we derived a new SBR-value based on the minimum and maximum intensity of a standing wave: $SBR(0, L = 218\,\text{nm}) \leq 2150$. This highlights that we achieved a more than 1000-fold extinction of the illumination intensity in the minimum compared to the maximum.

An explanation for the large variance of SBR-values can be the interplay of randomly distributed molecular transition dipole orientation and the z-component of the electric field in the lateral plane (see figure 2.5(a)). Assuming non-optimal lateral centering of the dye, the latter can be excited by the residual electric field leading to an increase of the measured background counts. Consequently, the SBR is dependent on the orientation and the rotational degree of freedom of the emitter as well as its prelocalization.

[4] On average, the relative error of the SBR of a single molecule MINFLUX trace was 33 %.

To support this hypothesis, we performed a correlative study of the molecular brightness in the x-y-scan, the fluorescence extinction by polarization modulation and the SBR in MINFLUX tracing measurements (see appendix A.11). The results revealed that there is a linear correlation between the measured SBR-value and both fluorescence extinction and emitter brightness.

Conclusion We conclude that some of the immobilized Cy3b molecules exhibit a fixed transition dipole moment. If this dipole was exclusively oriented along the polarization of the illuminated beam (e.g. x-direction), the dye exhibits the highest SBR and appears the brightest in the overview scan.

4.4.3 MINFLUX localizations with minimal L-value

Based on these findings, we limited our investigation to the 10 % brightest dyes on the coverslip. For a sub-population of 20 %, the low number of detected background photons in the middle exposure allowed for setting the L-value down to 6 nm in MINFLUX tracing and tracking measurements. Here, an optimal SBR was achieved. In MINFLUX tracing measurements, the 1 nm localization uncertainty benchmark was reached with roughly 20 photons (figure 4.6(b)). In one third of the measurements only 10 photons were required. The localization uncertainties of multiple MINFLUX tracking measurements are plotted against the measured photons (figure 4.6(c)) or SBR (figure 4.6(d)). Similarly to MINFLUX tracing, these results show that molecular localization precision can be achieved with a low number of photons.
In summary, these results underline that high precision measurements are possible with a low number of detected photons. Furthermore, they highlight the importance of a scalable and iteratively adaptable L-value, which in the most ideal case can be adapted individually to each emitter.

4.4.4 MINFLUX localizations with highest sampling rate

Measurement settings In a further measurement (MINFLUX tracing with L=10 nm) we verified the 4Pi-MINFLUX performance with respect to a maximal sampling rate. The sampling rate was limited by the time required to perform the shift of the intensity minimum (∼0.3 µs). In order to measure with a sufficiently large duty cycle (ratio of total exposure dwell time ($3 \cdot T_{dwell}$) to total measurement time T_{tot}, see figure 3.4) we set the sampling rate to ∼130 kHz using T_{dwell} =2 µs. We illuminated the molecules with a high laser power (1 mW in the back focal plane of objective 1 and ∼ 20 % more in objective 2) to achieve a fluorescence detection rate of roughly the same order as the sampling rate. The high illumination intensity, however, led

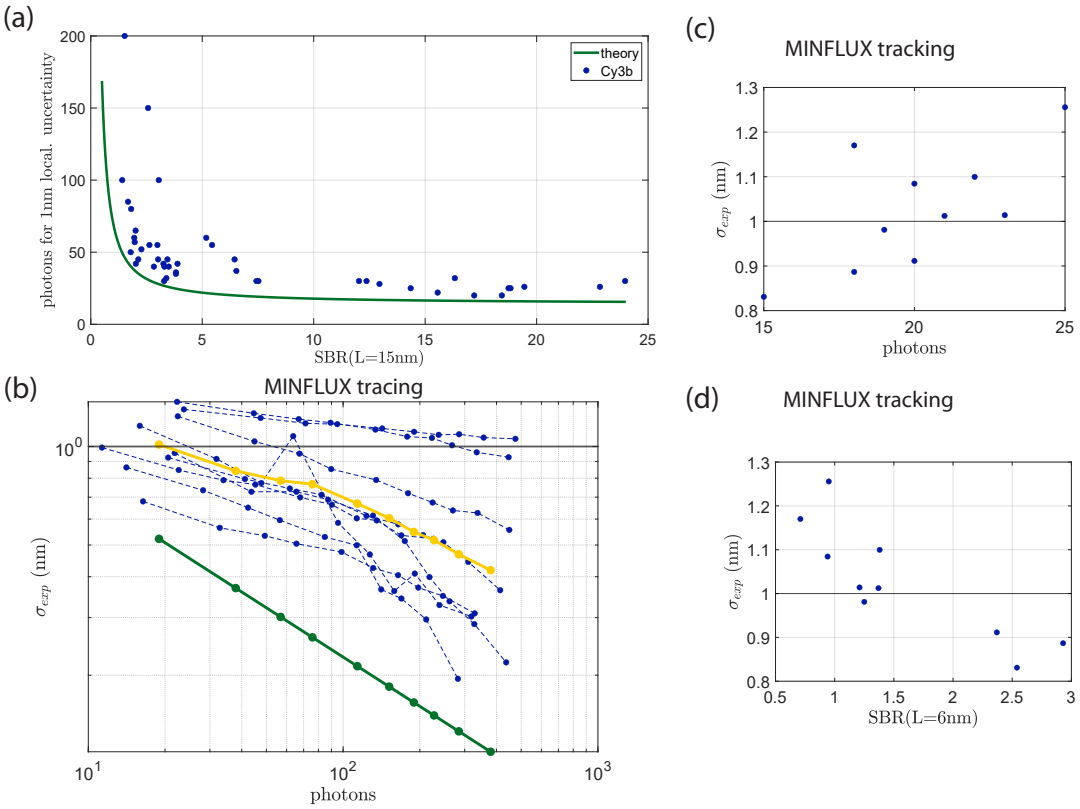

Figure 4.6: MINFLUX measurements with the minimal achieved L-value at single static molecules (Cy3b) (a) Photons required for 1 nm localization uncertainty plotted against the measured SBR. The corresponding single molecule data are shown in appendix figure A.10. The high variance of the SBR-values was caused by an imperfect centering of the molecule in the lateral plane leading to a higher number of detected background photons for the molecules that have a transition dipole moment orientated along z-direction. (b)-(d) MINFLUX measurements with $L = 6$ nm of molecules with a SBR-value larger than 10 ($\sim$ 20% of the dyes shown in (a)). (b) Uncertainty of MINFLUX tracing measurements plotted against the number of detected photons. The average uncertainty (yellow) of the single molecule data (blue) shows that an uncertainty of 1 nm is reached with close to 20 photons. (c) and (d) The uncertainty of MINFLUX tracking measurements is plotted against the number of detected photons (c) or the SBR (d). Considering only emitters with SBR greater than 1, a one nanometer tracking precision is achieved with less than 20 photons.

to direct photo-bleaching for most studied molecules. A sufficiently large number of detected photons (>5000) could only be acquired for less than 5 molecules.

Results The best of these results is shown in figure 4.7 including a demonstration of two different analysis methods. Here, on average, three photons were detected per MINFLUX localization with an average SBR of 8.6 (figure 4.7(a)).[5] The resulting position trace of 76 ms length reveals that an oscillation is present (figure 4.7(b)).

[5] In order to gain a high number of valid measurements, we set the L-value to a larger value than the optimum (see section 4.3.3).

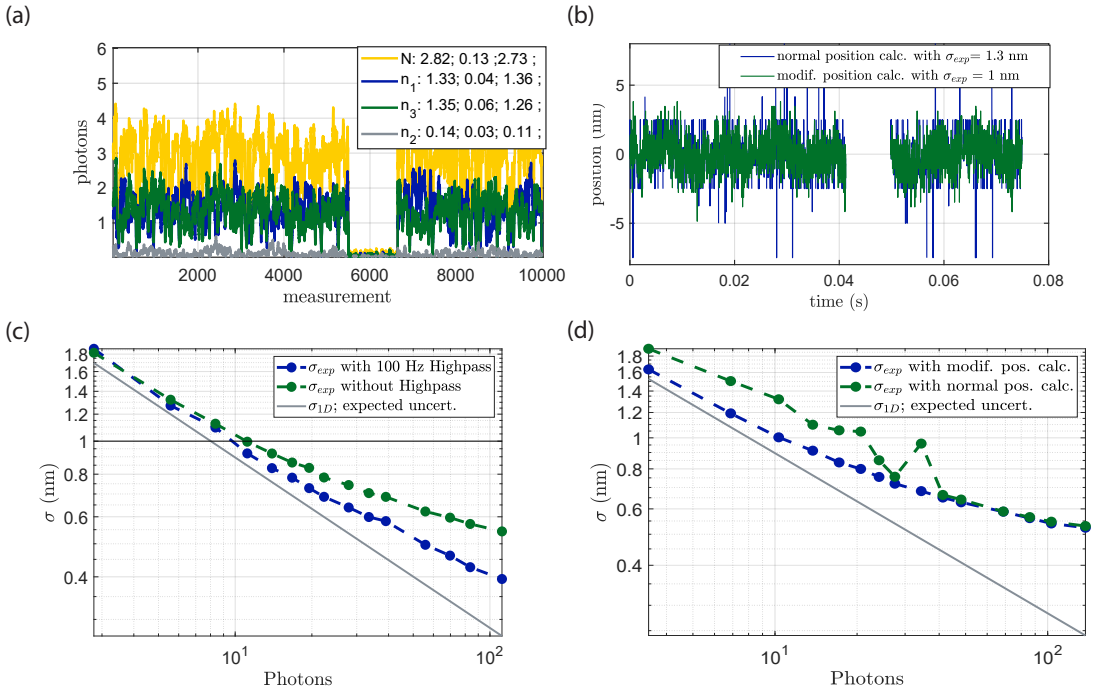

Figure 4.7: MINFLUX tracing of a single static molecule (Cy3b) with 130 kHz sampling rate. (a) Detected photon count time trace with on average three photons per 7.6 µs, leading to a fluorescent count rate of 400 kHz. For better visibility, the photon counts are smoothed with a smoothing filter of window size 30. The molecule exhibited a single blinking event (around measurement repeat 6000). Irreversible photo-bleaching could be demonstrated in a subsequent measurement under the same conditions. The measurements of the first and the third interval were used in the analysis of (c) and (d). Mean photon counts are given in the legend. (b) Position trajectory of the measurement in (a) for the normal and modified estimator. Measurements with zero detected photons were discarded. An oscillation with a frequency between 90 and 100 Hz is visible (compare figure A.12). (c) Experimental uncertainty without filtering of zero photon measurements but with 100 Hz high pass filtering. Here, localization uncertainties of 0.4 nm— i.e., one one thousandth of the wavelength, were achieved with 100 photons. (d) Experimental uncertainty of the two position estimators (as shown in (b)) is plotted versus the number of detected photons (binned measurements). Measurements with zero photons detected were discarded.

Using Fourier analysis, we found that the frequency of the oszillation falls in the range of 92 to 100 Hz (figure A.12). The most probable cause of the vibrational influence is the microscope (tip/tilt piezo) and not the molecule (see section 4.3.2). Thus, applying a high pass filter with a filter edge at 100 Hz is sufficient to remove this oscillation.[6] The resulting localization uncertainty plotted against the binned number of detected photons shows that an improvement of 0.2 nm was achieved in the high photon count regime (figure 4.7(c)). Here, the standard deviation of roughly 150 consecutive MINFLUX localizations was only 0.4 nm.

In addition, we performed an analysis in which measurements with zero detected

[6]Note that even when 6 measurements are binned together, the high pass filter eliminates less than 1 % of the total frequency spectrum width.

photon were discarded. These events occurred on average once in five measurements and could be caused, among other things, by the statistics of the measurement process or by the emitter exhibiting a blinking behavior. Interestingly, the localization uncertainty in the low photon regime is slightly improved compared to the previous analysis (figure 4.7(d)). Due to the residual oscillation, uncertainties below 0.6 nm were not achievable. Since in this analysis the temporal information of the individual measurement was lost, we did not apply high pass filtering. Measurements of gold nanoparticles, of which the plasmonic property allows an even higher emission rate, revealed a similar performance of the microscope.

Conclusion We could show that the 4Pi-MINFLUX is capable of locating single emitters with a high sampling rate. In general, the localization uncertainty of a single MINFLUX measurement is better than the uncertainty calculated from the standard deviation of repeated measurements, because the reference position of the interferometric localization and ultimately the emitter position itself may not be constant during the period of the repeated measurements. To that end, measuring with a high fluorescence detection rate allows to reduce the measurement time and consequently minimizes the influence of thermal drift. Here, 4Pi-MINFLUX additionally benefits from the doubled detection efficiency due to the second objective lens. When the residual noise can be accurately attributed to a microscope device, band-stop filtering can be applied to the remove this unwanted influence from the data. With ongoing setup improvements, we have shown that vibrations arising from the microscope could be reduced or completely eliminated in the higher range of the frequency spectrum (>500 Hz, see figure A.9). Thus, a validation of the MINFLUX concept with a localization precision down to the Ångström-range might be feasible.

5 Axial 4Pi-MINFLUX imaging

The axial resolution of the 4Pi-MINFLUX microscope was verified by localizing single fluorophores incorporated into a DNA origami nanoruler. Nanorulers are artificial DNA nanostructures of designable size and shape, at which fluorescent molecules can be incorporated at nearly any distance and with high specificity and precision [54]. DNA nanorulers are used in various applications, ranging from quantitative characterization and calibration to proof-of-principle measurements of new microscopy techniques (DNA-PAINT [55], 2D MINFLUX [22], MINFIELD STED [56]).
We chose a nanopillar that has three labeling points of single Alexa Fluor 647 with distances of 10 and 20 nm along the axial direction (see figure 5.1(a)). This DNA origami structure features a cuboid shape. Specific binding sites at the bottom base plate ensure a perpendicular orientation of the labeled axis of the nanopillar with respect to the coverslip surface—i.e., parallel to the optical axis. Single molecule blinking was established by (1) adapting a STORM buffer to the requirements of the 4Pi-MINFLUX and (2) photo-activating the fluorophores using an ultraviolet (UV) laser (405 nm, see section 3.5 and 3.4). In the following we present the data acquisition and analysis that was tailored for the MINFLUX imaging scheme as well as the statistical results of the imaged nanorulers.

5.1 Data acquisition and analysis

The MINFLUX imaging scheme consists of multiple repeats (2000) of a three step iterative MINFLUX localization (see section 3.4.2). Since a higher background photon count was observed, presumably caused by a higher residual excitation intensity in the minimum, we measured with a larger L-value (60 and 40 nm) compared to MINFLUX tracing experiments using the same excitation wavelength (640 nm, compare section 4.3). Further measurement parameters are listed in table 5.1.

Molecular blinking events

With Alexa Fluor 647 molecule attached the nanopillar, we observed intensity burst lengths of 50 ms $\pm$ 88 % and average detected photon counts of 3000 per burst, which allowed 6 localizations, with a total dwell times of 9 ms. An exemplary trace of the

MINFLUX imaging iteration step:	1st	2nd	3rd
L (nm)	120	90	60
exposure dwell time (ms)	0.5	0.5	2
multiplexing number	1	1	60
excitation laser power (µW)	2	5	20
expected photon counts	40	60	500
other parameters:			
total imaging time (s)	18		
repeat of localizations	2000		
activation laser power in the bfp of objective 1 (µW)	9		
photon count threshold for activation laser	20		
expected count rate (kHz)	30 - 40		

Table 5.1: Measurement parameters of the MINFLUX imaging experiments shown in figure 5.1, 5.2 and 5.3(a)-(c). The excitation laser power was measured in the back focal plane (bfp) of objective 1. The laser power at Objective 2 was ∼12 % larger.

total number of detected photons of all three MINFLUX iterations shows clearly resolvable single emission burst (5.1(b)). The mean detected photons per MINFLUX localization range around 550 photons, whereas single spikes of double intensity indicate a simultaneous activation of two emitters. The diverse blinking behavior, e.g. burst length, becomes visible in the magnified time window of the total photon counts of the last MINFLUX step (figure 5.1(c)). The UV activation laser created background counts of 40 photons. The individual counts of single exposures in the last MINFLUX step show that the pattern was sufficiently well localized on the active molecule after the preceding two MINFLUX localizations with in total 110 photons detected ($n_1 \approx n_2$, figure 5.1(d)).
The localization position trace of the magnified time window shows that all three molecules were activated (see figure 5.1(e)). The differently colored ranges represent the expected molecular position. Emission bursts, which were interrupted by short blinking events with a resting time of the molecule in the off-state of shorter than two repeats i.e. 18 ms, could be attributed to the same molecule (compare second 6).

Data filtering

The time trace of detected photons N of the measurement process depends on several statistical processes, such as the on-/off-switching of the dye and the Poisson noise of the low number of photons per exposure. Therefore, physically-motivated, robust criteria are required to discriminate invalid localizations from valid ones. For example, a localization has to be discarded if the fluorophore photo-bleaches during

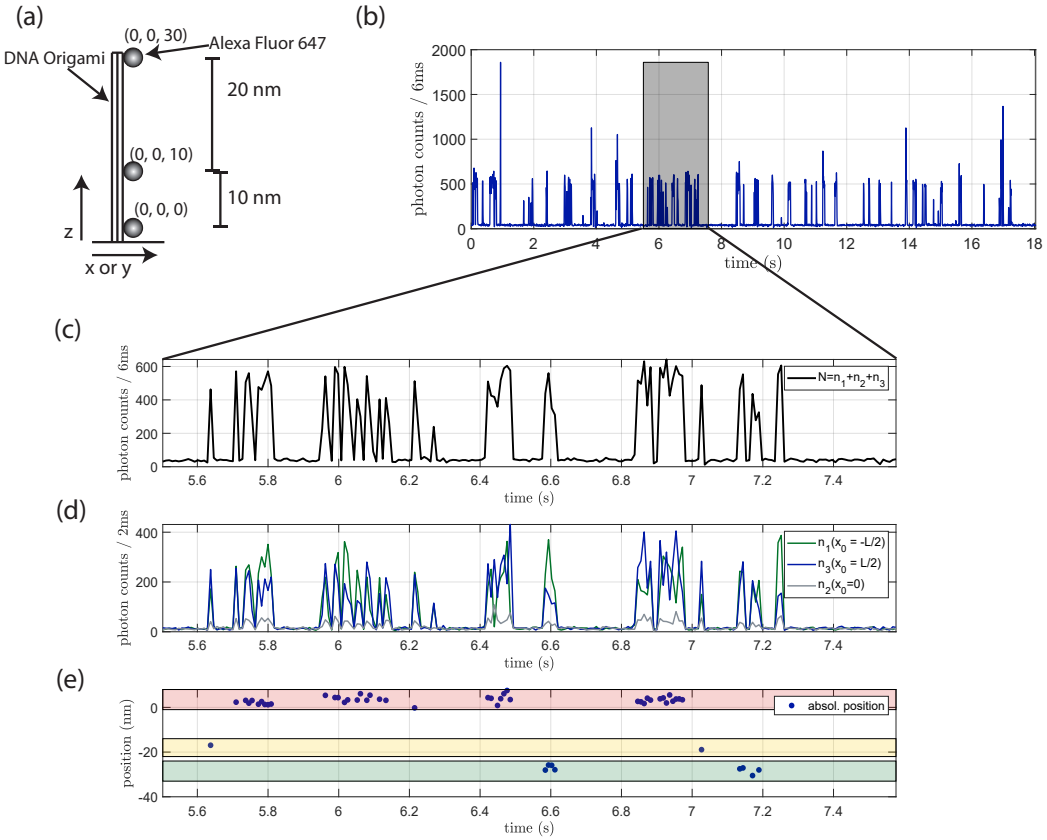

Figure 5.1: Design and measurement results of an exemplary DNA origami nanopillar (a) Illustration of the DNA origami nanopillar with three labelled Alexa Fluor 647 molecules. (b) Total number of detected photons in all iteration steps. Single burst events are clearly resolvable and, due to their nearly constant height, distinguishable from bursts with two activated molecules. (c) Magnification of the grey shaded area in (b). The blinking behavior of the fluorophores is clearly visible. (d) Detected photon count of each MINFLUX exposure from the interval shown in (c). (e) Calculated positions of the iterative MINFLUX process. From each valid event in (d) an emitter localization is extracted. One can see that each single burst stems from a single molecule and that these burst occur stochastically and have a different duration. The localizations of the three molecules are highlighted with different color shadings for better visualization.

the localization process, or if a second emitter appears. Another example occurs if one of the three exposures (n_1, n_2 or n_3) detects an exceptionally high or low number of photons arising from the Poissonian nature of the photon emission and detection processes. We defined invalid localizations as those measurements which fulfill at least one of the following criteria:

1. $n_2 > n_1$ or $n_2 > n_3$, which was only considered in the last iteration step
2. $N < N_{min}$, where N_{min} is the manually defined lower photon threshold
3. $N > N_{max}$, where N_{max} is the manually defined upper photon threshold
4. $SBR < SBR_{min}$, where SBR_{min} is the manually defined lower SBR threshold

After position calculation, where the first filter criterium was directly considered, the two photon threshold filters (figure 5.2(a)) and the SBR-threshold filter (figure 5.2(b)) reduce the number of valid localization by around 30 %. The localization histogram of the remaining 238 valid localizations reveals three points of clustered localizations (figure 5.2(c)).

Position data fitting – Gaussian mixture model

We analyzed the list of valid localizations using a Gaussian mixture model (GMM), which uses an expectation maximization algorithm and was supplied by the Matlab community (*gaussian_mixture_model.m*) [57].[1] The GMM assumes that each localization randomly stems from a Gaussian distribution defined by two parameters: a mean position μ and a standard deviation σ. The chosen fitting model consists of three Gaussian distributions, one for each emitter. The separation of neighboring molecules was determined by the difference of their mean position, while the localization precision was determined by the Gaussian standard deviation.

[1] The algorithm performs iteratively first an expectation step (determination of the log-likelihood function for the complete set of localizations) and afterwards a maximization step (maximization of the log-likelihood function for the parameter set) based on Gaussian models, until a user-defined quality value is reached.

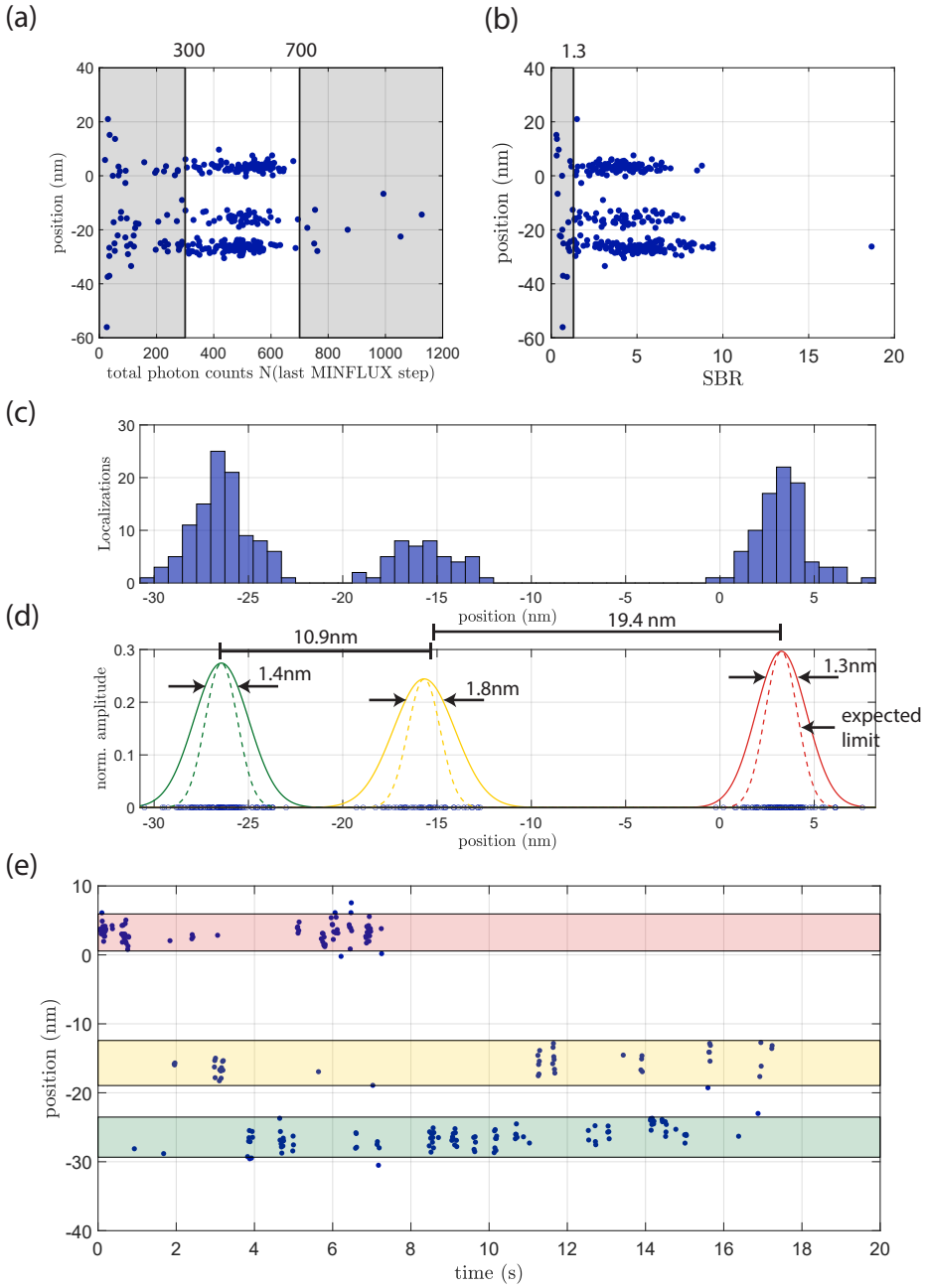

Figure 5.2: Exemplary analysis of a MINFLUX imaging measurement of a DNA origami nanopillar (a) Intensity filter: Invalid localizations were discarded using a lower (300) and an upper (700) intensity threshold. (b) SBR-filter: With the use of a lower SBR threshold (1.3), the filter should discard localizations of which the SBR lies under the optimal value. (c) Localization histogram of valid localizations after filtering. Bin size: 0.75 nm (d) GMM fit to the localizations shown in (c). Three Gaussian distributions were fitted to the distribution of localizations shown along the x-axis. Separation of neighbouring mean values and the uncertainties of the Gaussian distribution are shown in the plot. The measured distance is in accordance with the expected distance of 10 and 20 nm. The expected localization uncertainty was calculated to be 0.9 nm, based on the number of photons detected and mean SBR. This is illustrated as dotted line (normalized Gaussian function). (e) Position trace of the emission bursts shown in figure 5.1(b). The colored area marks the $\pm 2\sigma$-range of the localization uncertainty.

5.2 Experimental results

We applied the GMM on the filtered localizations of the exemplary nanopillar and extracted distances of the localization clouds—i.e., fluorophores, of 10.9 and 19.4 nm (figure 5.2(d)). These separations are in agreement with the expected distances of the fluorophores of 10 and 20 nm. The molecular localization precisions range between 1.3 and 1.8 nm for, on average, 500 detected photons per localization in the last iteration step and 610 photons in total. The expected localization precision based on measured photons and mean SBR was (0.9 ± 0.1) nm.[2] The measurement results are summarized in table 5.2. In the following, we want to verify if the localization precision can be improved by further analysis steps.

Clustering of localizations of single emission bursts Since an emission burst could be measured with multiple MINFLUX localizations, we adapted the analysis routine to allocate each emission burst only a single position value by taking the average value of the respective localizations. Further, we required that the UV laser was not activated during an emission burst. Here, the burst should not be intersected by short-term blinking, which, due to illumination of the activation laser, can lead to activation of another molecule. When performing the GMM analysis on the modified list of localizations, similar positions and standard deviations were achieved, which differed only in the 0.1 nm range. Thus, only minor improvements could be stated.

Linear drift correction Since the experiment was designed for short measurement times, we did not implement an active drift correction. However, during the 18 second long measurement time, a change of the mean position value could be observed for one molecule, which showed blinking events over the longest time period and is highlighted by the green interval in figure 5.3(e). We referred this unidirectional change of positions to thermal drift. Using a linear drift correction exclusively to the localization from the highlighted molecule, we could improve its localizations precision by 0.2 nm resulting in a 1.2 nm overall uncertainty. When the calculated drift parameters were applied to all localizations the mean localization uncertainty improved by less than than 10 % (towards 1.41 nm).

Statistical results From the roughly 170 measured nanopillars, 10 % appeared to have three labeled molecules, where only half (8) had exhibited clear blinking statistics

[2]The error of the expected localization uncertainty is the Gaussian error of the parameter N and SBR in equation 2.21:

$$\delta\sigma_{1D} = \sqrt{\left(\frac{\partial\sigma_{1D}}{\partial N}\delta N\right)^2 + \left(\frac{\partial\sigma_{1D}}{\partial SBR}\delta SBR\right)^2} \tag{5.1}$$

MINFLUX imaging results:	$L = 60\,\text{nm}$
distance (nm)	9.7 ± 1.6
	19.2 ± 2
localization uncertainty σ_{exp} (nm)	1.6 ± 0.3
Results of figure 5.2:	
average photons in last MINFLUX step	500 ± 85
average photons in all MINFLUX steps	610 ± 85
SBR	4.5 ± 2
expected localization uncertainty σ_{1D} (nm)	0.9 ± 0.1

Table 5.2: Results of the MINFLUX imaging measurements shown in figure 5.2 and 5.3(a)-(c).

to precisely differentiate three different fluorophores. We achieved roughly three times more valid measurements of nanopillars with exactly two labeled molecules. In figure 5.3(a) to (c) three more localization histograms and their respective results of the GMM analysis are shown. In all plots, the structure of three individual localization positions is resolvable and their precision ranges between 1 and 2.2 nm. However, the number of localizations differs strongly between the origamis, rising the potential of low statistical significance with less than 10 localizations. The averaged results of the fluorophore distances and their localization uncertainty are summarized in table 5.2.

MINFLUX Imaging with smaller L-value In a second measurement, we lowered the L-value to 40 nm to measure with more optimal SBR. Here, we measured 35 nanopillars from which one nanopillar appeared with three labeled fluorophores. We could measure five nanopillars labeled with two fluorophores. The results of GMM analysis of the fully labeled nanopillar reproduce, with 10.5 and 19.4 nm, the expected distances (figure 5.3(d)). The mean localization uncertainty of 1.3 ± 0.1 nm was slightly better than in the previous measurements. This can be explained by the L-value and the higher photon number in the last MINFLUX iteration step (640 photons with SBR of 2.7 ± 1.7). However, compared to the expected uncertainty of 0.6 nm, the measured value exhibits a larger deviation, absolute and relative.

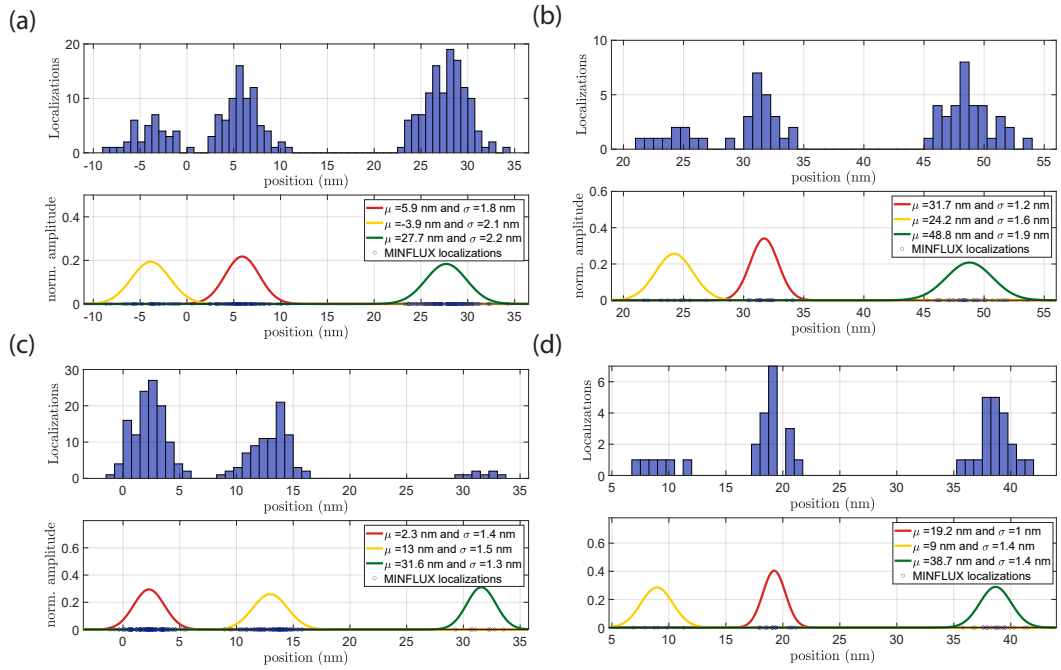

Figure 5.3: Localization histograms and results of the GMM analysis of representative DNA origami nanopillars. Three fluorophore positions were successfully localized at all nanorulers shown (see legend). (a) to (c) Measurements and data analysis were performed similar to figure 5.2. The L-value was 60 nm. (d) This measurement was performed with an L-value of 40 nm. The SBR was closer to the optimal value. Only a minor improvement of the localization precision was visible.

5.3 Summary and discussion

The 4Pi-MINFLUX microscope could successfully resolve the three fluorophore positions of Alexa Fluor 647 incorporated in the nanopillar. Two molecular separations of 9.7 and 19.2 nm were measured with an average localization uncertainty of less than 1.6 nm for 610 detected photons (see table 5.2). Measurements with a smaller L-value and higher number of detected photons have not significantly improved the localization precision, which was always higher than 1 nm.

Experimental imperfections led to a deviation of the localization uncertainty with respect to the limit given by photon statistics. This deviation of 0.7 nm was most presumably caused by thermal drift, since most vibrational influences average out due to the long measurement acquisition time. Due to residual excitation light in the intensity minimum, we measured with a larger L-value (60 nm) and invested ten times more photons per localization compared to MINFLUX tracing and tracking measurements of section 4.3.

We observed small deviations ($< 10\,\%$) of molecular separation from the designed structure. These differences could be pinpointed to several influences: (1) non-normal orientation of the nanopillar with respect to the surface, (2) changes of the geometrical properties like rigidity of the folded origami (potentially influenced by the $MgCl_2$

concentration in the buffer [58]), (3) incorrect calibration of the 4Pi PSF based on the non refractive index-matched buffer ($n_{med} \approx 1.4$) or (4) sub-nanometer variation of the emitter position due to its linker length ($\sim 0.6\,\text{nm}$) [54, 59]. Since the overall differences between measured and expected shape are small, the mentioned influences might either be minimal or balance each other out.

To achieve molecular localization precision in 4Pi-MINFLUX, both L-value and total number of detected photons were of similar magnitude compared to the pioneering experiments by Balzarotti *et al.*, who imaged lateral DNA origami structures [22]. Hence, the aberrations in both experiments were of the same scale. However, 4Pi-optics exhibits a clear improvement compared to the 3D MINFLUX measurements by Gwosch *et al.*, in which the smallest resolvable axial separations were in the order of 50 nm. This was due to the SBR-limited L-value of 100 nm and the resulting requirement of 700 to 1000 photons for single nanometer localization precision [24]. In general, all MINFLUX localizations show an improved performance compared to the 2500 photons required in camera-based localizations using a coherent double objective lens system [39].

The apparent incomplete labeling of the DNA origami can be explained in several manners, including: (1) an incomplete assembly of the DNA origami, (2) a low degree of labeling of the DNA strands that were incorporated in the nanopillar or (3) a degradation of the buffer leading to irreversible photo-bleaching of the dye before its transition to a long-lived dark state [21].

In future experiments, we recommend to activate the UV laser when the detection rate falls below a mean count rate derived from multiple previous localizations, following the approach of Balzarotti *et al.* [22]. This could minimize the probability of double activation during short-term blinking of the dye on time scales $< 10\,\text{ms}$. Further, we recommend to excite the fluorophores with an intensity below their saturation value. Since higher emission rates can cause longer or more frequent short-term blinking, the currently implemented measurement and analysis routine could become less reliable in discriminating events with two activated emitters.

Since the 10 nm separated labeling points were resolved with a precision of 1 to 2 nm, it is very likely to resolve also smaller structures. Therefore, similar DNA origamis with projection of the molecular separation along the axial direction of 6 and 3 nm have been ordered and will be used in further experiments. So far, molecular distances on this length scale were verified with Förster resonance energy transfer (FRET) [5, 59, 60]. Future 4Pi-MINFLUX experiments might shed light on the impact that photo-physical interactions of multiple fluorophores can have on the achieved resolutions.

6 Conclusion and Outlook

In this thesis, the MINFLUX localization concept was united with a 4Pi-optics illumination scheme. By using two opposing objective lenses, it was possible to create a focused interference pattern, of which the minimum position could be translated along the optical axis. We implemented a 1D MINFLUX localization with three exposures of differently targeted minima positions by changing the relative optical path length of the interfering beams. This was achieved using microsecond fast electro-optic phase modulators.

Simulations of the illumination PSF revealed that the 4Pi-MINFLUX outperforms state-of-the-art, single objective lens 2D or 3D MINFLUX microscopes in terms of the curvature in the intensity minimum. Not only a smaller separation of the first side maxima ($\sim 30\,\%$), but also a five times higher intensity of the maximum per illumination unit is achieved with 4Pi-optics. This leads to a 40 % decrease in the number of required photons for a localization, when similar SBR and localization uncertainties are considered. We expect no other focused illumination scheme to create a stronger curvature in the intensity minimum.

In axial localization measurements of static single molecules, we could set the uncertainty defining L-value routinely down to 15 nm, and in individually optimized cases even down to 6 nm. 2D- and 3D MINFLUX operate routinely at respectively 3 and 8 times larger L-value. These higher L-values highlight that in 4Pi-MINFLUX a higher SBR and consequently cleaner interference was achieved. Even here, background photon counts stemmed to a greater amount ($\sim$3) from the emitter excited by the residual intensity in the minimum than from luminescent background photons. Due to the low L-value, 4Pi-MINFLUX is the first experimental demonstration that molecular localization precision with only several tens of detected photons is possible.

The resolution power of the 4Pi-MINFLUX scheme was demonstrated with DNA origami nanorulers. The microscope could reliably render the individual positions of molecular emitters separated by 10 nm along the axial direction and achieved an average localization precision of 1.6 nm.

Outlook

Optical aberrations The quality of the destructive interference pattern is central to successful MINFLUX measurements. More than any other illumination scheme, 4Pi-optics is especially susceptible to optical aberrations, which arise due to the asymmetric illumination condition of both beams. Since the sample is immobilized on the surface of only one coverslip, one beam travels only through immersion medium, while the other beam travels through both immersion- and mounting medium. When moving away from mounting media with matching refractive index, such aberrations increase, and consequently the advantage over single objective lens MINFLUX decreases.
In future 4Pi-MINFLUX implementations, adaptive optics should be considered to minimize differences of the wave front of both interfering beams. This approach has previously been shown to be applicable to coherent double objective lens systems to reduce limitations arising from both optical elements and samples themselves [61, 62].

Buffer Although the refractive-index-matched TDE-buffer allowed for a constant emission rate of the studied single molecules, it deviates strongly from the natural aqueous environment of biological samples. In the case of imaging applications using stochastically blinking fluorophores, which require the diffusion of blinking-regulating additives, a pure TDE-buffer is not suitable due to its higher viscosity. This equally applies to tracking applications, during which the movement of the emitter itself is studied.
Thus, holding on to an index matched buffer limits the range of possible applications of 4Pi-MINFLUX. Hence, in future work it might be beneficial to use glycerol objective lenses to reduce refractive index mismatches of aqueous buffers [40].

4Pi cavity Limitations that especially affect the localization precision in repeated MINFLUX measurements are vibrations and thermal drift. Both lead to undesired changes of the intensity minimum position when their effect on the two 4Pi cavity beam path lengths differs. Since the 4Pi cavity was constructed relatively large compared to a triangular 4Pi cavity with intrinsic beam alignment designed by Curdt *et al.*, drift-free data could not be recorded in long-term measurements when relying solely on passive cavity stabilization [42].
A possible improvement to achieve active stabilization of the optical cavity path length could be to introduce a distinguishable reference beam illuminated along the same path as the excitation beam. Equally to the excitation beam, the reference beam should be split at the start of the 4Pi cavity into two paths. The beams that are backreflected at the boundary of the sample coverslip should then be interfered

at a detector just outside of the 4Pi cavity. Changes of the interference signal would provide information about the drift of the optical path length of the 4Pi cavity. Although, these measurement would only provide an approximation of the actual changes experienced by the illumination beam, such information could allow for partial drift correction. Still, such a system would increase the operation complexity and it would eventually be better to reconstruct the microscope with a smaller cavity. Additionally, this would allow to eliminate mechanically vibrating elements. Since we have conceptually proven that the PSF can be successfully controlled for MINFLUX localizations, one can think of implementing the electro-optical controlling elements on an optical integrated circuit to further reduce the size of the 4Pi cavity [63].

Field of view Since the localization measurement can only be unambiguously performed up to a length scale of half of the excitation wavelength in the medium, the size of resolvable structures and the tracking ranges are limited [64]. For tracking, the sample stage can be repositioned, allowing a larger tracking range, yet with a time resolution limited by the sample stage (»1 ms).

Multidimensional localization The current implementation of 4Pi-MINFLUX is constrained to measurements along the axial direction. Thus, the studied structure or movement must be oriented accordingly. This requirement can nicely be met with DNA origami nanopillars as their structures and modifications are controlled by design, which allows specific binding of the nanopillar baseplate to the surface of the coverslip. Additionally, single emitter distances and modification sites along the nanopillar axis can be chosen with single nanometer precision [54]. Intrinsic alignment along the localization dimension allows improved measurement of distances or movements, either by a factor of two faster acquisition or by consuming only half the photons compared to lateral localization schemes. In the latter, the orientation in the lateral plane cannot be constrained so easily to a single dimension. Since multiple repetitive localizations were achieved for a single emission burst of the dye, we can expect that also 3D localizations are not limited by the number of detected photons per emission burst. With the expansion towards 3D localization conceptually presented in this thesis, 3D 4Pi-MINFLUX holds promise to achieve the highest precision measurements of small structures and molecular distances in 3D in the field of fluorescence nanoscopy.

In conclusion, **4Pi-MINFLUX** can be an excellent tool to image small structures, follow dynamics and measure distances and their changes in the sub-nanometer regime. While previously information at these length scales could exclusively be accessed by FRET, 4Pi-MINFLUX now allows measurements in this regime with

high precision and minimal photon fluxes. In this work, a localization precision down to the upper sub-nanometer range was established. We encourage further research to explore the suggested improvements and resolve the current limitations of the 4Pi-MINFLUX technology. We hope this might pave the way towards routine measurements of complex biological samples with Ångström precision in three dimensions.

A Appendix

A.1 MINFLUX localization

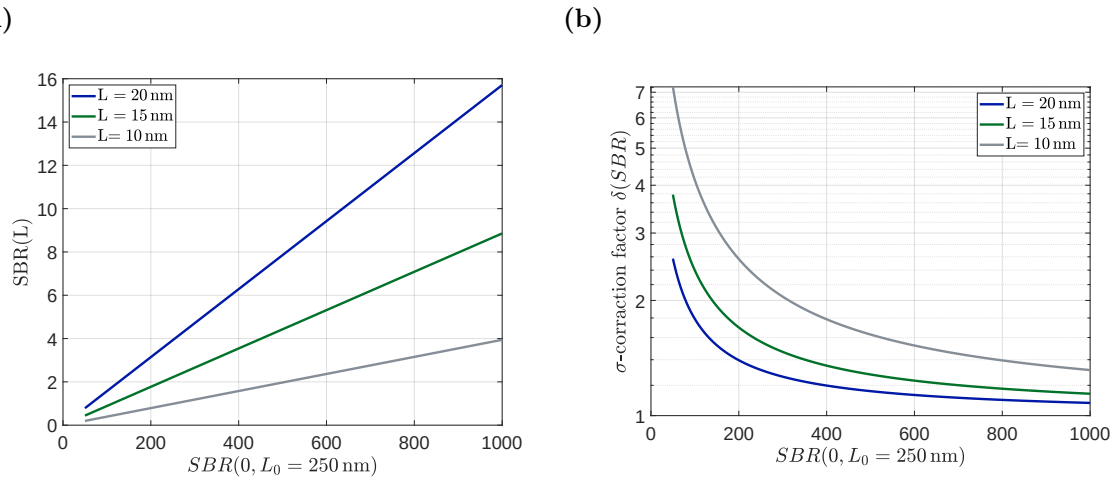

Figure A.1: (a) Calculation of the signal-background-ratio (SBR) at an L-value (see legend) for varying reference $SBR(0, L_0)$-values (equation 2.33), which were evaluated at 250 nm (separation of the first side maxima as observed in the experiment). (b) SBR-correction factor (product of both square root terms in equation 2.26) for varying reference SBR-values, which were evaluated at $L_0 = 250\,\mathrm{nm}$.

A.2 4Pi PSF calculation

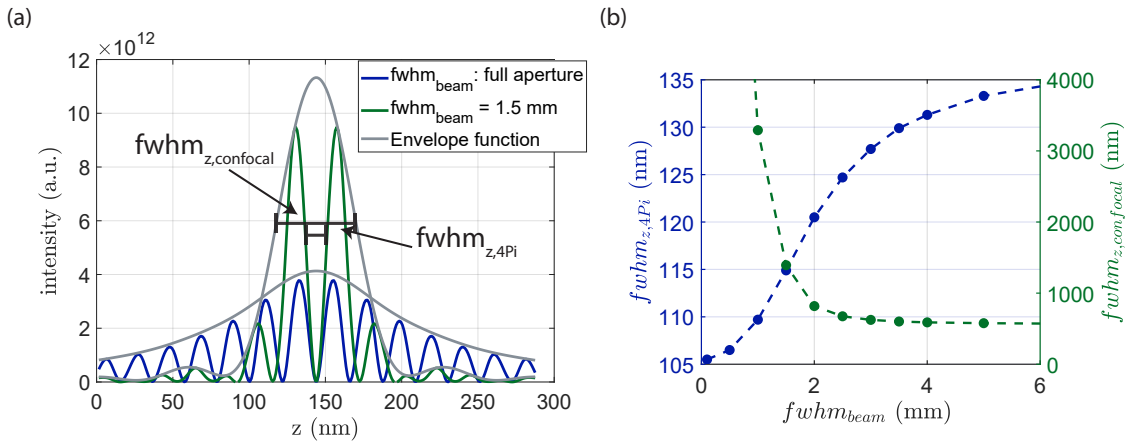

Figure A.2: Beam size dependent parameter of the axial 4Pi PSF. (a) Destructive interference axial illumination profile along the optical axis for two different beam sizes. $fwhm_{beam}$ denotes the $fwhm$ of a Gaussian beam in the back focal plane of an objective. $fwhm_{z,4Pi}$ denotes the $fwhm$-value of the minimum. $fwhm_{z,confocal}$ denotes the $fwhm$-value of the confocal envelope function, which was calculated from a non interfering 4Pi illumination scheme. (b) Beam size dependent values of $fwhm_{z,4Pi}$ and $fwhm_{z,confocal}$. An optimal operation range balancing the illuminated volume ($fwhm_{z,confocal}$) and separation of the first size maxima ($fwhm_{z,4Pi}$) was found between beam sizes of 2.5 to 3 mm.

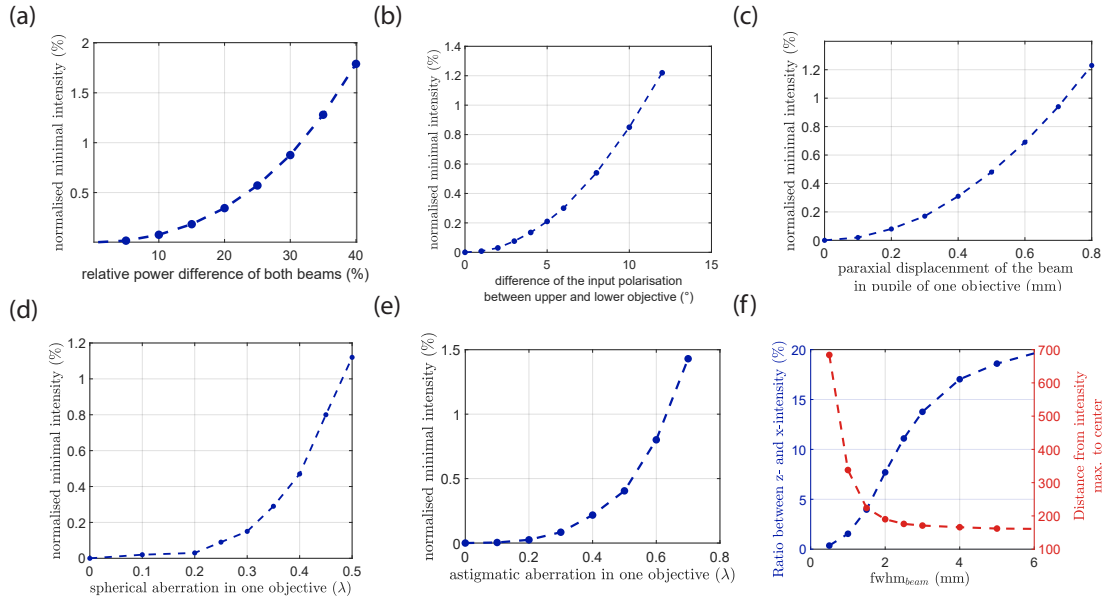

Figure A.3: 4Pi PSF Aberrations Each aberration ((a) to (e)) was simulated until the intensity in the minimum reaches a value of 1 % of the maximum. (f) Properties of the illumination intensity in lateral plane arising from z-component of the electric field vector under modification of the beam size. The left y-axis denotes the ratio of the intensities arising from the z-component in the later plane and global maximum of the x-component. The right y-axis denotes the distance of the lateral maximum to the geometric focus point. Calculations were performed for a NA 1.44 oil objective lens (λ =640 nm) and linear (x) polarized illumination.

A.3 Calculation of the optimal beam position for normal vector system for titled 4Pi PSF

In the following, it will be derived, at which paraxial distance h (distance of the beam and the optical axis in the bfp of the objective lens) the three beams have to be positioned to achieve orthogonal tilted PSF for 3D localization. The procedure to find the ideal beam setting is at first to determine the arrangement of the beams (distance with respect to the optical axis) in the back focal plane of both objectives using non focussed beams, i.e. widefield illumination. Here, the angle with respect to the optical axis is the same for all beams. We assume that the following vectors are the directions of the three tilted PSF and the optical axis

$$\vec{v}_1 = \begin{pmatrix} 1 \\ 0 \\ 0 \end{pmatrix}, \quad \vec{v}_2 = \begin{pmatrix} 0 \\ 1 \\ 0 \end{pmatrix}, \quad \vec{v}_3 = \begin{pmatrix} 0 \\ 0 \\ 1 \end{pmatrix} \quad and \quad \vec{v}_{opt} = \frac{1}{\sqrt{3}} \begin{pmatrix} 1 \\ 1 \\ 1 \end{pmatrix}. \tag{A.1}$$

It by definition all vectors $\vec{v}_1, \vec{v}_2, \vec{v}_3$ are rectangular to each other and with the scalar product between $\vec{v}_i \cdot \vec{v}_{opt} = |\vec{v}_i|\,|\vec{v}_{opt}| \cos(\alpha)$ for $i = [1, 2, 3]$ the angle towards the optical axis α is calculated to be $\alpha = 54.7\,°$.
Using Abbe sine condition, which sets a relation between the paraxial distance h of the beam and the angle of incidence α of a light ray towards the optical axis on the sample side. This is a relation that must be fulfilled by every spherical aberration corrected objective lenses and is defined by:

$$h = fn \sin(\alpha) \tag{A.2}$$

With n being the refractive index of the immersion medium, f the focal length of the objective, which is calculated with the focal length of the tubelens $f_{tubel.}$ and the magnification factor of objective and tubelense Mag as: $f = f_{tubel.}/Mag$. With the values used later in the experiment $f_{tubel.} = 200\,\text{mm}$, $Mag = 100$ and $n = 1.518$ the paraxial distance of the incoming beam is calculated to be $h = 2.48\,\text{mm}$. Note that these findings are only valid for a non-focused beam and thus, is the numerically correct value for beams focused in the back focal plane.

A.4 Detailed mechanical design of the 4Pi unit

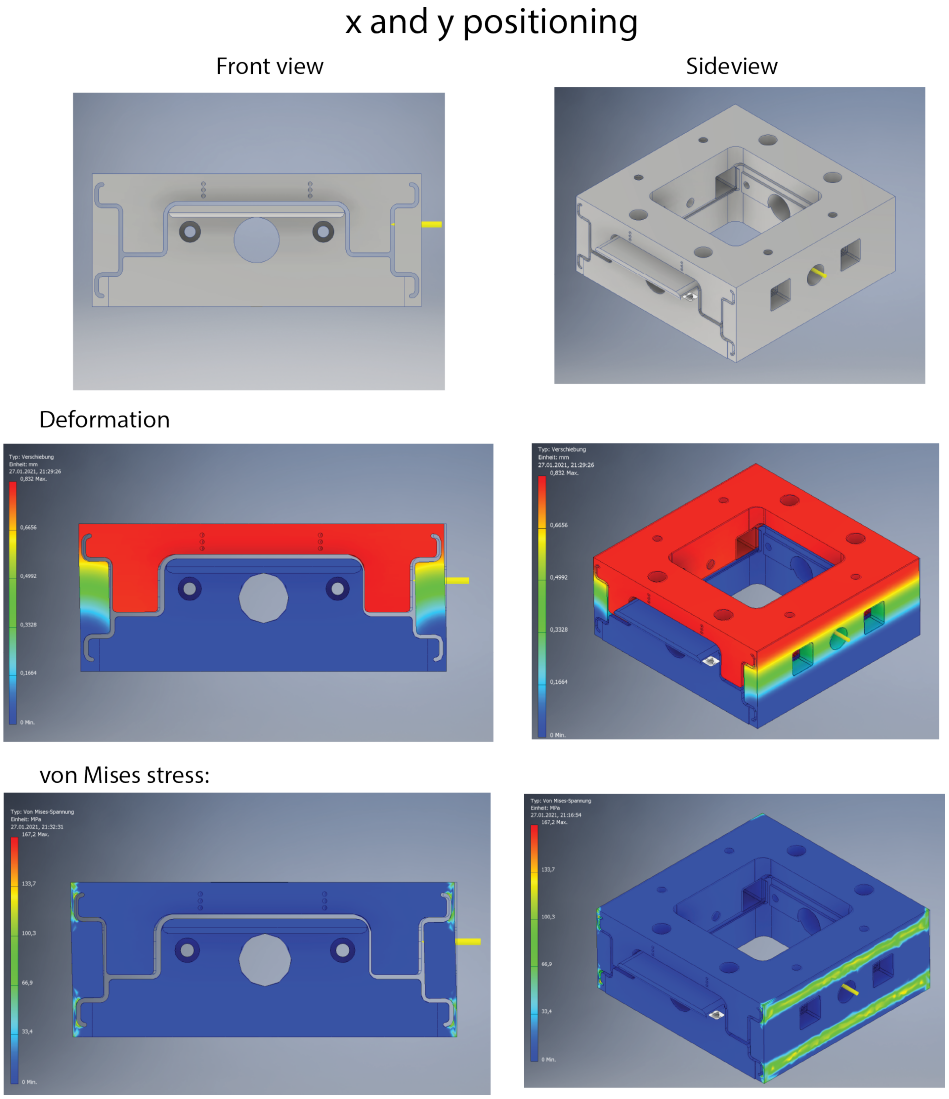

Figure A.4: CAD-sketch and mechanical properties of a single positioning element used for x-y-positioning of the lower objective lens. The x-y-positioning was achieved by two identical positioning elements, which are 90 ° twisted to each other and stacked on top of each other. The top row shows the shape of the positioning element without force effect. The middle show shows the deformation of the positioning element (maximal 0.8 mm) when a force of 300 N is applied to the right side. The push/ pull force was generated by the piezo motor and indicated by a yellow arrow pointing to the left side of the figure. The lower row shows the von Mises stress in the positioning element when the same force.

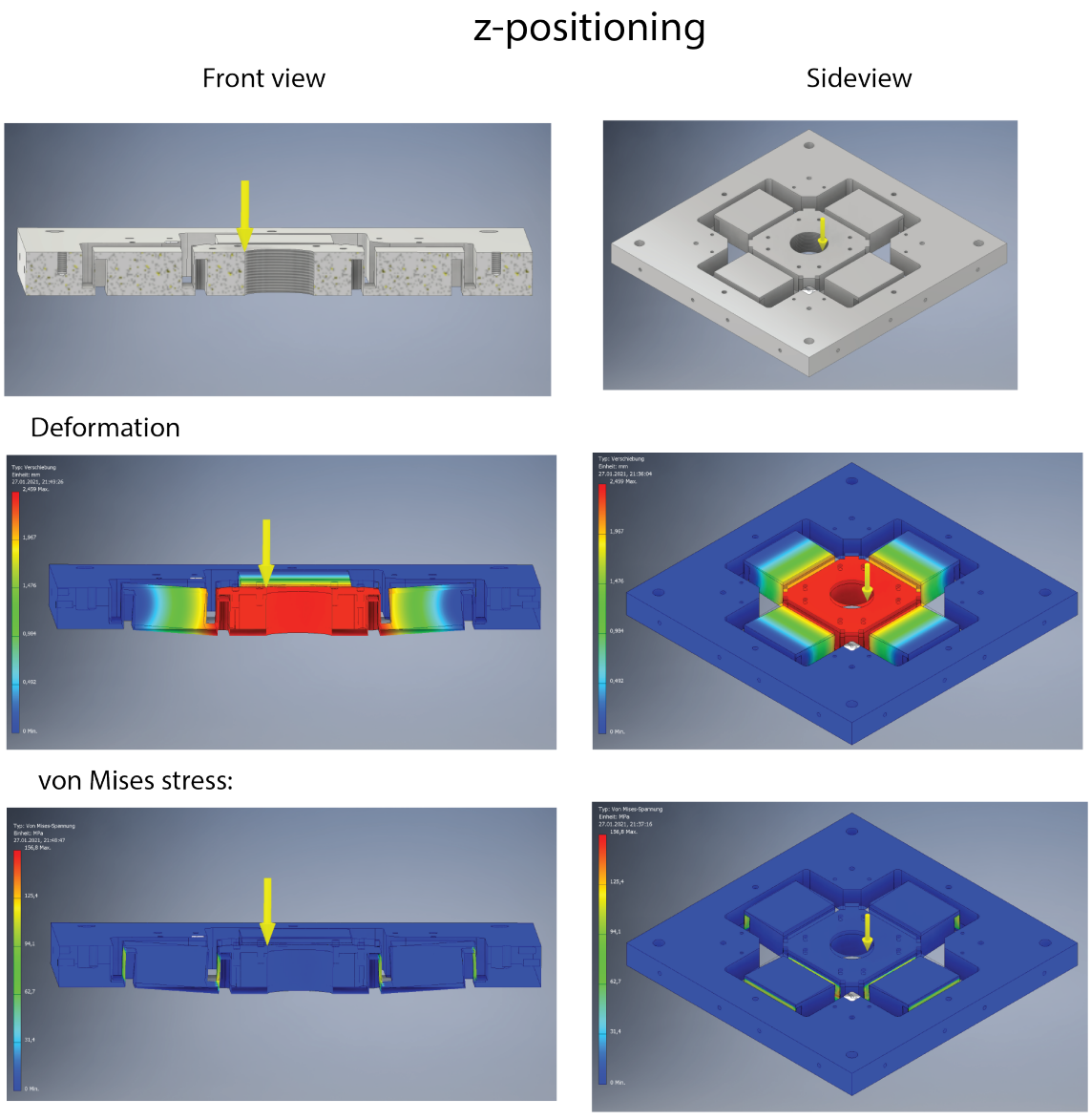

Figure A.5: CAD-sketch and mechanical properties of the positioning element used for z-positioning of the upper objective lens. The top row shows the shape of the z-positioning element without force effect. The middle show shows the deformation of the positioning element (maximal 2.5 mm) when a force of 300 N is applied to the right side. The push/ pull force was generated by the piezo motor and indicated by a yellow arrow pointing to the bottom side of the figure. The lower row shows the von Mises stress in the positioning element when the same force is applied.

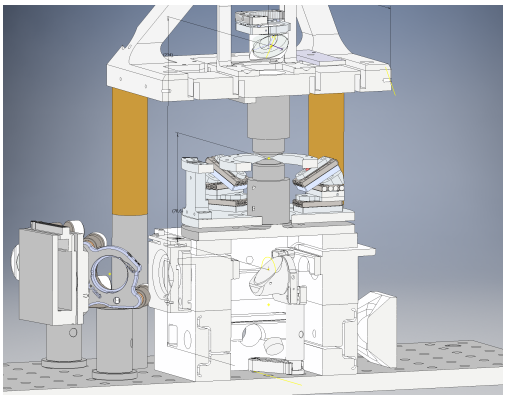

Figure A.6: Inside view of the mechanical construction of the objective mounting frame.

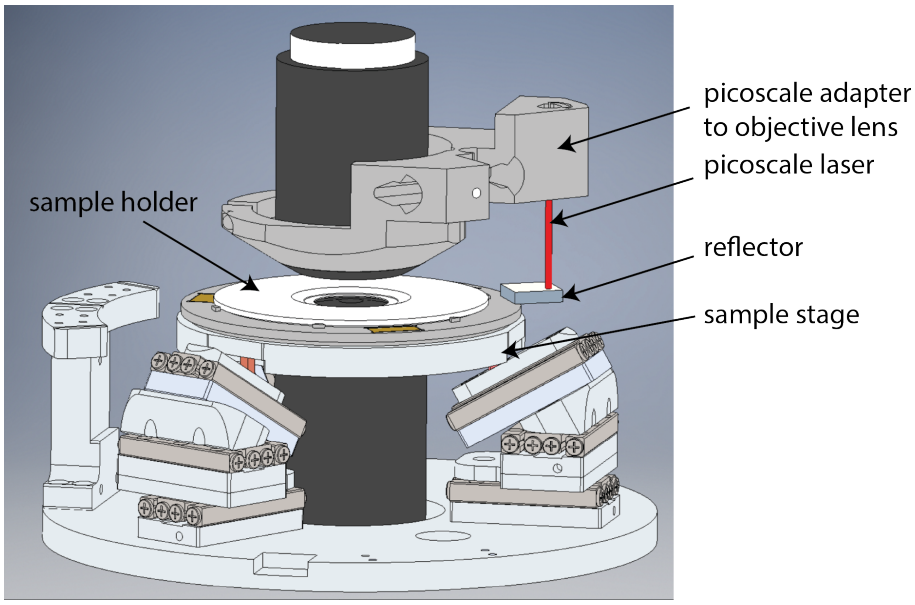

Figure A.7: Commercial displacement measurement device (fiber based interferometer, Picoscale, SmarAct GmbH, Oldenburg, Germany). The Picoscale can measure distance changes with nanometer precision. We used it in our measurement, to crosscheck the translation of the sample stage. Therefore, we first mounted the Picoscale in an adatper which is fixated to the upper objective. A mirror was glued to the sample stage and served as a retroreflector for the picoscale laser. Thus, the Picoscale does not measure the distance changes of the sample position in the close vicinity to the optical focus of the objective lenses but rather from a position roughly 3 cm away from it. We assume that the such a displaced measurement does not induced a large bias when fast movements with measurements times below one minute are performed. However, long-term drift might be different for the sample position in the focus compared to the position of the mirror. The adapter was designed by Michael Remmel.

A.5 MINFLUX tracking and tracing measurements

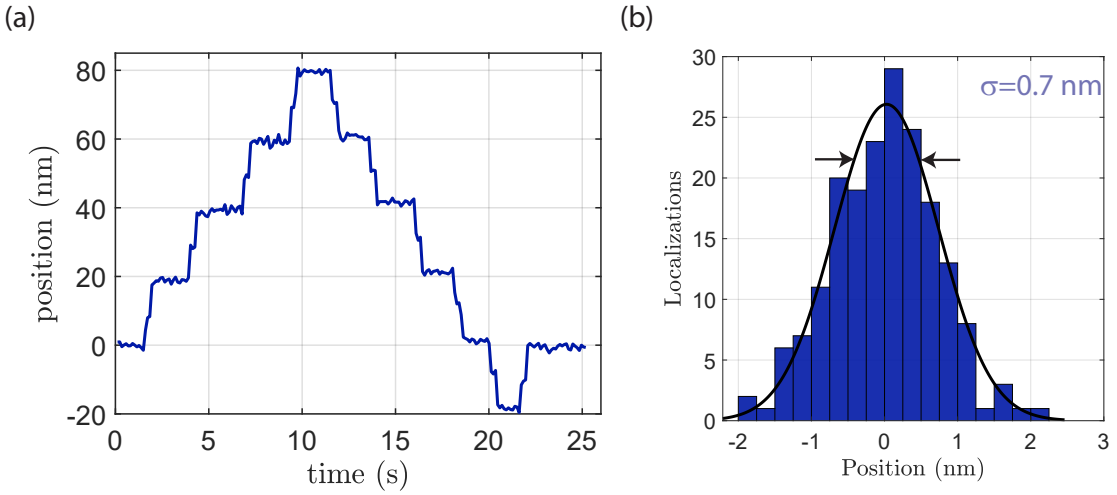

Figure A.8: MINFLUX tracking of a single emitter (Atto 647N) during step wise sample stage movement with an amplitude of 20 nm The measurement parameter are listed in table A.1. (a) Localization trajectory with multiple bidirectional, manually performed sample stage steps. The position after an single step are clearly resolvable from each other and the mean distance of consecutive position levels is (19.6 ± 0.8) nm. On average, 450 photons contributed to a single MINFLUX localization. (b) Histogram of 185 localizations from the localization trajectory in (a). Only the localizations, which were attributed to a level of a step are considered and subtracted by the mean position value of the position level. A Gaussian fit to the histogram plot reveals that the localization uncertainty on average lies below 1 nm. The pure statistical photon limit for the on average 450 photons measured in each localization was 0.3 nm. Bin size: 0.25 nm

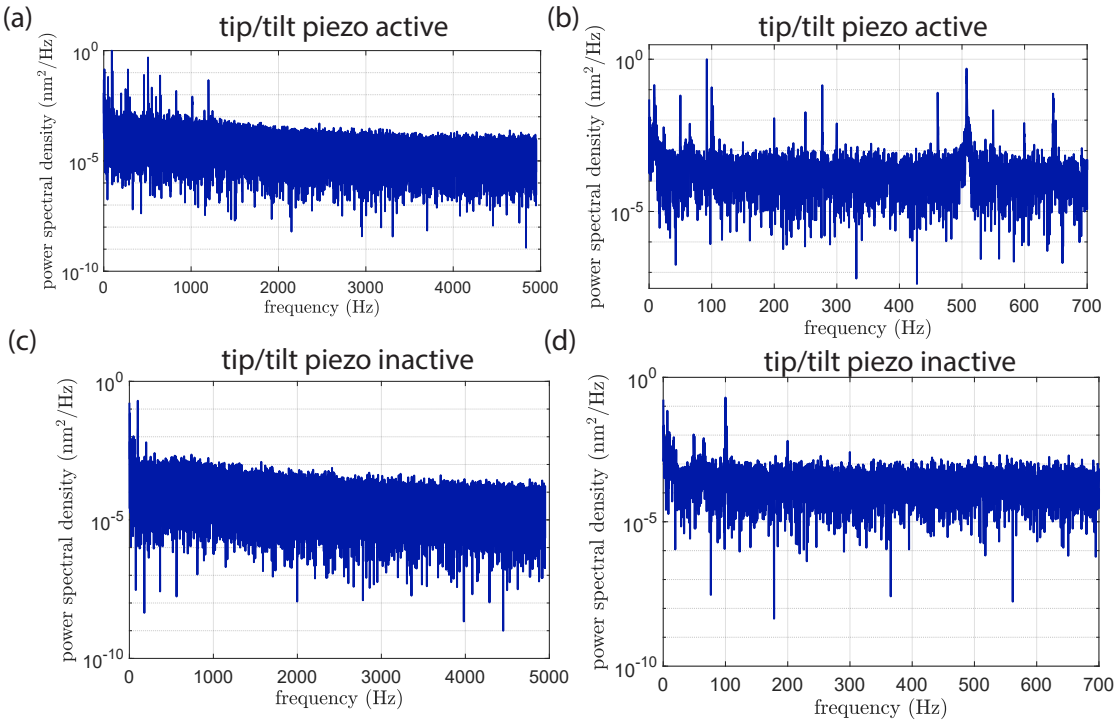

Figure A.9: Power spectral density (PSD) of MINFLUX tracking measurements at a GNP with 10 kHz sampling rate and different settings of the tip/tilt piezo (L =20 nm) (a) PSD measured with an active tip/tilt piezo. Active denotes that the piezo element was operation in the same way as used for scanning. (b) Zoom in of the spectrum in (a) reveals that multiple frequencies are present in the spectrum. (c) PSD measured with an inactive tip/tilt piezo. Inactive denotes that the feedback loop for the piezo positioning was slowed down. (d) Zoom in of the spectrum in (a) reveals that the tip/tilt piezo was responsible for the most of the peaks in the spectrum (92 and 512 Hz as well as higher harmonics of these two frequencies).

Parameters of MINFLUX tracking	Sinosoidal oscillation (figure 4.2)	Step-Movement (figure A.8)
Fluorophore	Cy3b	Atto 647N
L (nm)	20	20
Exposure time (setuptime)	500 µs (3.5 µs)	5 ms (3 µs)
position correction time	0.5 µs	100 ms
Repeats of last MINFLUX iteration	2000	220
Fluorescence count rate (kHz)	17	30
Average photon per localization	26	450
SBR(L)	8	5.1

Table A.1: Measurement parameters of MINFLUX tracking experiments

Parameters of MINFLUX tracing with $L = 15$ nm			
Sampling rate (kHz)	1	5.5	10
Exposure time T_{dwell} (µs)	a) 333 b) 1650 c)16500	a) 60 b) 330 c) 3300	33
sum of setup (T_{setup}) and position calculation time ($T_{poscalc}$)	2	2	2
Repeats of last MINFLUX iteration	a) 5000 b) 1000 c) 500	a) 2000 b) 500 c) 50	10000
laser power (λ =640 nm) in the bfp of objective 1 (µW)	10	75	260

Table A.2: Measurement parameters of MINFLUX tracing experiments with Atto 647N Results were presented in figure 4.3 and 4.5.

Parameter of MINFLUX:	MINFLUX tracing from (figure 4.3(a))	MINFLUX tracing and tracing from (figure 4.3(b) to (d))
L (nm)	15	6
Exposure dwell time T_{dwell} (µs)	330	330
position correction time (µs)	3.5	3.5
Repeats of last MINFLUX iteration	3000	500
Fluorescence count rate (kHz)	30	20

Table A.3: Measurement parameters of MINFLUX experiments with Cy3b from section 4.4

(a) Without High pass filter

(b) With 5 Hz high pass filter

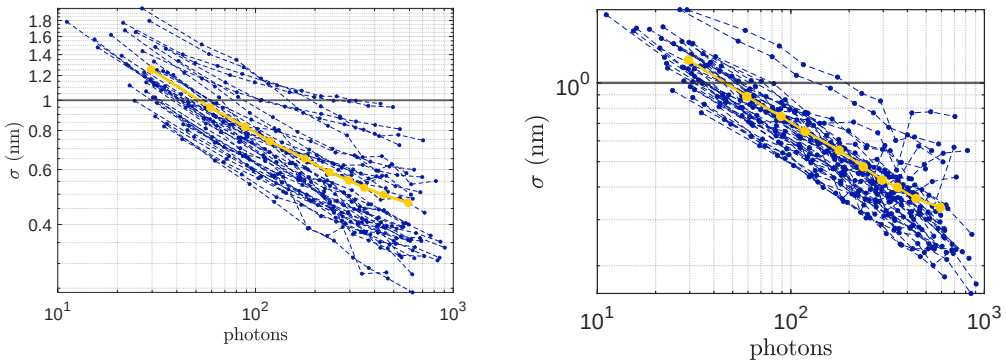

Figure A.10: MINFLUX tracing experiment results with Cy3b and with L=15 nm. Both plots show the individual results for a single molecule in blue and the average value in yellow. (b) was analyzed with an additional 5 Hz high pass filter. Here, the localization uncertainty in the high photon count regime could be reduced.

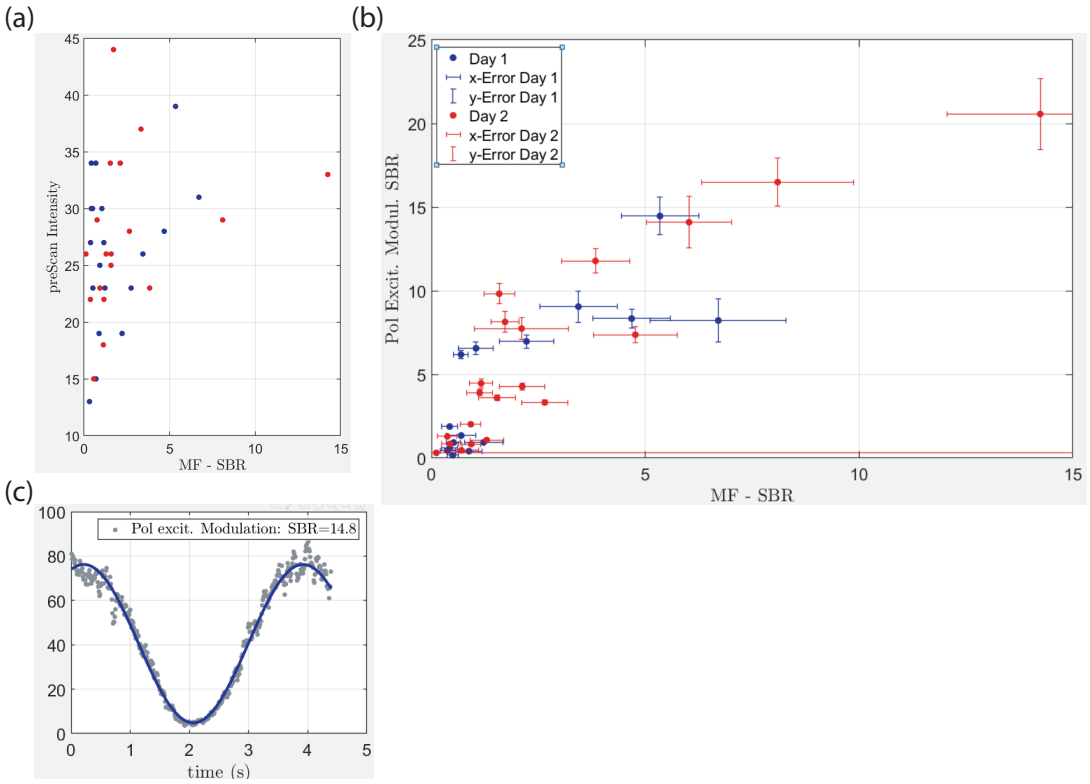

Figure A.11: Correlative measurements of the emitter brightness, fluorescence extinction by polarization modulation and the SBR in MINFLUX tracing (L=15 nm) measurements. (a) Emitter brightness in the x-y-scan of the pre-localization step plotted versus the SBR of MINFLUX tracing. A high SBR-value is only achieved for emitter which have shown a high brightness in the pre-scan. (b) Detected photon count trace at simultaneous modulation of the excitation polarization by rotation of a $\lambda/2$ wave plate. The SBR was defined by ratio of the maximum to minimum intensity, which both were extracted from data fitting with a sinusoidal function. (c) SBR of the polarization modulated excitation time trace plotted against the SBR measured in MINFLUX tracing. A positive correlation between both measurement parameter is visible. This leads to the conclusion that MINFLUX measurements with a high SBR-value were only possible if the molecule exhibited a strong excitation polarization dependent brightness, i.e. has a fix transition dipole moment. The measurement has been performed at the same sample at two different measurement days (blue and red).

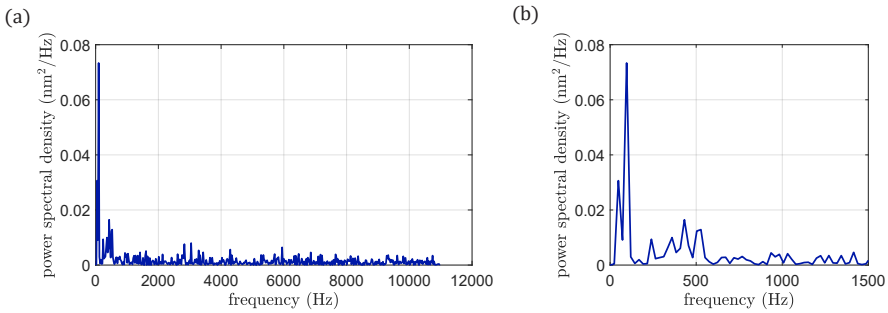

Figure A.12: Power spectral density of the MINFLUX tracing measurement shown in figure 4.7 (a) using the modified position estimator and binning factor of six.(a) shows the full spectrum. (b) Zoom in of the spectrum shown in (a). A peak in the low frequency range (<100) as well as around 500 Hz is visible. Both peak could be attributed to the vibration of the tip/tilt mirror (see section 4.3.2).

B List of Figures

C List of Tables

D Bibliography

1. Cheng, Y. Single-particle cryo-EM—How did it get here and where will it go. *Science* **361,** 876–880 (2018).
2. Danev, R., Yanagisawa, H. & Kikkawa, M. Cryo-Electron Microscopy Methodology: Current Aspects and Future Directions. *Trends in Biochemical Sciences* **44,** 837–848 (2019).
3. Pawley, J. B. *Handbook of biological confocal microscopy* 3. ed. ISBN: 9780387259215 (Springer, New York, NY, 2006).
4. Jradi, F. M. & Lavis, L. D. Chemistry of Photosensitive Fluorophores for Single-Molecule Localization Microscopy. *ACS Chemical Biology* **14,** 1077–1090 (2019).
5. Ishikawa Ankerhold, H. C., Ankerhold, R. & Drummen, G. P. Advanced fluorescence microscopy techniques–FRAP, FLIP, FLAP, FRET and FLIM. *Molecules (Basel, Switzerland)* **17** (2012).
6. Abbe, E. Beiträge zur Theorie des Mikroskops und der mikroskopischen Wahrnehmung. *Archiv für Mikroskopische Anatomie* **9,** 413–468 (1873).
7. Rayleigh, J. XV. On the theory of optical images, with special reference to the microscope. *The London, Edinburgh, and Dublin Philosophical Magazine and Journal of Science* **42,** 167–195 (1896).
8. Hell, S. W. Double-scanning confocal microscope. *European Patent,* p. 0491289 (1992).
9. Huang, B., Wang, W., Bates, M. & Zhuang, X. Three-Dimensional Super-Resolution Imaging by Stochastic Optical Reconstruction Microscopy. *Science* **319,** 810–813 (2008).
10. Pavani, S. R. P. *et al.* Three-dimensional, single-molecule fluorescence imaging beyond the diffraction limit by using a double-helix point spread function. *Proceedings of the National Academy of Sciences* **106,** 2995–2999 (2009).
11. Liu, W. *et al.* Breaking the Axial Diffraction Limit: A Guide to Axial Super–Resolution Fluorescence Microscopy. *Laser & Photonics Reviews* **12** (2018).

12. Hell, S. W. & Wichmann, J. Breaking the diffraction resolution limit by stimulated emission: stimulated-emission-depletion fluorescence microscopy. *Optics Letters* **19,** 780–782 (1994).

13. Klar, T. A., Jakobs, S., Dyba, M., Egner, A. & Hell, S. W. Fluorescence microscopy with diffraction resolution barrier broken by stimulated emission. *Proceedings of the National Academy of Sciences of the United States of America* **97,** 8206–8210 (2000).

14. Betzig, E. *et al.* Imaging intracellular fluorescent proteins at nanometer resolution. *Science (New York, N.Y.)* **313,** 1642–1645 (2006).

15. Rust, M. J., Bates, M. & Zhuang, X. Sub-diffraction-limit imaging by stochastic optical reconstruction microscopy (STORM). *Nature methods* **3,** 793–795 (2006).

16. D Este, E., Kamin, D., Göttfert, F., El-Hady, A. & Hell, S. W. STED Nanoscopy Reveals the Ubiquity of Subcortical Cytoskeleton Periodicity in Living Neurons. *Cell Reports* **10,** 1246–1251 (2015).

17. Schmidt, R. *et al.* Mitochondrial Cristae Revealed with Focused Light. *Nano letters* **9,** 2508–2510 (2009).

18. Shtengel, G. *et al.* Interferometric fluorescent super-resolution microscopy resolves 3D cellular ultrastructure. *Proceedings of the National Academy of Sciences of the United States of America* **106,** 3125–3130 (2009).

19. Aquino, D. *et al.* Two-color nanoscopy of three-dimensional volumes by 4Pi detection of stochastically switched fluorophores. *Nature Methods* **8,** 353–359 (2011).

20. Huang, F. *et al.* Ultra-High Resolution 3D Imaging of Whole Cells. *Cell* **166,** 1028–1040 (2016).

21. Dempsey, G. T., Vaughan, J. C., Chen, K. H., Bates, M. & Zhuang, X. Evaluation of fluorophores for optimal performance in localization-based super-resolution imaging. *Nature Methods* **8,** 1027–1036 (2011).

22. Balzarotti, F. *et al.* Nanometer resolution imaging and tracking of fluorescent molecules with minimal photon fluxes. *Science* **355,** 606–612 (2017).

23. Xu, K., Babcock, H. P. & Zhuang, X. Dual-objective STORM reveals three-dimensional filament organization in the actin cytoskeleton. *Nature Methods* **9,** 185–188 (2012).

24. Gwosch, K. C. *et al.* MINFLUX nanoscopy delivers 3D multicolor nanometer resolution in cells. *Nature methods* **17,** 217–224 (2020).

25. Keller, J., Schönle, A. & Hell, S. W. Efficient fluorescence inhibition patterns for RESOLFT microscopy. *Optics Express* **15,** 3361–3371 (2007).

26. Masullo, L. A. *et al.* Pulsed Interleaved MINFLUX. *Nano letters* (2020).

27. Cnossen, J. *et al.* Localization microscopy at doubled precision with patterned illumination. *Nature Methods* **17,** 59–63 (2020).

28. Gu, L. *et al.* Molecular resolution imaging by repetitive optical selective exposure. *Nature Methods* **16,** 1114–1118 (2019).

29. Lakowicz, J. R. *Principles of Fluorescence Spectroscopy* ISBN: 978-0-387-31278-1 (2006).

30. Richards, B. & Wolf, E. Electromagnetic diffraction in optical systems, II. Structure of the image field in an aplanatic system. *Proceedings of the Royal Society of London. Series A. Mathematical and Physical Sciences* **253,** 358–379 (1959).

31. Gustafsson, M. G. L. Surpassing the lateral resolution limit by a factor of two using structured illumination microscopy. *Journal of microscopy* **198,** 82–87 (2000).

32. Mueller, T., Schumann, C. & Kraegeloh, A. STED Microscopy and Its Applications: New Insights Into Cellular Processes on the Nanoscale. *Chemphyschem : a European journal of chemical physics and physical chemistry* **13** (2012).

33. Nagorni, M. & Hell, S. W. Coherent use of opposing lenses for axial resolution increase in fluorescence microscopy. I. Comparative study of concepts. *Journal of the Optical Society of America. A, Optics, image science, and vision* **18,** 36–48 (2001).

34. Bailey, B., Farkas, D. L., Taylor, D. L. & Lanni, F. Enhancement of axial resolution in fluorescence microscopy by standing-wave excitation. *Nature* **366,** 44–48 (1993).

35. Gustafsson, M. G. L., Agard, D. A. & Sedat, J. W. *Sevenfold improvement of axial resolution in 3D wide-field microscopy using two objective lenses* in *Three-Dimensional Microscopy: Image Acquisition and Processing II* (eds Wilson, T. & Cogswell, C. J.) (SPIE, 1995), 147–156.

36. Gustafsson, M. G., Agard, D. A. & Sedat, J. W. I5M: 3D widefield light microscopy with better than 100 nm axial resolution. *Journal of microscopy* **195,** 10–16 (1999).

37. Wang, G., Hauver, J., Thomas, Z., Darst, S. A. & Pertsinidis, A. Single-Molecule Real-Time 3D Imaging of the Transcription Cycle by Modulation Interferometry. *Cell* **167,** 1839–1852.e21 (2016).

38. Schmidt, R. *et al.* Spherical nanosized focal spot unravels the interior of cells. *Nature methods* **5,** 539–544 (2008).

39. Backlund, M. P., Shechtman, Y. & Walsworth, R. L. Fundamental Precision Bounds for Three-Dimensional Optical Localization Microscopy With Poisson Statistics. *Physical review letters* **121** (2018).

40. Schmidt, N. C., Kahms, M., Hüve, J. & Klingauf, J. Intrinsic refractive index matched 3D dSTORM with two objectives: Comparison of detection techniques. *Scientific Reports* **8,** 1–12 (2018).

41. Hell, S. W. & Stelzer, E. H. K. Properties of a 4Pi confocal fluorescence microscope. *JOSA A* **9,** 2159–2166 (1992).

42. Curdt, F. *et al.* isoSTED nanoscopy with intrinsic beam alignment. *Optics Express* **23,** 30891–30903 (2015).

43. Böhm, U., Hell, S. W. & Schmidt, R. 4Pi-RESOLFT nanoscopy. *Nature communications* **7,** 10504 (2016).

44. Schmidt, R., Engelhardt, J. & Lang, M. 4Pi Microscopy. **950,** 27–41 (2013).

45. Curdt, F. *4Pi Nanoscopy parallelized by linescanning* PhD thesis (Universität Heidelberg, 2013). `https://doi.org/10.11588/heidok.00014362`.

46. Hell, S. W., Reiner, G., Cremer, C. & STELZER, E. H. K. Aberrations in confocal fluorescence microscopy induced by mismatches in refractive index. *Journal of microscopy* **169,** 391–405 (1993).

47. Staudt, T., Lang, M. C., Medda, R., Engelhardt, J. & Hell, S. W. 2,2'-thiodiethanol: a new water soluble mounting medium for high resolution optical microscopy. *Microscopy research and technique* **70,** 1–9 (2007).

48. van de Linde, S. *et al.* Direct stochastic optical reconstruction microscopy with standard fluorescent probes. *Nature Protocols* **6,** 991–1009 (2011).

49. Wurm, C. A., Neumann, D., Schmidt, R., Egner, A. & Jakobs, S. in *Live Cell Imaging* (ed Papkovsky, D. B.) 185–199 (Humana Press, Totowa, NJ, 2010). ISBN: 978-1-60761-404-3.

50. Egner, A., Schrader, M. & Hell, S. W. Refractive index mismatch induced intensity and phase variations in fluorescence confocal, multiphoton and 4Pi-microscopy. *Optics Communications* **153,** 211–217 (1998).

51. Eilers, Y., Ta, H., Gwosch, K. C., Balzarotti, F. & Hell, S. W. MINFLUX monitors rapid molecular jumps with superior spatiotemporal resolution. *Proceedings of the National Academy of Sciences of the United States of America* **115,** 6117–6122 (2018).

52. Vogelsang, J. *et al.* A reducing and oxidizing system minimizes photobleaching and blinking of fluorescent dyes. *Angewandte Chemie (International ed. in English)* **47,** 5465–5469 (2008).

53. Cooper, M. *et al.* Cy3B™: Improving the Performance of Cyanine Dyes. *Journal of Fluorescence* **14,** 145–150 (2004).

54. Scheckenbach, M., Bauer, J., Zähringer, J., Selbach, F. & Tinnefeld, P. DNA origami nanorulers and emerging reference structures. *APL Materials* **8,** 110902 (2020).

55. Jungmann, R. *et al.* Single-Molecule Kinetics and Super-Resolution Microscopy by Fluorescence Imaging of Transient Binding on DNA Origami. *Nano letters* **10,** 4756–4761 (2010).

56. Göttfert, F. *et al.* Strong signal increase in STED fluorescence microscopy by imaging regions of subdiffraction extent. *Proceedings of the National Academy of Sciences* **114,** 2125–2130 (2017).

57. Matthew Roughan. *gaussian_mixture_model.m* (ed MATLAB Central File Exchange) Retrieved May 8, 2021. `https://www.mathworks.com/matlabcentral/fileexchange/24867-gaussian_mixture_model-m`.

58. Schmied, J. J. *et al.* DNA origami–based standards for quantitative fluorescence microscopy. *Nature Protocols* **9,** 1367–1391 (2014).

59. Funke, J. J. & Dietz, H. Placing molecules with Bohr radius resolution using DNA origami. *Nature Nanotechnology* **11,** 47–52 (2016).

60. Förster, T. Zwischenmolekulare Energiewanderung und Fluoreszenz. *Annalen der Physik* **437,** 55–75 (1948).

61. Hao, X., Antonello, J., Allgeyer, E. S., Bewersdorf, J. & Booth, M. J. Aberrations in 4Pi Microscopy. *Optics Express* **25,** 14049–14058 (2017).

62. Wang, J. *et al.* Implementation of a 4Pi-SMS super-resolution microscope. *Nature Protocols* **16,** 677–727 (2021).

63. Hunsperger, R. G. *Integrated Optics* ISBN: 978-0-387-89774-5 (Springer New York, New York, NY, 2009).

64. Von Middendorff, C., Egner, A., Geisler, C., Hell, S. W. & Schönle, A. Isotropic 3D Nanoscopy based on single emitter switching. *Optics express* **16,** 20774–20788 (2008).

E Acknowledgements

I want to thank Prof. Dr. Stefan W. Hell for the opportunity to work in his group in Heidelberg. I appreciate the stronger supervision during the last year and that he gave me access to all the equipment needed for the experiments and time to learn. Further, I would like to thank Prof. Dr. Ulrich Schwarz for being part of my examination board as well as second referee for my thesis. Finally, I want to thank the other members of my examination board: Prof. Joachim Spatz and Prof. Thomas Pfeifer.

Most of all, I want to express my gratitude to my scientific supervisor, Johann Engelhardt. He shared his experience with 4Pi microscopy with me and he was a unfailing source of scientific guidance, encouragement and reassurance.

Next, I would like to thank my direct colleagues, the Physic-Boys (Tobias Engelhardt, Michael Remmel, Jan Otto Wolff and Julian Rickert). I am grateful that we could benefit from each others experience and research results. I am thankful for Julian's support and proof-reading, and for our scientific discussions about the 4Pi-MINFLUX experiment, i.e. 4PimFlux, during the last phase of my PhD. I am happy to see that he is willing to continue the experiments of my project.
A very special thank you goes out to Jessica Matthias and Richard Lincoln, who provided valuable assistance in topics covering the chemical part in my research and proof-read my thesis. Jessica M. further supported me in the sample preparation of the DNA origami nanopillars.
A very special thank you goes out to all members of the optical nanoscopy group (Physic-Boys, Chem-Guys and Neuro-Girls) and especially to Jade Cottam Jones for the support in the scientific coordination.
Thanks to the reliable stuff and staff of (a) the mechanical workshop — especially Martin Lukat for manufacturing all my designed components and for spreading an uplifting mood — (b) the electronics workshop (Matthias Steigleder) and (c) the glazier's workshop (Göttingen) for their technical support.

If I were given a doctoral hat, I would dedicate each corner to one of the following four friends: Michelle Frei, Alexander Salim, Stefan Kleyer and Marina Sabbadini! Each of you has been an immense and close support in priceless conversations and words of advice. Especially, Marina helped me to develop a broader view on science, and life in general. Further, I want to thank all supportive friends during different stages of my PhD: Ruben S., Julia J., Jan B., Jenny K., Tim D. and Manuel C..[1]

Finally, my warmest thanks go to my family and in particular my parents, Egon und Monika Held. You made it possible that I could study physics and you have been the biggest supporters ever since. Thank you for staying at my side, also during difficult phases of my PhD.

[1] I am secretly thanking J. K. Rowlings, for creating the Harry Potter world that I was thrilled to discover and into which I could retreat after tough lab days.